A decorative graphic of a scroll with a blue outline and grey circular accents at the corners. The text is centered within the scroll.

Chapter 4

*Study of Characterization of
Glassy Polymer Blends and
Composite Membranes*

Transport Properties of Polymer Blends and Composites Membranes for Selective Permeation of Hydrogen

4.1.1 Introduction

4.1.2 Membrane Preparation

4.1.3 Result and Discussion

4.1.3.1 Gas Permeability and Selectivity

4.1.3.2 Diffusion and Solubility Coefficients

4.1.3.3 Thickness and Porosity Measurement

4.1.3.4 Robeson Upper Bound

4.1.3.5 Fourier Transform Infrared (FT-IR) Spectroscopy

4.1.3.6 Energy Bandgap Analysis

4.1.3.7 FE-SEM Morphology and EDX

4.1.3.8 Differential Scanning Calorimetry (DSC)

4.1.3.9 Calculation of Activation Energy

4.1.3.10 Thermalgravimetric Analyzer (TGA)

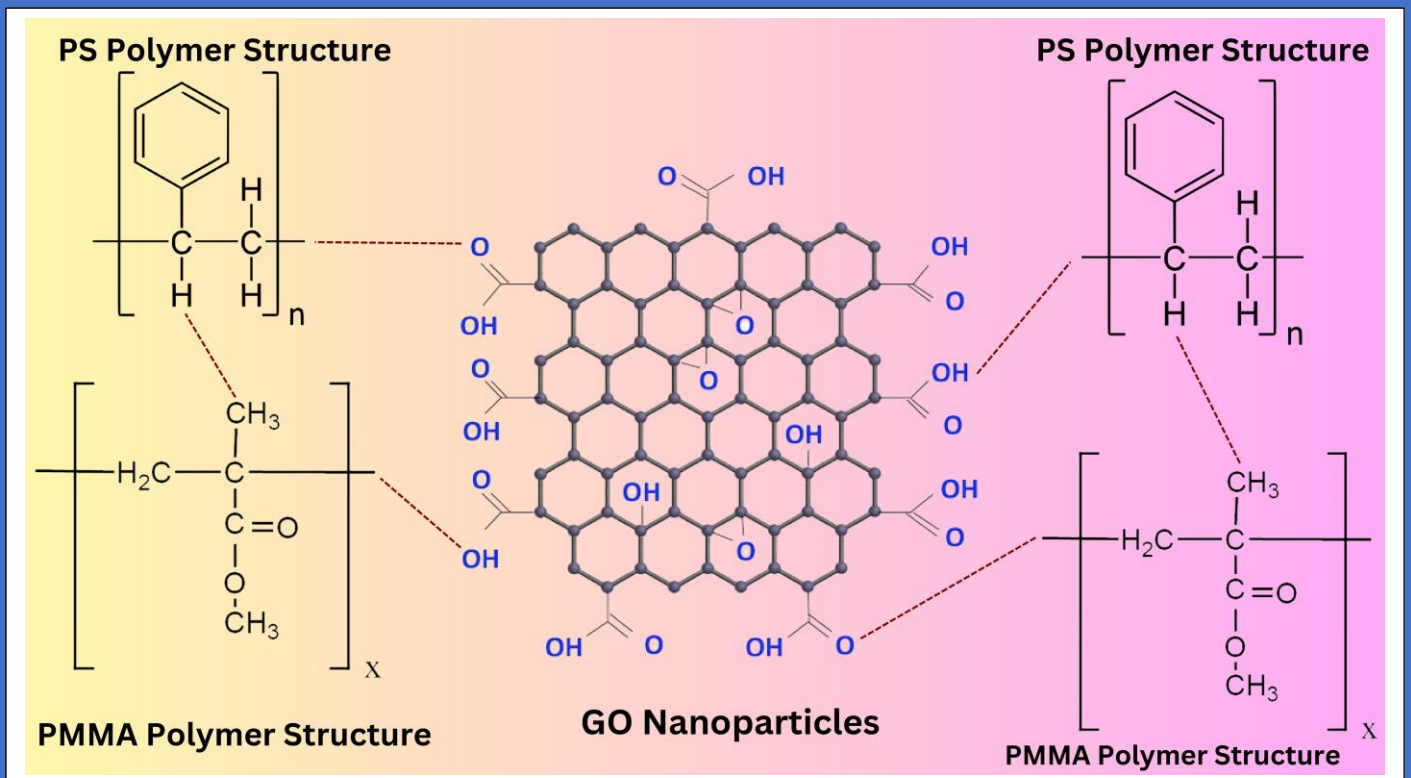
4.1.3.11 X - ray Diffraction

4.1.4 Conclusion

References

Chapter – 4.1

Transport Properties of Polymer Blends and Composites Membranes for Selective Permeation of Hydrogen



In this chapter, the discussion of about hydrogen gas permeation and its applications has been reported. Dispersion of graphene oxide (GO) in a polymer blend of Polystyrene (PS)/Poly (methyl methacrylate) (PMMA) nanocomposite membranes is present. Chapter 4.1 reports a study of blends of PMMA and PS that were prepared in different ratios of weight percentage for PMMA: PS (80:20, 50:50 and 60:40) composite with 1 wt% of GO and 2 wt% of GO. The structural and morphological properties of these prepared composite membranes have been characterized using gas permeation, SEM and EDX. UV Spectroscopy and FT-IR have carried out the optical absorbance measurement of the composite membranes. The permeability measurements indicate the GO nanofillers in blends of PS/PMMA higher permeability for hydrogen gas than that of pure polymers. The gases used for the permeation measurements were H₂, CO₂, N₂ and CH₄. Selectivity has been calculated for H₂/CO₂, H₂/N₂ and H₂/CH₄ gas pairs and plotted to show Robeson's 2008 upper bound and compared with reported data. The transport properties of these gases have been compared with that of a pure polymer membrane. There is a trade-off between permeability and selectivity parameters; GO nanofillers keep selectivity constant as permeability increases, which the nanogap theory could explain. DSC has been considered one of the most versatile thermal analysis tools to characterise polymer samples. This chapter 4.1 shows a DSC study of PMMA/GO (1%) and PS/GO (1%) and nanocomposite blends of PMMA and PS and also studies of X-ray diffraction of membranes.

4.1.1 Introduction

In the petrochemical sector, notably those for gas separations and purifications, significantly focus exclusively on modified membrane technology. Various methods, with natural gas reforming being the most common, can be used to produce hydrogen. Therefore, it is essential to separate hydrogen from other gas mixtures such as CO₂ and CH₄ using a filtration system. Steam reforming of natural gas currently stands as the most economically viable and widely used method for hydrogen production, accounting for over 80% of the global supply [1]. Poly (methyl methacrylate) (PMMA) is used in a wide range of applications, including optical, biological, denture, and prosthetic materials. Exceptional properties of polystyrene (PS) have resulted in the PS/PMMA blend, which can be used in a various industries [2]. Because of its outstanding structural, mechanical, thermal, optical, and electrical properties, graphene oxide (GO) is an ideal two-dimensional filler nanomaterial for polymer nanocomposites for applications in a wide range of technical fields of study [3].

Various efforts have been made to generate a combination of PS/PMMA composite for GO membranes because GO substrates may increase membrane thickness and penetrating flux while providing appropriate mechanical strength for composite membrane production [4]. As a substrate in the present chapter, a PS/PMMA-GO modified blend composite membrane with high packing density, low mass transfer resistance, and good thermal and chemical durability was used [4]. A nanocomposite of PS and PMMA in which GO nanoparticles play an important role in improving H₂ molecule transport routes. As the GO quantity grows, so does the excess free space, which enhances permeability. These results indicate that composite membranes synthesized of PS/GO and PMMA/GO may efficient hydrogen filters. Lighter gases, such as H₂, CO₂, and O₂, have a greater influence on nanocomposite membrane penetration than heavy gases, such as N₂ and CH₄. For all observed gas pairs, the nanocomposite membrane separation factor approaches Robeson's upper limit bound 2008. The H₂/O₂ gas pair is exactly above the upper limit boundary line, which is emerges for a new type of membrane materials for gas separation [6].

4.1.2 Membrane Preparation

In present study, PS and PMMA polymers were dissolved in a suitable Dichloromethane solution. The polymer matrix phase was simply dissolvable, while graphene oxide nanoparticles were disseminated in the same solution. The solution casting process was used to synthesize a mixture of PS/PMMA polymeric membrane with graphene oxide nanofillers. These PS and PMMA were mixed using a magnetic stirrer for their blend and blend composite with GO nanofillers. To obtain a homogeneous solution, the PMMA, PS, and GO nanofiller solutions were independently agitated for 3 hr in a Dichloromethane solvent, and then the mixtures of PMMA/GO (1 wt%), PS/GO (1 wt%), and PS/PMMA composite with GO (1 wt%) with varying wt% of PMMA: PS (80:20, 60:40, 50:50, 60:40, and 20:80 w/w%) was sonicated for 1 hr with a probe-sonicator to avoid agglomeration, and then the whole solution was agitated for 24 hr at room temperature. The combination was moved to a flat-bottomed glass, and the solvent was allowed to evaporate overnight in the system. The permeability of these membranes was determined the following day after they were removed from the petri dish, and the thickness of the various membranes was measured by using a digital thickness meter and various characterization techniques of membranes have been discussed in chapter 2 [7].

4.1.3 Results and Discussions

4.1.3.1 Gas Permeability and Selectivity

Since hydrogen is far more permeable to polymers than other gases, such as nitrogen, methane, and carbon dioxide, membranes were initially used to separate the hydrogen from mixtures of other gases. Due to its speedy capacity, membrane-based gas separations were first focused on separating H₂ from CO₂. The filtering process used in gas refinement is another industrial use for hydrogen-based membranes. Such selectivity's may be readily attained using a number of glassy polymers, and membrane systems have been tested using polymers with selectivity surpassing H₂/CH₄. However, the greater selectivity has been typically characterized by decreased flow rates. The statement from equation (2.1) about the constant pressure /variable volume system controls how quickly gas flow and permeability change. The size and composite of membranes affect the passage of gas molecules through them. The gas molecules passed through pure PS, PMMA, blends of PS/PMMA and blend composite of PS/PMMA-GO membranes in a size-dependent order, gases with lower kinetic diameters penetrate faster. In comparison to pure PS and PMMA, gas flow through composites with nanofillers behaves differently from that through polymer materials, with a significant reduction in the permeability of gases with greater kinetic diameters. The movement of hydrogen gas molecules over the membrane produces an appropriate pressure gradient. Diffusion takes both membrane and gas flow properties into consideration when calculating gas penetration rates [8]. It has been observed that mixed matrix membranes (MMMs) utilize the solution diffusion model. In the movement of gas molecules through MMMs, the particle size, particle agglomeration and interfacial morphologies all play, their contribution in final permeability value.

This is especially true for a blend of polymer and inorganic filler that flow rate of hydrogen gas through different blends and nanocomposite materials is shown in Figure 4.1.1 [9]. Since H₂ has a smaller molecule than the other gases, even at high pressures, it may easily pass through thick structures. A greater penetration rate and more effective transport channels are now possible because of modifications made to the membrane material. Figure 4.1.1 (I and II), the permeability and selectivity values are shown for both a pure blend of PS/PMMA and a composite membrane containing graphene oxide nanofillers. These membranes were analyzed for their performance with various gases such as H₂, O₂, CO₂, N₂, CH₄, and Ar. It has been observed that the transport of hydrogen in GO nanocomposite membranes is a complex process.

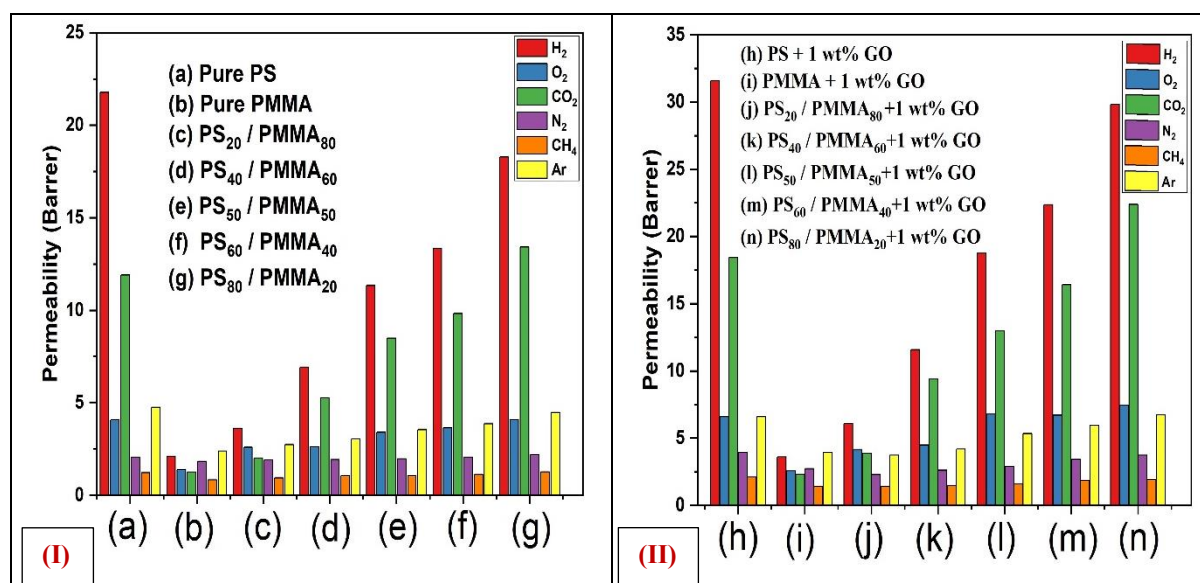


Figure 4.1.1: Permeability of membranes (I) Pure and blend of PS/PMMA polymer membranes (II) blend composite of PS/PMMA-GO membrane

It is observed that membrane blending of two polymers increases hydrogen penetration, PMMA and PS mix membranes have better hydrogen gas permeability. The hydrogen permeation in these nanocomposite membranes follows a solution-diffusion mechanism, although with additional steps, affected by the partial pressure gradient across the membrane. As a result, the diatomic hydrogen molecule breaks down into atomic hydrogen. It is important to note that the permeability sequence may differ from the dispersed gas flow rate, as factors such as membrane thickness and exposed surface area are taken into consideration [10]. Hydrogen atoms are recombined into molecular form during desorption from the bulk composite volume due to the solution-diffusion process [11]. The polymer composite of graphene oxide may potentially affect the rate of hydrogen permeation if these additional processes are considered. One notable observation was that the permeability of hydrogen gas significantly surpasses that of other gases [12]. This might be because of the exposed surface thermal properties were altered during the synthesized process, causing condensation and altering the solubility factor. The solubility of the penetrant is also a factor in determining permeability. The solubility of gas molecules and polymer segments was enhanced by condensing gas molecules and the mixing polymer segments. Many types of research have shown that the quantity of nanofiller in the polymer matrix may improve gas permeability, contrary to the Maxwell model, which states that increasing the filler volume fraction lowers gas penetration by composite membranes [13]. This contradict effect may be due to graphene oxide nanofillers not adhering tightly to the PS and PMMA blend, creating nanogaps around

the filler surface [14]. Because it is a much bigger molecule than H_2 , carbon dioxide diffuses through the membrane much more faster.

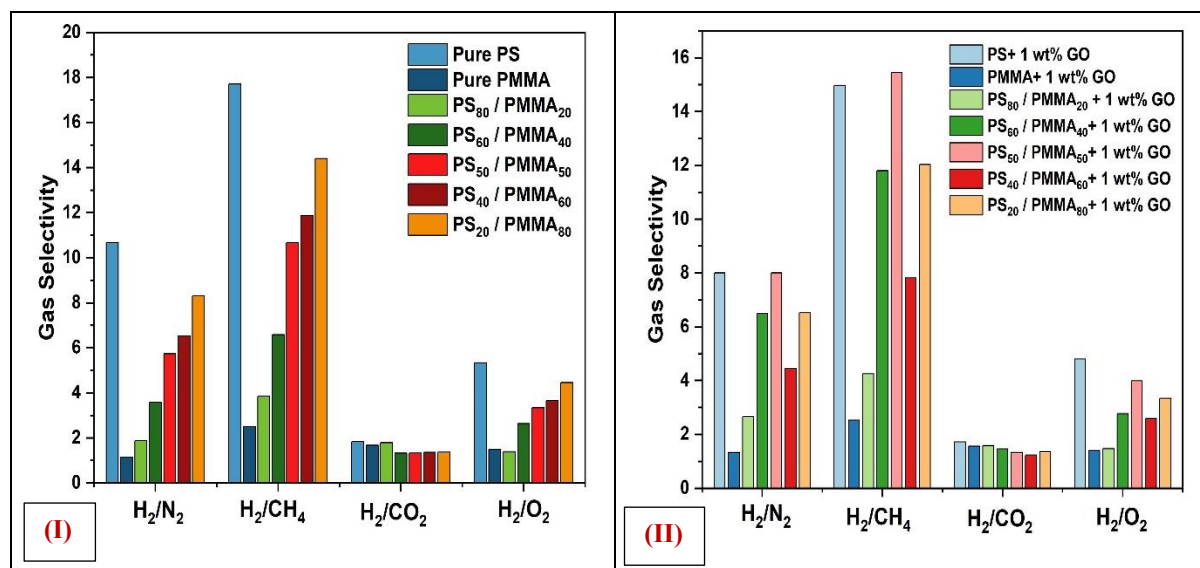


Figure 4.1.2: Selectivity comparison of (I) Pure and blend of PS/PMMA polymer membranes (II) Blend of PS/PMMA composite with graphene oxide nanofillers

The selectivity of PS/PMMA blend composites with GO nanofillers in mixed matrix membranes (MMMs) is shown in Figure 4.1.2 (I and II), where the addition of nanoparticles enhances the permeability of pores in the PS/PMMA blend. Combining two different polymers or a polymer-inorganic filler mixture in hybrid membranes can lead to increased gas permeability and separation [15]. Carbon dioxide (CO_2), being a larger molecule compared to hydrogen (H_2), exhibits faster diffusion through the membrane. Among the various composites, $PS_{20}/PMMA_{80}$ stands out with the highest permeability for both H_2 and CO_2 gases. Additionally, $PS_{40}/PMMA_{60}$ and $PS_{50}/PMMA_{50}$ blends, show higher permeability compared to other membrane blends [16]. The polar nature of H_2 molecules leads to interactions with the polar PS groups, affecting the packing density of the membrane and potentially influencing gas diffusion rates. Faster diffusion occurs when there is a shorter time lag. Moreover, to calculate the permeability coefficient, the thickness of the membrane was considered, which is the most important parameter for determining the permeability of oxygen, because gas permeation is a thickness-dependent characteristic membrane thickness is a crucial consideration when calculating gas permeability [17]. Figure 4.1.3 (I) is a plot showing the suggested permeabilities of pure PS, pure PMMA, PS/GO (1 wt%), PMMA/GO (1 wt%), PS/GO (2 wt%), and PMMA/GO (2 wt%) with respect to different gases. From those results, it was observed that as we increased the wt% of graphene oxide nanofillers from 1 wt% to 2 wt%, the

permeability of materials changes drastically when increased because GO nanofillers increase the fractional free volume (FFV) and porosity of material [18].

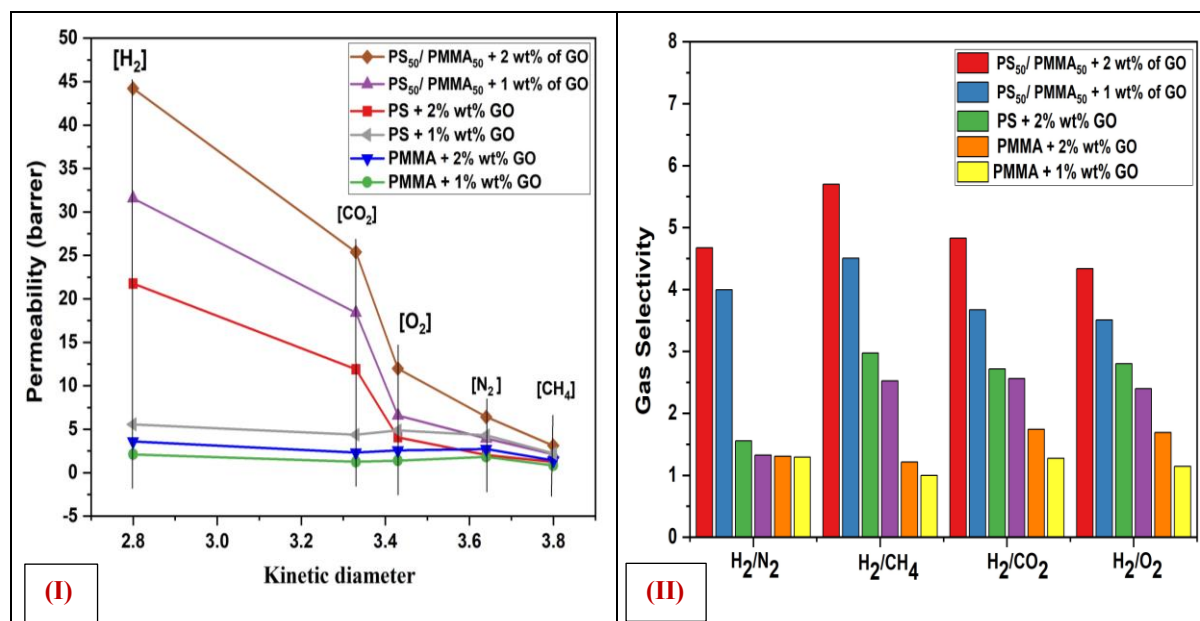


Figure 4.1.3: (I) Permeability and (II) Selectivity, comparison of pure and blend PS/PMMA composite with GO membranes

As observed from Figure 4.1.2 (I and II) and Figure 4.1.3 (II), it is clear that the selectivity of H₂/CH₄ is especially higher than any other gas pair, primarily due to the lower permeability of methane gas. The addition of filler particles has a significant impact on material permeability. For instance, when a composite of 2 wt% of GO is added to a PS membrane, the permeability increases nearly twofold compared to pure PS permeability. Additionally, it has been observed that the permeability of PMMA/GO surpasses that of pure PMMA, as well as PS. Furthermore, the permeability of PS increases when blend with PMMA, especially when the PMMA content has been increased to 80 wt% [19]. This behaviour differs from the decrease in H₂ and CO₂ permeability that occurs when increasing PMMA content with PS, indicating a slightly different behaviour. The impact of filler content in the blend matrix behaves similarly to its impact on H₂ and CO₂ penetration, although it exhibits lower O₂ permeation rates. This variation may be attributed to the size and structure differences between oxygen molecules and H₂. When comparing the results of PS/GO membranes with PS/GO (1 wt%) filler content to those with PS/GO (2 wt%) filler content, the permeability of H₂ nearly doubles. The incorporating of GO nanoparticles in the PS/PMMA nanocomposite blend enhances the permeation of hydrogen gas. When high pressure is applied, this blend polymer composites with graphene oxide can lead to improved H₂/CO₂ selectivity [20]. Notably, an increase in the

weight percentage of GO nanofillers is associated with a simultaneous decrease in selectivity, as observed in Figure 4.1.3 (II). The incorporation of GO nanofillers into a polymer matrix significantly enhances the membrane performance in terms of hydrogen permeation. In summary, the addition of GO nanofillers to pure polymers substantially increases permeability, particularly in case of hydrogen gas [21].

4.1.3.2 Diffusion and Solubility Coefficients

The membrane separation process can be simplified by considering two fundamental parameters: diffusivity (D) and solubility (S). Solubility defines how many gas molecules can be dissolved within a membrane material, while diffusivity measures how easily these molecules can move through the pores of the membrane. The ability of a membrane to allow molecules to pass through is referred to as its permeability. According to the Maxwell model, as the volume fraction of fillers in composite membranes increases, gas permeation tends to decrease. However, several studies have looked into the potential for increasing gas permeability by adding more graphene oxide nanofillers into the PS/PMMA blend polymer blends. The aggregation of particles plays a critical role when combining organic and inorganic compounds, depending on the specific composite with nanofillers [22]. While the choice of inorganic filler material significantly influences gas diffusion, the performance of hybridized membranes has been also greatly affected by the selection of polymer blends. In general, the diffusivity and solubility of the penetrant gas passing through the membrane phase determine the magnitude of gas permeation through the membrane. Many times, factors including an increase in solubility or an increase in free volume may be responsible for improved gas permeability in nanocomposite membranes. Figure 4.1.4 (I and II) provides data on diffusion coefficients and solubility coefficients.

In the current study, it is important to note that hydrogen gas (H_2) has not been considered a polar gas, and higher solubility is not the main cause of its more quick penetration in the MMMs. This data indicates that in the case of nanocomposite membranes, the interaction between the filler material and the polymer blend, particularly when functional groups on the filler surface interact with polar gas molecules, leads to an increase in solubility [23]. It has been determined that it instead related to the increase in free volume created by the dispersion of nanofillers. The interaction between nanofillers and polymer chain segments plays a crucial role in expanding this free volume.

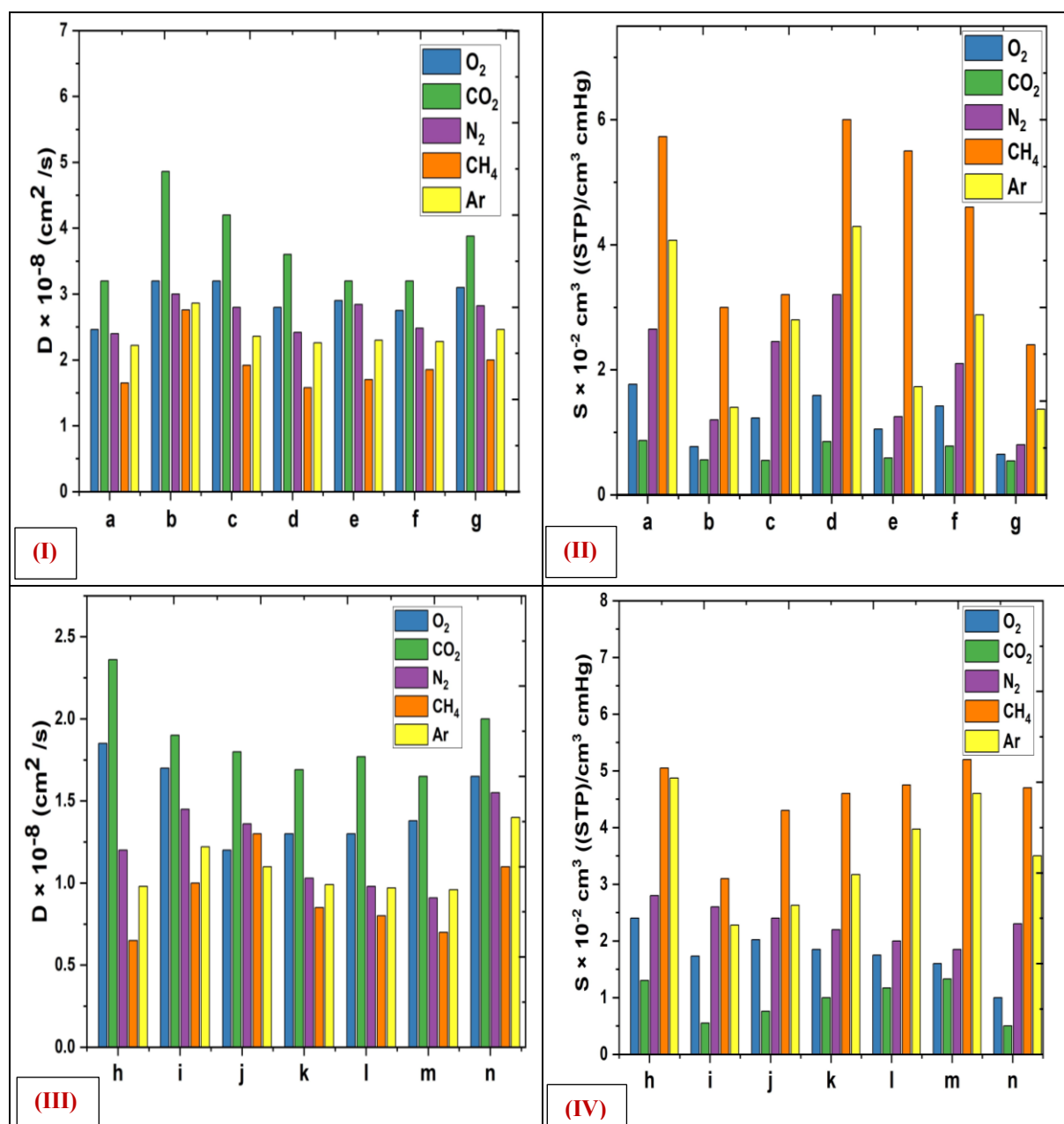


Figure 4.1.4: Diffusion and the Solubility coefficients value of **(I and II)** pure and blend of PS PMMA polymer membranes **(III and IV)** blend composite of PS/PMMA with graphene oxide, here (a) Pure PS, (b) Pure PMMA, (c) PS₂₀ / PMMA₈₀, (d) PS₄₀ / PMMA₆₀, (e) PS₅₀ / PMMA₅₀, (f) PS₆₀ / PMMA₄₀, (g) PS₈₀ / PMMA₂₀, (h) PS + 1 wt% GO, (i) PMMA + 1 wt% GO, (j) PS₂₀ / PMMA₈₀ + 1 wt% GO, (k) PS₄₀ / PMMA₆₀ + 1 wt% GO, (l) PS₅₀ / PMMA₅₀+ 1 wt% GO, (m) PS₆₀ / PMMA₄₀+ 1 wt% GO, (n) PS₈₀ / PMMA₂₀+ 1 wt% GO

When graphene oxide nanoparticles are incorporated into PS/PMMA blends, they interfere with the packing of polymer chains and enhance the void space between these chains. The permeation of the gas penetrant has been eventually improved by the increased void space, in this case of H₂. As more nanofiller has been added, the fractional free volume increases, further improving H₂ permeability. The addition of GO to PS/PMMA composites particularly

enhances the flow of hydrogen gas molecules. These changes in hydrogen transmission can be attributed to improvements in the permeability coefficient. The composite structure of the PS/PMMA blend with GO fillers is significant in creating additional free volume to facilitate hydrogen diffusion. The concentration of fillers also contributes to the abundance of available free space, which supports efficient gas permeation.

4.1.3.3 Thickness and Porosity Measurement

The thickness of a membrane is a crucial parameter that significantly influences its performance in various membrane separation processes because it acts as a barrier controlling the transfer of chemicals through the membrane surface [24]. In applications like ultrafiltration, where maximizing permeation flux is important, it is essential for the membrane to be as thin as possible while still maintaining its mechanical stability. Another critical factor affecting membrane performance is its porosity. Figure 4.1.5 (I and II) shows the thickness and porosity of membranes in two scenarios: the PS/PMMA blend and the PS/PMMA-GO blend composite membranes.

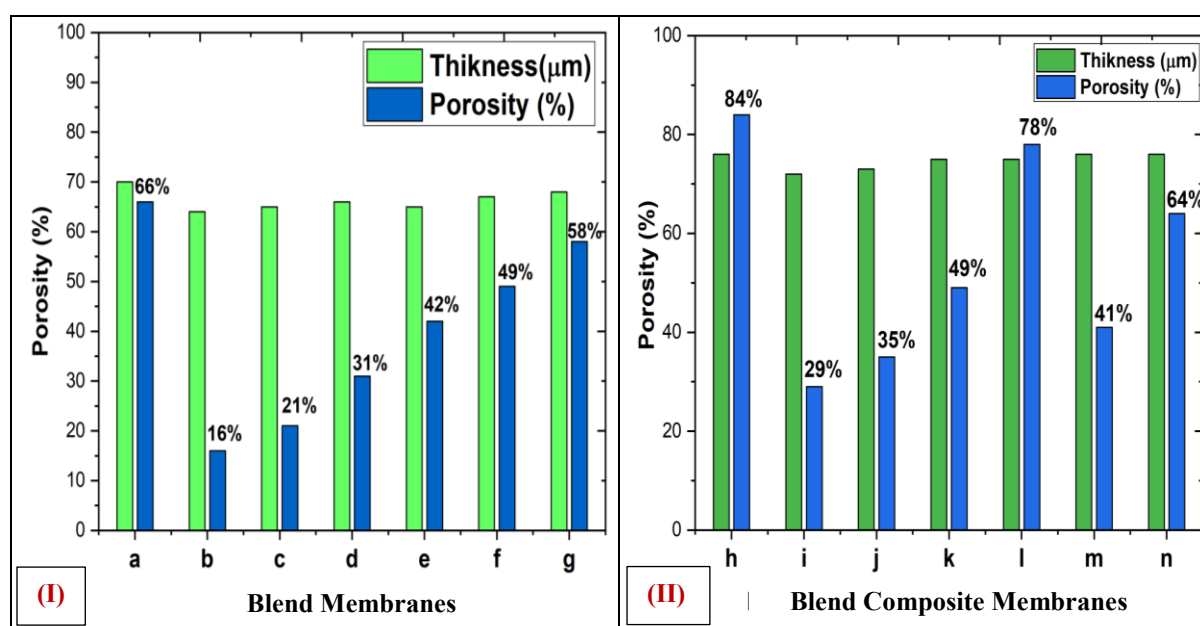


Figure 4.1.5: Thickness and Porosity comparison of (I) pure and blend of PS/PMMA polymer membranes (II) blend composites of PS/PMMA-GO membranes, here (a) Pure PS, (b) Pure PMMA, (c) PS₂₀ / PMMA₈₀, (d) PS₄₀ / PMMA₆₀, (e) PS₅₀ / PMMA₅₀, (f) PS₆₀ / PMMA₄₀, (g) PS₈₀ / PMMA₂₀, (h) PS + 1 wt% GO, (i) PMMA + 1 wt% GO, (j) PS₂₀ / PMMA₈₀ + 1 wt% GO, (k) PS₄₀ / PMMA₆₀ + 1 wt% GO, (l) PS₅₀ / PMMA₅₀ + 1 wt% GO, (m) PS₆₀ / PMMA₄₀ + 1 wt% GO, (n) PS₈₀ / PMMA₂₀ + 1 wt% GO

In the case of both blend and composite polymer membranes, it is significant that pure PS has higher porosity compared to pure PMMA. Moreover, the porosity increases as the

weight percentage of GO in the PS/PMMA polymer blend composite is increased, as shown in Figure 4.1.5 (I) [25]. The porosity of the membranes shows an observable increase, going from 66% for pure PS to 84% for the PS polymer composite with 1 wt% of GO. Similarly, for pure PMMA, the initial porosity was 16%, and after the addition of 1 wt% of GO, it increased to 29% [26]. All blend composite membranes show this tendency of increasing porosity, all blend composite membranes show this tendency of increasing porosity, as observed in Figure 4.1.5 (II) [27]. In both Figure 4.1.5 (I and II), the thickness of the membranes remained relatively stable regardless of changes in the blending ratio or the addition of GO nanofillers. This suggests that membrane thickness does not play a significant role in determining membrane permeability [28]. These results align with prior research indicating that the addition of more nanofillers to a material tends to enhance porosity and void sizes.

4.1.3.4 Robeson Upper Bound

In the context of polymeric membranes, there exists a trade-off relationship that is associated with an upper-bound correlation. This relationship can be visualized by plotting the logarithm of the separation factor against the logarithm of the gas with higher permeability. Such a plot provides a limit to achieving the desired outcome of both a higher separation factor and high permeability [29]. This upper limit relationship has been demonstrated to hold true for various gas pairs, including H_2/CO_2 , H_2/N_2 , O_2/N_2 , H_2/CH_4 , H_2/O_2 , and CO_2/CH_4 , as observed from Figures 4.1.6, Figures 4.1.7 and Figures 4.1.8.

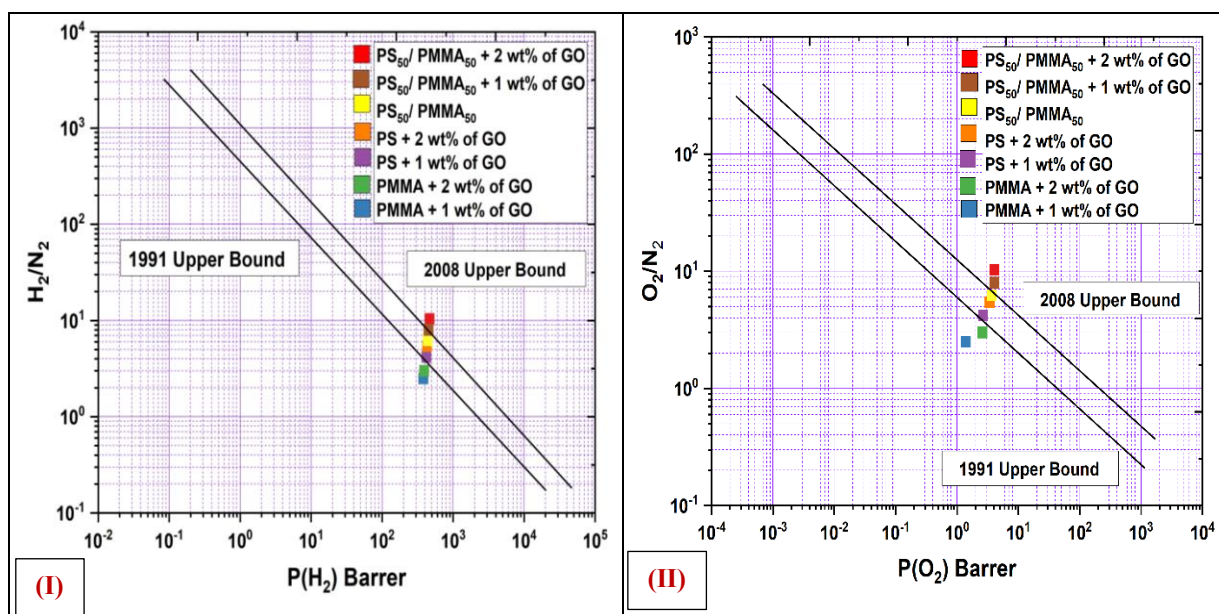


Figure 4.1.6: Robeson upper bound correlation for (I) H_2/N_2 separation and (II) O_2/N_2 separation

Figure 4.1.6 (I and II), shows the upper limit relationships for H_2/N_2 and O_2/N_2 , it is important that there has been minimal movement in the upper limit relationship since 1991, while the significant the number of data obtained [32]. On one end of the range with low permeability, you can observe variations of polyimide, while on the high permeability end of the upper limit, there are data points related to nanocomposite materials. Freeman, through theoretical projections, established this empirical upper limit connection, and the actual experimental evidence closely aligns with these predictions [30]. The data published on membrane separation since 1991, which goes beyond the data used in the original correlation and the upper limit concept itself, allows for a more comprehensive evaluation of the relationships between structural properties and membrane separation performance. Experimental studies and methodologies involving group contributions have contributed significantly to our understanding of membrane separation and membrane structure. As a result, researchers have found that meet or exceed the initial upper limit. As obtained in the original paper [31], it was remarked that the upper limit relationship should move somewhat higher when more structure/property optimization of polymers based on solution-diffusion transport happens [30,31]. This suggests that as researchers continue to optimize polymer structures based on solution-diffusion transport, the upper limit concept may need to be adjusted upwards to allow these advancements in membrane science.

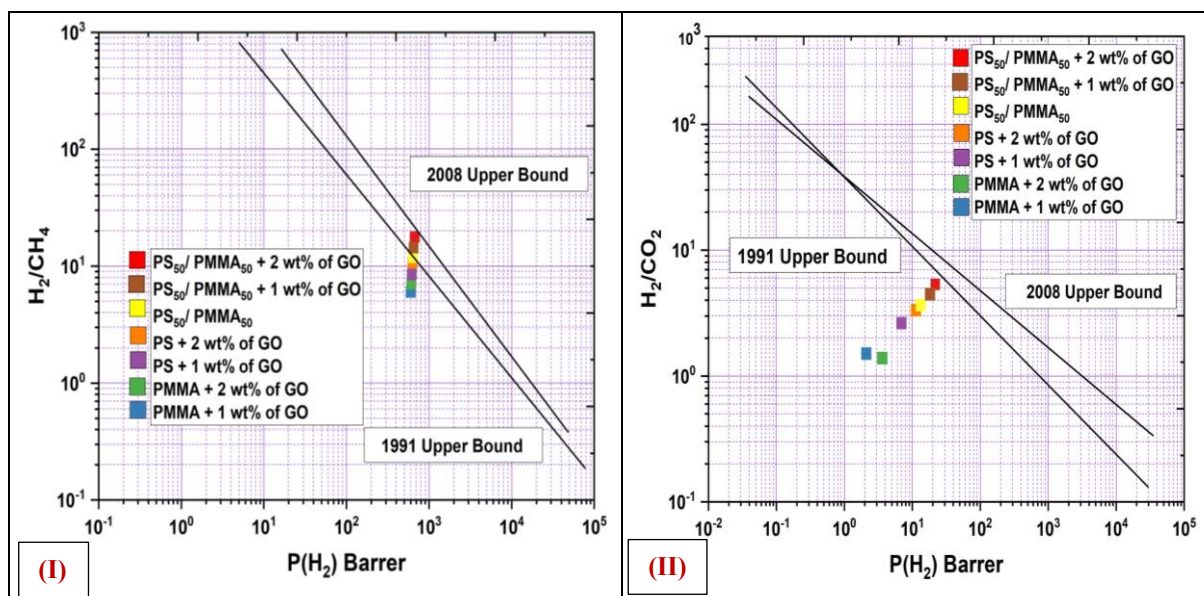


Figure 4.1.7: Robeson upper bound correlation for (I) H_2/CH_4 separation (II) for H_2/CO_2 separation

Figure 4.1.7 (I and II) highlights the upper-bound relationships for H_2/CH_4 and H_2/CO_2 . Interestingly, there are numerous data points located just above the initial upper limit, particularly for H_2/CO_2 . Polyimide variations exhibit a wide range of upper limit positions,

which includes from the low permeability end to the high permeability end. This emphasizes an earlier established upper limit connection between H_2 and CO_2 . To maintain the selectivity between H_2 and CO_2 , a hybridization process may be used for gas mixture separation and hydrogen recovery. Additionally, a few data points related to polystyrene at the higher permeability end of the relationship have caused a slight change in the slope of the upper bound relationship. This shift in slope might be attributed to the fact that there were fewer data points in the lower permeability portion of the dataset in comparison to the original correlation [33].

The slope of the line was expected to remain relatively consistent, and this expectation has proven accurate. There are various methods for surpassing the upper limit, including the use of heterogeneous membranes built upon homogeneous polymer sheets. However, achieving molecular sifting structures in polymeric membranes is currently not achievable. The upper bound correlation represents an empirical connection that reflects the current state of the field. It is important to note that the polymeric materials used to establish the upper bound correlation do not include heterogeneous membranes, surface-modified membranes, or molecular filtration membranes [32,33].

However, it is worth highlighting that certain polymers with unique structural properties, such as those with a 'ladder' structure are of interest since they approach filtration-type structures and are positioned around or at the existing empirical upper limit. This suggests that there may be limits to polymeric gas membrane separation based on structural properties. Efforts are ongoing to identify polymeric structures that can exceed the empirical upper bound limitations. While some gas pairings have shown only minor increases, there have been significant changes observed in specific gas pairs, as indicated in the following data analysis. The results are obtained from a single study with identical experimental membrane preparation conditions [34]. The statistics regarding permeability-separation factors for polyaniline variations have shown a general consistency across the literature, which is why they were included in the analysis. However, they were excluded in cases where individual data points fell within the range of the existing upper limit correlation. It is important to note that using these methods can lead to the creation of polymeric compounds that are insoluble and infusible, far exceeding the upper limit correlation. Although the 'upper limit' line was originally established experimentally, there is now sufficient data available to establish a more realistic boundary for permeability over a wide range of values spanning many decades [35]. It is observable that membranes composed of polymer blends composites with graphene oxide, especially those with an increasing weight percentage of GO nanofillers, tend to exhibit the

highest selectivity and are positioned closest to the upper limit lines. As shown in Figure 4.1.8 (I), in the case of the H_2/O_2 upper limit relationship, three materials, $PS_{50}/PMMA_{50}$ with 2 wt% of GO, $PS_{50}/PMMA_{50}$ with 1 wt% of GO, $PS_{50}/PMMA_{50}$, and PS with 2 wt% of GO are all located within the upper bound range between from 2008 to 1991 [35].

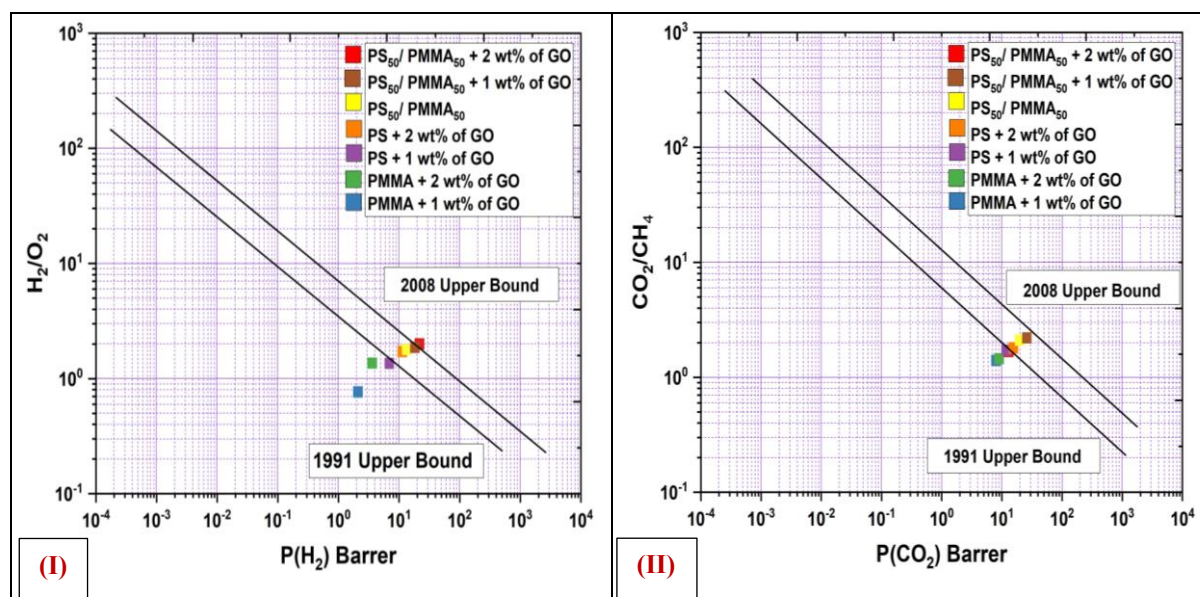


Figure 4.1.8: Robeson upper bound correlation for (I) H_2/O_2 separation and (II) CO_2/CH_4 separation

This data indicates minimal shifts in the upper limit positions, and it is important to observe that membrane performance is strongly influenced by the choice of polymer used in its fabrication. Parameters like flow, permeability, and selectivity all play vital roles in determining membrane transport performance. The data related to polymeric membrane structure and properties have significantly expanded since the commercialization of membrane gas separation system. The relationship between selectivity and permeability has often been characterized as a trade-off, with most data points falling below a well-defined line, as shows in Figure 4.1.8 (II) for the CO_2/CH_4 upper limit relationship. This relationship has been validated for various gas pairings, including H_2 , O_2 , N_2 , CO_2 , and CH_4 , suggesting its broad applicability. Determining an upper bound for analysis requires using data from studies where comparable membranes were used to analyzed both permeability and selectivity [36].

It is possible to achieve values above the upper limit with nanocomposite membranes containing graphene oxide nanofillers [37]. In most membrane gas separation processes, one of the product streams is permeate. However, in the case of air separation, both streams are typically considered products and can be further processed to obtain the desired purity following the initial separation achieved by the membranes [36,37].

4.1.3.5 Fourier Transform Infrared (FT-IR) Spectroscopy

The analysis of these polymer nanocomposites involved the use of fourier transform infrared (FT-IR) analysis, and the results are shows in Figure 4.1.9. The FT-IR spectrum shows characteristic bands associated with the various chemical groups present in the materials. Specifically, bands at 3448 cm^{-1} and 2925 cm^{-1} are attributed to the stretching vibrations of CH_2 and CH_3 groups in PMMA, while the presence of an ester carbonyl group ($\text{C}=\text{O}$) in PMMA is indicated by the stretching vibration at 1732 cm^{-1} . The bands at 690 cm^{-1} are likely linked to the stretching vibration of the $\text{C}-\text{O}$ bond (ester bond) [38].

Additionally, the bands at 1455 cm^{-1} and 1560 cm^{-1} correspond to the bending vibrations of $\text{C}-\text{H}$ bonds. A peak at 1385 cm^{-1} is associated with the twisting mode of bending vibrations of the $\text{C}=\text{C}$ group in PMMA, and peaks at 980 cm^{-1} , 1120 cm^{-1} , and 1210 cm^{-1} correspond to the stretching vibrations of $\text{C}-\text{O}-\text{C}$ bonds [37]. In the case of composite with graphene oxide, its FT-IR spectrum reveals characteristic vibrations related to $\text{C}-\text{O}$, $\text{C}-\text{O}-\text{C}$, and $\text{C}-\text{OH}$ bonds at 280 cm^{-1} , 1120 cm^{-1} , and 1200 cm^{-1} , respectively. The peak at 1510 cm^{-1} is assigned to the skeletal vibrations ($\text{C}=\text{C}$) within graphene domains. Surface of GO features multiple $-\text{OH}$ functionalities, as visible from the peaks at 3600 cm^{-1} and 480 cm^{-1} . A reduction in the 3600 cm^{-1} , GO contains FT-IR peak associated with $-\text{OH}$ functionality and a decrease in the FT-IR peak related to $\text{C}-\text{O}-\text{C}$. Furthermore, a smaller FT-IR peak at 1732 cm^{-1} , corresponding to the $\text{C}=\text{O}$ group of GO, can also be observed in the composite, confirming the presence of GO fillers [37,38].

Even after reduction, a $\text{C}=\text{O}$ peak is still present in the PMMA/GO and PS/GO nanocomposites, primarily due to the contribution of $\text{C}=\text{O}$ groups originating from the PMMA component. However, the intensity of the $\text{C}=\text{O}$ group FT-IR peak is lower in comparison to pure PMMA. In the FT-IR spectrum of PMMA/GO nanocomposites, there are no additional distinguishable peaks, and it closely resembles the pattern of nanocomposites. Notably, the $\text{C}=\text{O}$ band occurs at a lower frequency, typically between 1732 cm^{-1} and 1748 cm^{-1} , due to the presence of intramolecular hydrogen bonds within GO, which were previously reduced [38]. Carbonyl oxygen may also form intermolecular links with oxygenated molecules in carbon scaffolds, resulting in a shift in frequency. This shift does not overlap with the $\text{C}=\text{C}$ band and allows the carboxyl groups from GO to be observed. Infrared spectroscopy may not effectively distinguish between two completely incompatible polymers. When two polymers are incompatible, their infrared spectra are likely to exhibit significant differences [38,39].

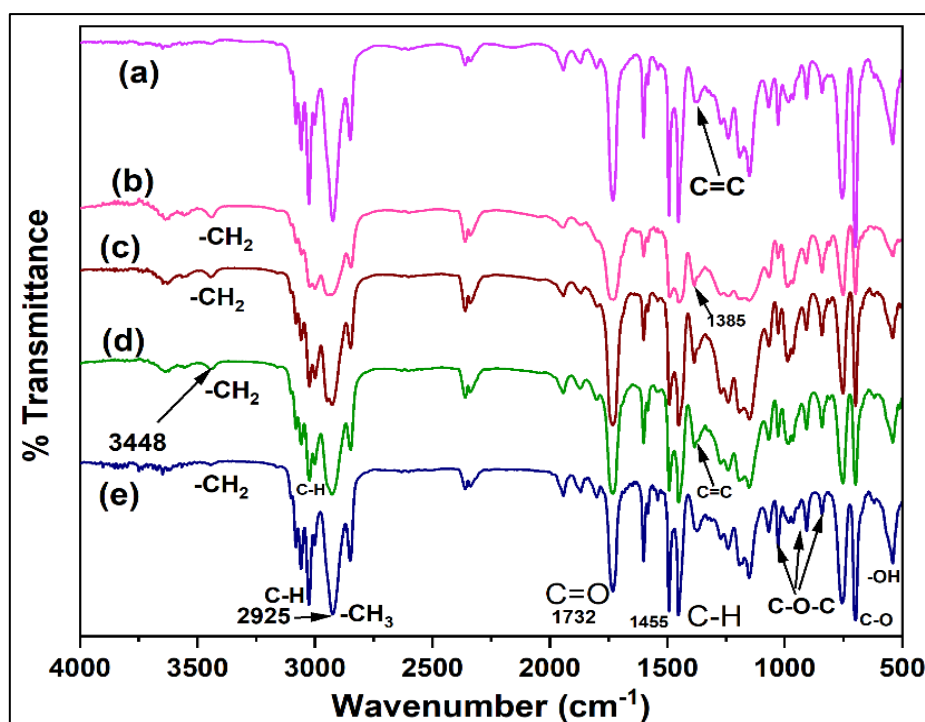


Figure 4.1.9: FT-IR Spectra of blend PS/PMMA composite with graphene oxide. Here, peak represented (a) PS with (2 wt% of GO), (b) PMMA with (2 wt% of GO), (c) PS₅₀/ PMMA₅₀ with (1 wt% of GO), (d) PS with (1 wt% of GO), (e) PMMA with (1 wt% of GO)

Chemical interactions between polymers would lead to spectral changes, including band shifts and broadening. These variations in infrared spectra should be noticeable if the polymers are compatible, as they would be observable in the spectrum of blends and the individual components spectra [40].

The shifting and broadening of bands may result from such chemical interactions, and the degree of interaction can depend on how uniformly the filler has been distributed within the mixture. Nanofillers tend to clump together in solvents due to strong van der Waals forces and electrostatic interactions [41].

These interactions, while not very significant on a larger scale, become substantial at the nanoscale because of the high surface area-to-weight ratios of materials. Graphene forms connections with polymers through Van der Waals forces, π - π stacking, and hydrophobic interactions [40,41]. When graphene oxide contains oxygen groups, it weakens the van der Waals forces, allowing gas molecules to enter the spaces between the layers of the membrane [42].

4.1.3.6 Energy Bandgap Analysis

Figure 4.1.10, it is shown the energy bandgap for various membrane materials, and it includes data for blends and blend composite samples, instrumental details of UV-spectroscopy has been described in chapter 2.

Based on the data from the Tauc's plot, it is observed that variations in the bandgap (BG) values: for pure PMMA it is 4.63 eV, pure PS it is 4.13 eV, for PMMA with 1 wt% of GO it is 4.11 eV and for PS with 1 wt% of GO it is 3.59 eV. The energy band gap refers to the energy difference between the valence band, where electrons are bound to atoms, and the conduction band. In the case of polystyrene, which is an insulating polymer, there is a significant energy gap between the valence and conduction bands. The exact value of the energy band gap for polystyrene can vary depending on factors such as the molecular weight of the polymer, its crystallinity, and the presence of any additives.

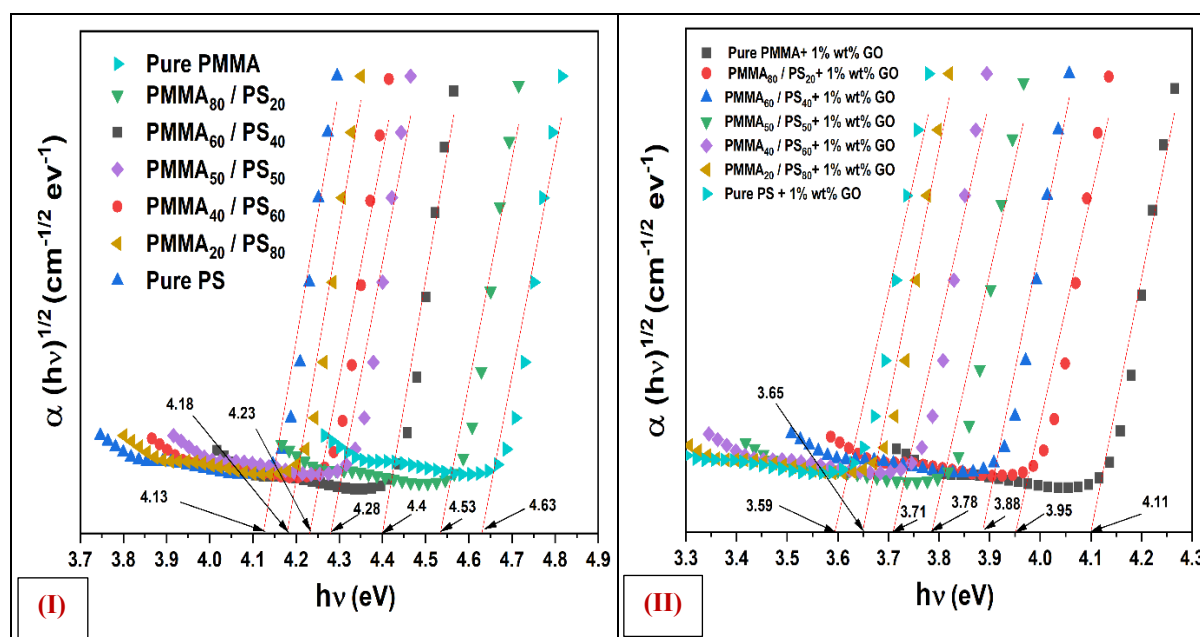


Figure 4.1.10: Absorption coefficient versus to photon energy for (I) pure and blend of PS/PMMA polymer membranes (II) blend of PS/PMMA composite with graphene oxide membranes

In general, polymers like PS and PMMA are considered to be insulators with relatively large band gaps compared to semiconductors or conductors, but as we composite with GO nanofillers the band gap decreased it shows materials behave towards semiconductors or conductor types [42].

Table 4.1.1: Represent the energy bandgap of various PS/PMMA blends composite with graphene oxide nanofiller membranes

Sample Name	Energy Bandgap (eV)	Sample Name	Energy Bandgap (eV)
Pure PMMA	4.63	PMMA+ 1 wt% GO	4.11
PMMA ₈₀ /PS ₂₀	4.53	PMMA ₈₀ /PS ₂₀ + 1 wt% GO	3.95
PMMA ₆₀ /PS ₄₀	4.40	PMMA ₆₀ /PS ₄₀ + 1 wt% GO	3.88
PMMA ₅₀ /PS ₅₀	4.28	PMMA ₅₀ /PS ₅₀ + 1 wt% GO	3.78
PMMA ₄₀ /PS ₆₀	4.23	PMMA ₄₀ /PS ₆₀ + 1 wt% GO	3.71
PMMA ₂₀ /PS ₈₀	4.18	PMMA ₂₀ /PS ₈₀ + 1 wt% GO	3.65
Pure PS	4.13	Pure PS+ 1 wt% GO	3.59

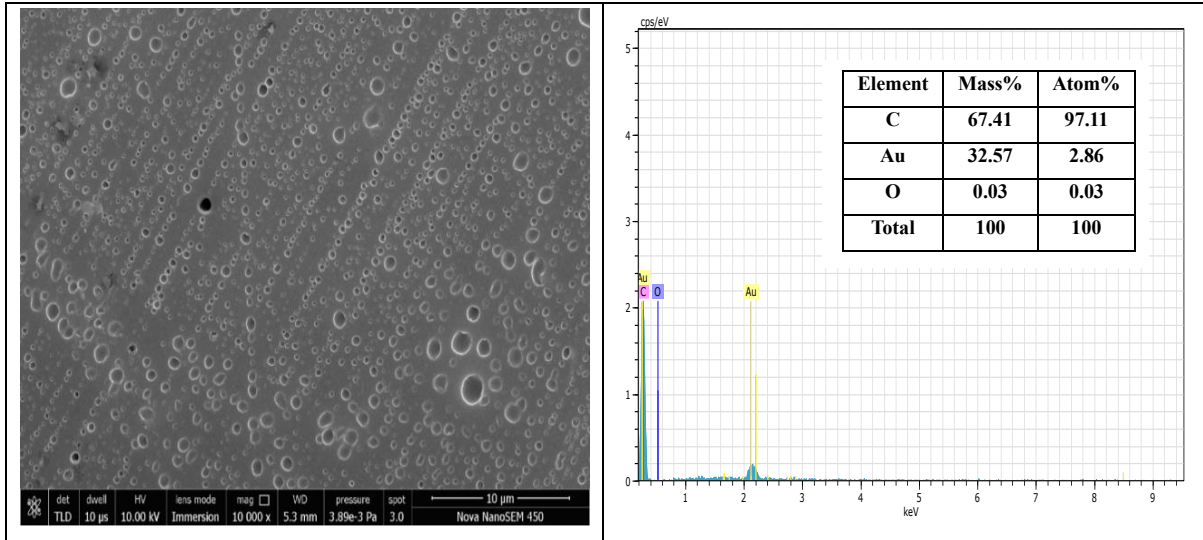
Table 4.1.1 provides the energy bandgap values for various nanocomposite polymer membranes. Energy bandgap measurements for both amorphous and crystalline materials can be obtained through optical transmission spectra [40]. The energy bandgap was determined using Tauc's plot, as shown in Figure 4.1.10.

This data indicates two primary trends: (i) Adding graphene oxide nanofillers to pure polymers or polymer blends leads to a reduction in the membrane bandgap. This decrease in bandgap is likely due to the conductive nature of GO nanofillers [40]. (ii) Increasing the weight percentage (wt%) of PMMA in PS/PMMA blends the bandgap of the membranes, significantly dropping from 4.63 eV to 4.13 eV and in this case, PS/PMMA-GO the bandgap of the membranes significantly decreases from 4.11 eV to 3.59 eV, GO nanofillers seem to play a crucial role in modifying the bandgap [41].

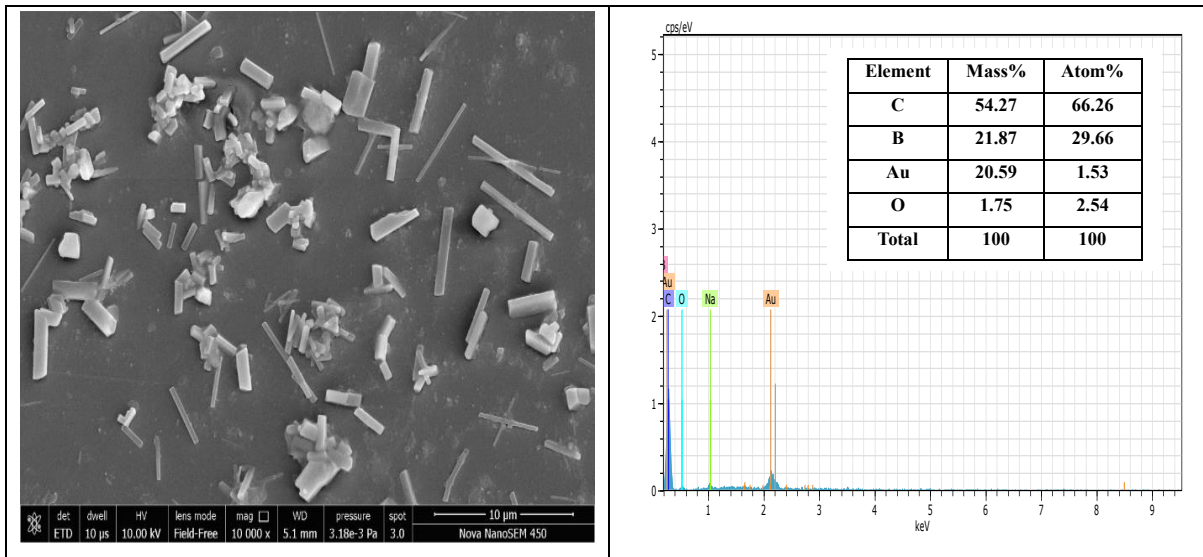
To determine the lowest photon energy required to move electrons from the valence band (VB) to the conduction band (CB), one can utilize the normal absorption boundary region. Various methods can be used to calculate the bandgap, which is typically expected to be near the absorption edge. Additionally, changes in absorption edges can occur due to the breaking and reformation of conjugated bonds, as revealed from FT-IR spectra.

4.1.3.7 FE-SEM Morphology and EDX

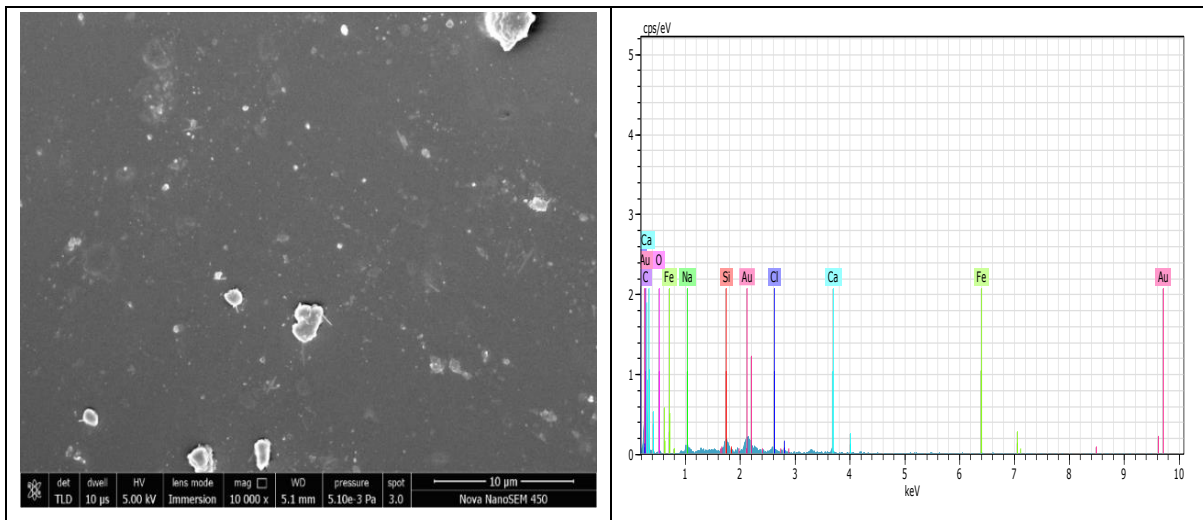
Figure 4.1.11 shows FE-SEM images of nanocomposite of PS/GO, nanocomposite of PMMA/GO and blend nanocomposite of PS₅₀/PMMA₅₀-GO polymer membranes. Instrumental details of FE-SEM and EDX have been discussed in chapter 2.



(I)



(II)



Element	Mass%	Atom%
C	40.51	71.95
Fe	20.77	7.93
Au	14.58	1.58
Na	7.11	6.60
Ca	6.12	3.26
Cl	4.62	2.78
Si	4.35	3.31
O	1.95	2.60
Total	100	100

(III)

Figure 4.1.11: SEM micrograph and EDX spectra of **(I)** nanocomposite membrane of PS/GO (1 wt%) **(II)** nanocomposite membrane of PMMA/GO (1 wt%) **(III)** blend membrane of PS₅₀/PMMA₅₀ composite with GO

Figure 4.1.11 shows the excellent dispersion of graphene oxide nanofillers within PS, PMMA polymers and blend of PS/PMMA membranes. The SEM images confirm the presence of PS/PMMA polymers and GO nanofillers in a homogeneous structure, which is likely to support favourable cell growth. Additionally, all composites shows good porosity and interconnectivity, although the morphology undergoes changes with the addition of 1 wt% of GO content. In the SEM image of the PS₅₀/PMMA₅₀ nanocomposite, it is visible that the 1 wt% of GO nanofillers are well-dispersed within the PS/PMMA blend. Several studies have shown that the addition of GO can enhance the mechanical and rheological properties of polymer composite membranes, and this is attributed to the strong interfacial interactions between pure, blend of PS/PMMA polymers and the nanocomposite with 1 wt% of GO fillers [42].

Specifically, in Figure 4.1.11 (I), the cross-sectional view of PS/GO (1 wt%) indicates the presence of large pores and numerous micropores, contributing to an increased active surface area. This increased surface area leads to a higher absorption capacity for the material being developed. Furthermore, as shown in Figure 4.1.11, it is observable that the addition of 1 wt% of GO has a significant impact on achieving uniform dispersion and controlling pore size during the synthesis of polymer PS/PMMA blend composites with GO nanofiller [42].

The Energy Dispersive X-ray (EDX) analysis provided valuable information on the carbon content and atomic percentages in the nanocomposite membranes containing PS and PMMA polymers. The results summarized in Figure 4.11 with the following outcomes:

1. For PS/GO in Figure 4.1.11 (I), the EDX analysis showed a carbon mass percentage of 67.41% and an atomic percentage of 97.11% for carbon elements. This suggests a high carbon content in the PS/GO nanocomposite [43].

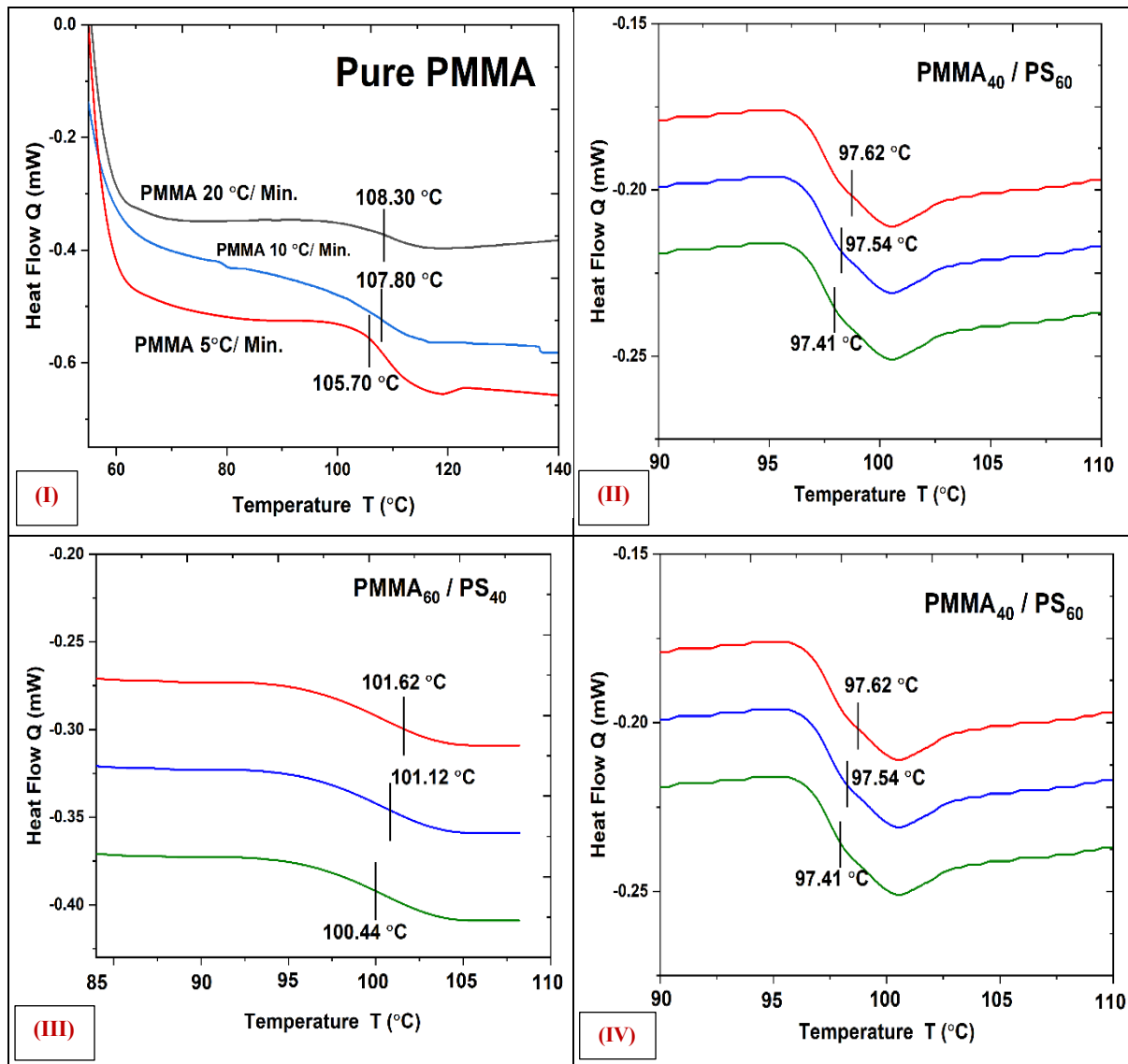
2. In the case of PMMA/GO observed from Figure 4.11 (II), the carbon mass percentage was found to be 54.27%, with an atomic percentage of 66.26% for carbon elements. While still substantial, these values are lower than those for PS/GO. This decrease in carbon content can be attributed to the fact that PMMA belongs to the acrylic family of polymers, which typically contain lower carbon content than styrene-based polymers like PS [43].

3. Figure 4.1.11 (III) shows that in another composites, the mass and atomic percentages of carbon elements are 40.51% and 71.95%, respectively. This composite appears to have a lower carbon content compared to both PS/GO and PMMA/GO [43].

In all EDX spectra, other elements are also present in the material, such as Au, O, Na, Fe, Ca, etc., indicating the blend composite of PS/PMMA-GO respectively. The EDX spectra also show additional peaks that suggest modifications in the polymer microstructure. These modifications have been confirmed in the SEM image shown in Figure 4.1.11 (III). The blending of PS and PMMA leads to changes in void spaces, which can affect the selectivity of the material for specific gases. Furthermore, SEM images also confirm the existence of GO nanoparticles within the polymer matrix. The dispersion of these nanoparticles in synthesized blend materials is uniform in nature. There is a sign of graphene oxide nanoparticles on the surface, may be due to their unique surface properties [42,43]. This surface behaviour could have implications for the interactions of material with its surroundings and its potential applications.

4.1.3.8 Differential Scanning Calorimetry (DSC)

PMMA and PS blends were developed by modifying the molecular weights of PMMA to prevent solvent-induced crystals from forming. All the parameters of DSC instrument has been discussed in chapter 2. Two T_g overlapped in PS/PMMA immiscible blends of 93 °C and 100 °C. The DSC thermograms showed that the PS melting peak was not visible in these Blend. At all compositions, the blend membranes were transparent for PS/PMMA [44]. Blends were heated at a temperature up to 90 °C above T_g for a week before cooling to room temperature and then quenching to see whether they were miscible at equilibrium.



PMMA:PS:GO (50:50:1)

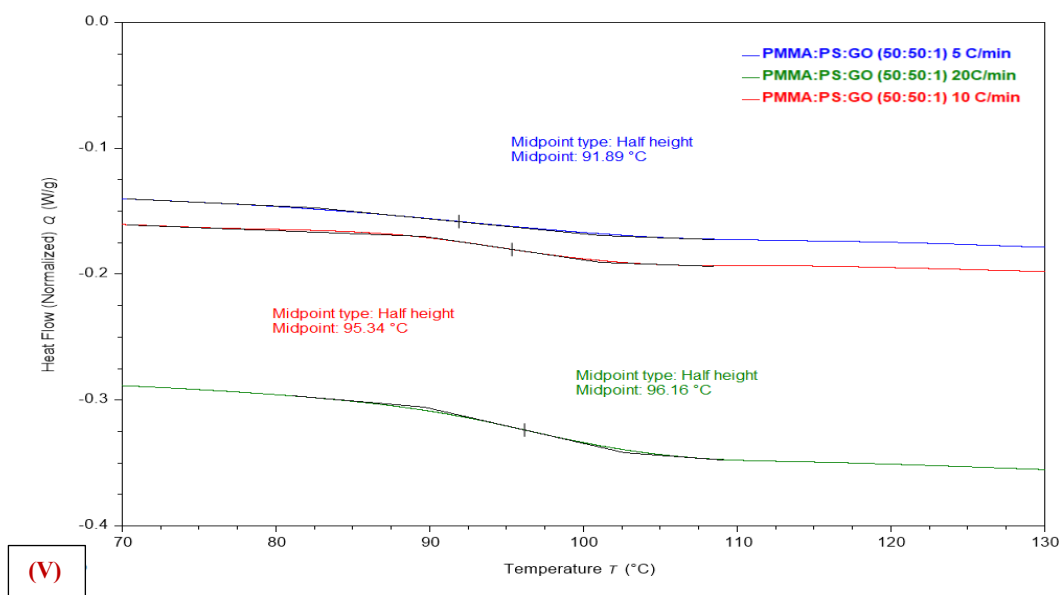


Figure 4.1.12: The DSC thermogram from (I - IV) Pure PMMA, Pure PS and blends of PS/PMMA and (V) blend of PS/PMMA composite with GO nanofillers

Figures 4.1.12 (I - IV) show the T_g values for the different weight ratios for PS/PMMA polymer blends. Furthermore, a DSC experiment is conducted to examine the impact of PMMA in PMMA/PS blends with various concentrations on the T_g value. It is observed when we increase the heating rate temperature from 5 °C/min to 20 °C/min, the glass transition temperature has been also increased according to that heating rate. To blend thin membrane with a ratio of PMMA₅₀- PS₅₀ the experimental value of T_g is around 97 °C, which also confirms the observed behaviour of heterogeneous polymeric systems [41].

Table 4.1.2 show the values of PMMA/GO and PS/GO and PMMA-PS/GO blend composites. Here the value of glass transition for PMMA/GO composite is 98.98 °C at a heating rate of 5 °C/min and for 10 °C/min and 20 °C/min, values are 99.19 °C and 100.72 °C. In the case of the composite of PS/GO the value of glass transition is 92.81°C for 5 °C/min, 93.57 °C for 10 °C/min and 95.57 °C for 20 °C/min.

Table 4.1.2: Glass transition temperature (T_g) value of pure, blend polymers and blend composite materials

Material	Glass transition Temperature (T_g) (°C)
Pure PS	95
PS PMMA	107
PMMA₈₀ / PS₂₀	102
PMMA₆₀ / PS₄₀	101
PMMA₄₀ / PS₆₀	97
PMMA₂₀ / PS₈₀	95
PMMA₅₀ / PS₅₀	97
PS / 1 wt% of GO	99
PMMA / 1 wt% of GO	93
PMMA₅₀ / PS₅₀ 1 wt% of GO	95

For, a nanocomposite blend of PS₅₀-PMMA₅₀ with graphene oxide, the glass transition value is likely 91.89 °C for 5 °C/min, 95.34 °C for 10 °C/min and 96.16 °C for 20 °C/min

For, a nanocomposite blend of PS₅₀-PMMA₅₀ with graphene oxide, the glass transition value is likely 91.89 °C for 5 °C/min, 95.34 °C for 10 °C/min and 96.16 °C for 20 °C/min heating rate, which is observed in Figures 4.1.12 (V). According to these observations, all of the PS/PMMA (80:20), PS/PMMA (50:50), and PS/PMMA (40:60) blends are miscible while in equilibrium, also T_g values observes from Table 4.1.2. Furthermore, because of the addition of graphene oxide, blended nanocomposite polymer membranes have a higher glass transition than pure and blended polymer membranes. These phenomena happened because of a decrease in fractional free volume. Graphene oxide plays a significant role as we composite the pure and blend of pure with graphene oxide; the glass transition increased compared to pure and blend of polymer of PS and PMMA, due to the functional groups in graphene, including the epoxide, carboxyl, and hydroxyl groups [44].

4.1.3.9 Calculation of Activation Energy

Activation energy (E_a), in the context of chemical reactions, has a physical meaning related to the energy barrier that reactant molecules must overcome to transform into products. The physical meaning of activation energy can be understood in the following ways: energy barrier for reaction, activation energy represents the minimum amount of energy required for a chemical reaction to occur. This barrier is often associated with breaking certain chemical bonds in the reactants, allowing new bonds to form in the products [45].

- **Iso-conversional Methods:**

Many approaches have been devised to analyze the crystallization process, most of them use Kolmogorov, Johnson, Mehl, and Avrami's (KJMA) transformation rate PS₇₅/PDMS₂₅ [42]. The iso-conversional methods are independent of the reaction model and give reliable activation energy values. They are classified as differential and integral methods i.e., Ozawa-Flynn-Wall (OFW) Method, Kissinger-Akahira-Sunose (KAS) Method, Boswell Method, Augis and Bennett's Method.

- ❖ **Approaches to Iso-Conversion Based on Linear Integrals:**

- **Ozawa-Flynn-Wall (OFW) Method:**

Ozawa, Flynn, and Wall employed an estimate proposed by Doyle in their technique [43]. The amount of energy taken by a collection of atoms in the glassy region to move from one state to another is known as the glass transition activation energy. Here, we could find the activation energy by using this Ozawa-Flynn-Wall (OFW) plot, which has been observed from Figure 4.1.13. The activation energy of pure PS is 86 kJ/mol⁻¹ and for pure PMMA has been

found 212 kJ/mol^{-1} . When we increased the wt% of PMMA in PMMA/PS blend then activation energy is increasing higher than PS and not above the activation energy of PMMA, this happened because of the miscible and glassy behaviour of both polymers, which is observed in Figure 4.1.13 (I).

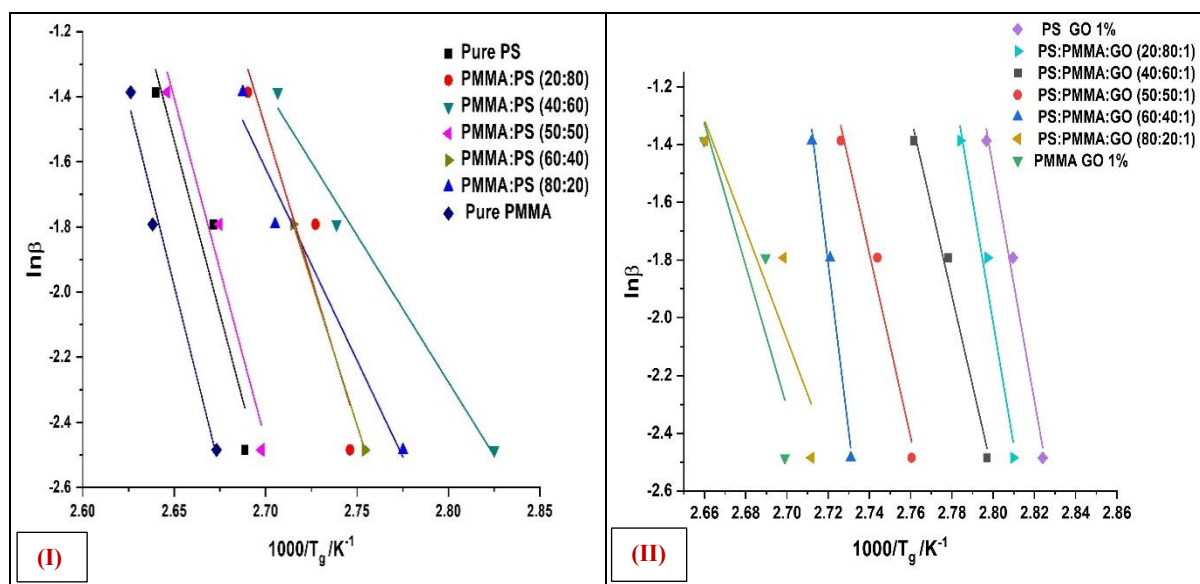


Figure 4.1.13: Ozawa-Flynn-Wall (OFW) plot of (I) Pure and Blends of PMMA/PS polymer (II) blend composite of PMMA-PS/GO

Figure 4.1.13 (II) the activation energy (E_a) of pure PS/GO its value is 157 kJ/mol^{-1} and for PMMA/GO has been found at 485 kJ/mol^{-1} [41]. When we increased the wt% of PMMA in PMMA-PS/GO nanocomposite blends the activation energy increased higher than PS but not above the activation energy of PMMA, this happened because of the miscible and glassy behaviour of both polymers and the presence of graphene oxide. In comparison to pure polymers and blends of polymers, the value activation energy increases when graphene oxide has been composites with PS/PMMA blends [42, 43].

- **Kissinger-Akahira-Sunose (KAS) Method:**

Coats and Redfern provided an estimate in their paper employed in this KAS technique. This technique assumes that the rate of reaction is most significant at the peak temperature (T_p), implying a constant degree of conversion (α) at T_p . Here, the activation energy from Figure 4.1.14 (I) is calculated on the plot of Kissinger-Akahira-Sunose (KAS) for pure PMMA it is found 216 kJ/mol^{-1} and for pure PS it is 88 kJ/mol^{-1} and the value of activation energy increases as we increased the wt% of PMMA in the blends of PMMA/PS.

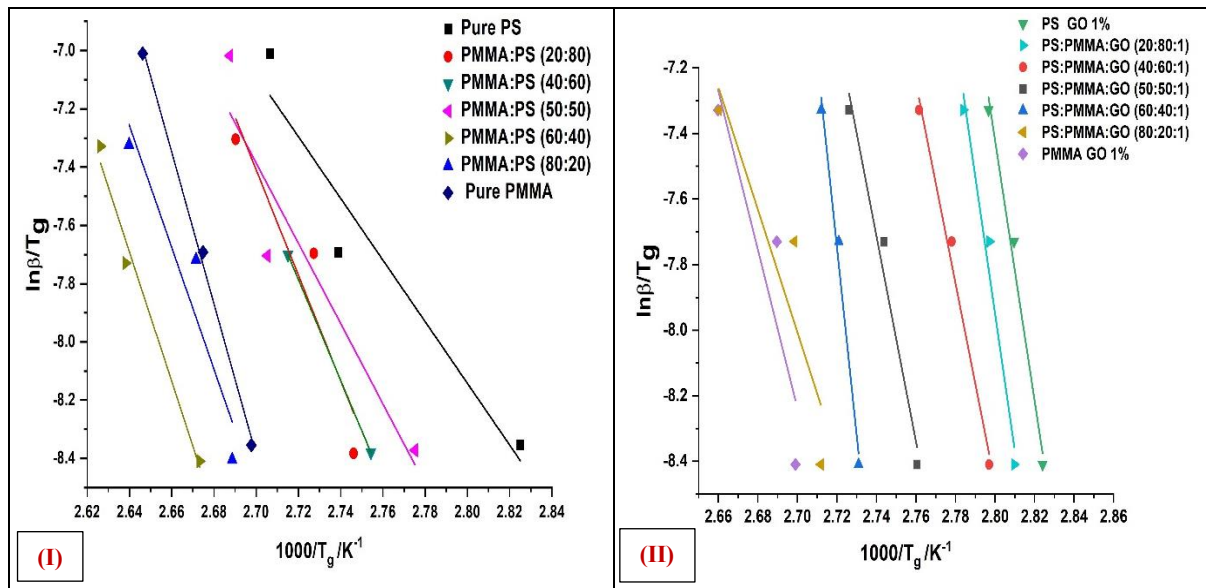


Figure 4.1.14: Kissinger-Akahira-Sunose (KAS) plot of (I) Pure and Blends of PMMA/PS polymer and (II) Blend Composite of PMMA-PS/GO

Moreover, from this plot, we can also observe as we go from pure PS to PMMA the value of intercept slop is also increasing for PS its value is 10.21 and for PMMA is 26.02 [46]. This graph shows that OFW and KAS results are near to one another, but Friedman’s points are much more dispersed.

• **Boswell Method:**

The activation energy at peak temperature (T_p) may be calculated using this approach proposed by Boswell [46].

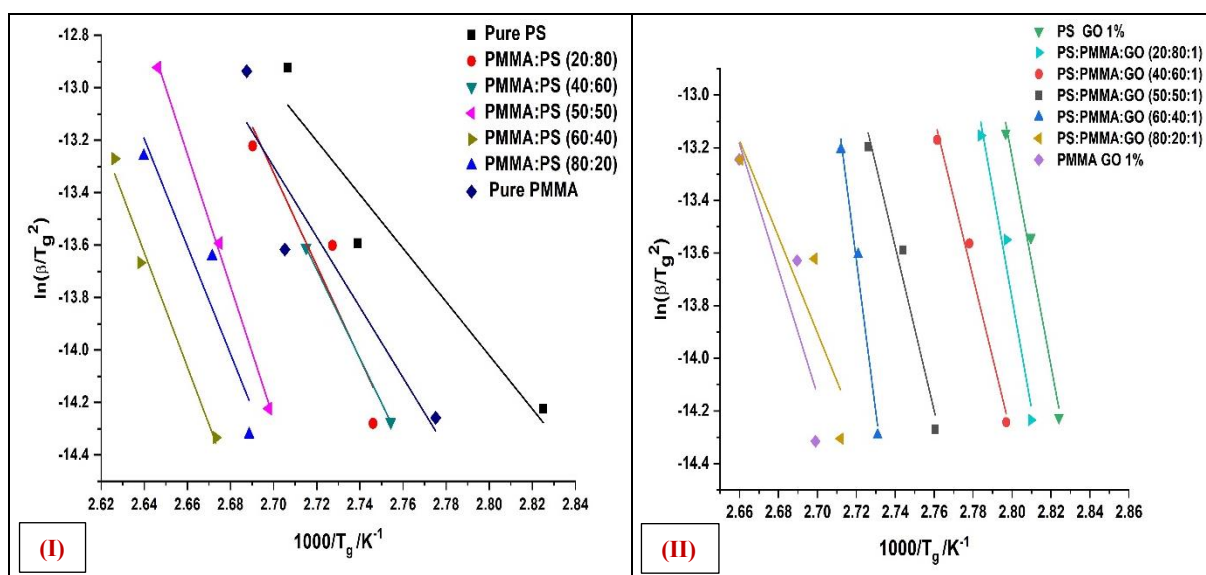


Figure 4.1.15: Boswell plot of (I) Pure and Blends of PMMA/PS polymer and (II) Blend Composite of PMMA-PS/GO

From this plot of Figure 4.1.15 (I) Boswell for membranes, we calculated activation energy for PS and PMMA and blends of PMMA/PS. The value of activation energy (A.E) for PS is 87 kJ/mol^{-1} and the slope value is 10.56 and for PMMA the value A.E is 219 kJ/mol^{-1} and slope value is 26.02 [46]. From this plot of Figure 4.1.15 (II) of Boswell for membranes, we calculated activation energy for PS/GO and PMMA/GO and blended the composite of PMMA₅₀-PS₅₀/GO. The value of activation energy (A.E) is 155 kJ/mol^{-1} for PS/GO and the slope value is 18.7 and for PMMA/GO the value A.E is 347 kJ/mol^{-1} and the slope value is 57.4 and for PMMA₅₀-PS₅₀/GO the value of A.E is 260 kJ/mol^{-1} and the slope value is 30.5 [47].

• Augis and Bennett's Method:

Augis and Bennett indicated that this approach might be used for heterogeneous processes given by the Avrami.

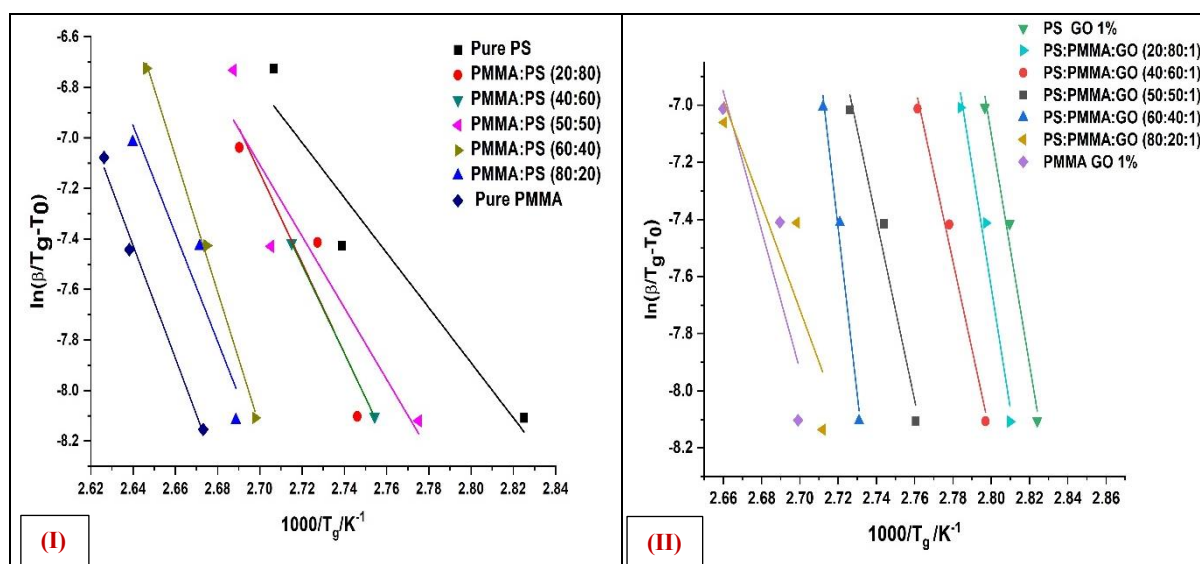


Figure 4.1.16: Augis and Bennett's plot of (I) Pure and Blends of PMMA/PS polymer and (II) Blend Composite of PMMA-PS/GO

Here, The activation energy is calculated from the Augis and Bennett's plot from Figure 4.1.16 (I) for pure PMMA it is found 221 kJ/mol^{-1} and for pure PS it is 92 kJ/mol^{-1} and the value of activation energy increases as we increased the wt% of PMMA in the blends of PMMA/PS [47]. Moreover, from these plots, we can also observe as we go from pure PS to PMMA the value of intercept slope is also increasing for PS its value is 10.89 and for PMMA is 26.68. Here, in Figure 4.1.16 (II) the activation energy was calculated for pure PMMA/GO; it is found at 485 kJ/mol^{-1} and for pure PS/GO, it is 152 kJ/mol^{-1} . An increase in the weight percentage of PMMA in the PMMA-PS/GO blends improved the activation energy value [46, 47]. Here, Table 4.1.3 represents the activation energy of pure PS, pure PMMA, blends of

PMMA/PS and blends composites of PS-PMMA/GO calculated from iso-conversional methods plots. The non-isothermal characterization kinetics of the present glassy polymer may thus be studied using Augis and Bennett's method.

Table 4.1.3: Activation energies (E_a) of Pure PS and PMMA and the Blends of PMMA/PS calculated from Iso-conversional methods plots:

Material	Method			
	Ozawa	Kissinger	Boswell	Augis and Bennett
	kJ/mol^{-1}			
Pure PS	86	84	87	90
Pure PMMA	212	216	219	221
PMMA ₈₀ -PS ₂₀	178	181	184	185
PMMA ₆₀ -PS ₄₀	168	170	173	177
PMMA ₅₀ -PS ₅₀	146	147	150	148
PMMA ₆₀ -PS ₄₀	139	140	143	145
PMMA ₂₀ -PS ₈₀	111	111	114	117
PS + 1 wt% of GO	157	151	155	152
PMMA + 1 wt% of GO	485	479	477	485
PMMA ₈₀ /PS ₂₀ + 1 wt% of GO	352	346	347	352
PMMA ₆₀ /PS ₄₀ + 1 wt% of GO	335.	329	330	334
PMMA ₅₀ /PS ₅₀ + 1 wt% GO	264	258	260	262
PMMA ₆₀ /PS ₄₀ + 1 wt% of GO	258	252	253	256
PMMA ₂₀ /PS ₈₀ + 1 wt% of GO	204	197	200	202

The activation energy and pre-exponential factor may be obtained using iso-conversional techniques (k_0). Using both iso-kinetic and iso-conversional approaches, the kinetics of characterization are examined. This approach of linear differential iso-conversion is believed to yield accurate estimates of the activation energy [47]. As a result, no assumptions about the reaction model are required. This indicates that the approach is unaffected by the reaction model.

4.1.3.10 Thermogravimetric Analyzer (TGA)

Analysis of polymer thermal decomposition using thermogravimetric analyzer (TGA) has often used to determine kinetic parameters including activation energy and the parameter of TGA instrument has been detail discussed in chapter 2. TGA thermograms showing weight loss vs temperature are shown in Figure 4.1.17 for different nanocomposite blends of PMMA/PS-GO with varied weight ratios of PMMA, PS and all the thermal curves of different samples observed at a heating rate of 5 °C/min, between 50 °C and 600 °C.

At temperatures between 80 °C and 110 °C, moisture evaporation causes the first weight loss in all samples; after reaching 130 °C, the samples become unstable owing to the evaporation of the solvent. All samples show the most significant weight loss at decomposition temperatures (T_d) between 340 °C and 430 °C [48]. At the temperature of 340 °C, about 90% of the material is degraded. The process of weight loss and the evaporation of degradation products increases during this phase. When temperatures exceed 400 °C, roughly 6 % to 7 % of weight loss occurs.

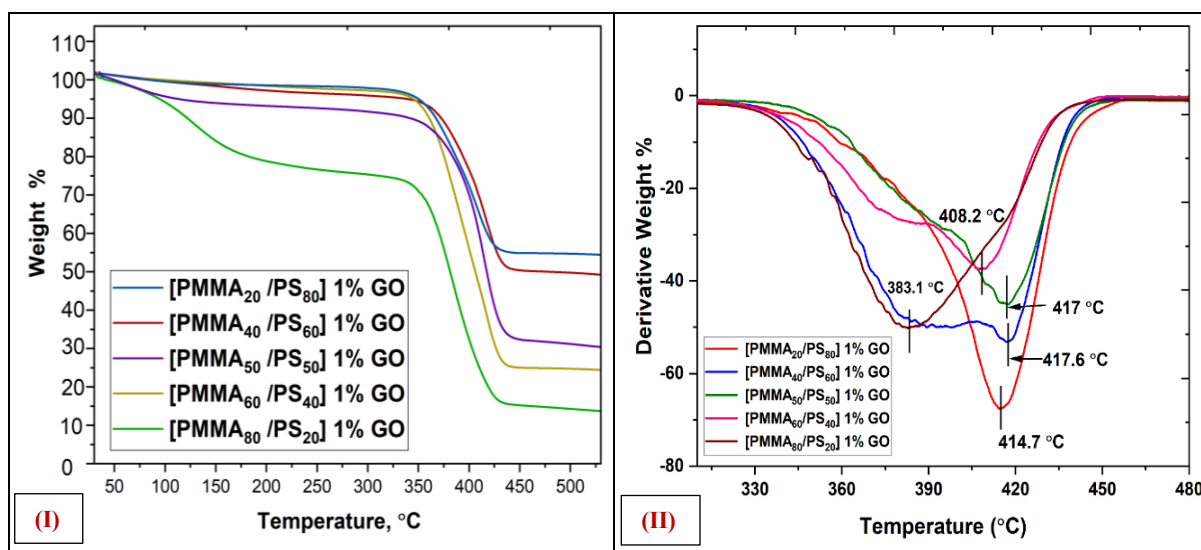


Figure 4.1.17: (I) Thermogravimetric analysis (TGA), (II) Curves of differential thermal analysis (DTA) of various nanocomposite blends of [PMMA/PS] (1% of GO)

This could be related to the structural breakdown of the polymer mixtures. Figure 4.1.17 shows TGA curves of nanocomposite blend membranes, which indicate that adding GO nanoparticles to the PMMA/PS blend increases the thermal stability material. PMMA thermal degradation is primarily due to the breakdown of C-C bonds, which proceeds through the decomposition of head-head bonds, the breakage of vinyl groups at the polymers ends, and the random breaking of polymeric chains. For the nanocomposites, two different phases of weight reduction have shown in the thermogram [47,48]. Initial processing involves solvent removal and polymer end degradation. At this point, graphene oxide contributes to the polymer increasing stability. The weight loss percentage is more significant in the second stage, when the polymer chain is broken down.

This is due to the impact of GO nanofillers. The heating has a good influence on thermal stability, as seen by the increase in char percentage. According to the findings, the amount of the inorganic component injected affects how much strength is increased. The addition of the inorganic component greatly decreases the thermal breakdown of PMMA polymer [49].

Table 4.1.4: Decomposition temperatures of nanocomposite blends of [PMMA/PS] with GO at different percent weight loss

Nanocomposite	Stage 1	Stage 2	T _{max} (°C)
[PMMA ₂₀ /PS ₈₀] 1% of GO	4.70%	92.30%	414
[PMMA ₄₀ /PS ₆₀] 1% of GO	4.55%	97.01%	417
[PMMA ₅₀ /PS ₅₀] 1% of GO	4.60%	98.60%	417
[PMMA ₆₀ /PS ₄₀] 1% of GO	8.62%	93.45%	408
[PMMA ₈₀ /PS ₂₀] 1% of GO	38.40%	105.55%	383

A blend of PMMA/PS had a much greater weight loss ratio overall compared to the performance of comparable nanocomposites. Based on the data in Table 4.1.4, it was determined that the polymer chains and inorganic particles, thus, PMMA and PS polymer matrix breakdown caused by heat were decreased. The results show that the T_{dmax} of pure PMMA and PS polymers has shifted towards higher values by the increasing weight percentage of PMMA and the addition of graphene oxide nanoparticles to the polymer matrix, compared with pure PMMA, PS, and blend of PMMA/PS. There is significant weight loss in stages 1 and 2 for the [PMMA₈₀/PS₂₀] with 1% GO samples; because of the higher weight percentage

of PMMA polymer compared to PS polymer, and due to more C-C bonds breaking, therefore it is creating more fraction free volume. An important peak in the derivative thermogravimetry (DTG) curve occurs around 414.7 °C. The DTG curve rapidly increases in temperature to a peak at 383.1 °C. This is the link in the chain the breaking apart of polymers into monomers and smaller building blocks such as dimers, trimers, tetramers, and pentamers [48,49].

4.1.3.11 X - ray Diffraction

XRD (Rigaku Smartlab) has been recorded with $\text{CuK}\alpha$ radiation at 80 keV with a wavelength of 1.5406 Å respectively, details of XRD has been discussed in chapter 2. Graphene oxide nanoparticles, pure PS, pure PMMA and PS/GO, and PMMA/GO blended composite membranes of XRD patterns have been seen in Figure 4.1.18. Sharp peaks of the graphene oxide have been observed, which indicates the crystalline nature of the product. There are structural changes in polymer nanocomposites when GO nanoparticles are included. In polymer nanocomposites, including nanoparticles, the X-ray diffraction pattern has sharp and diffuse peaks [49].

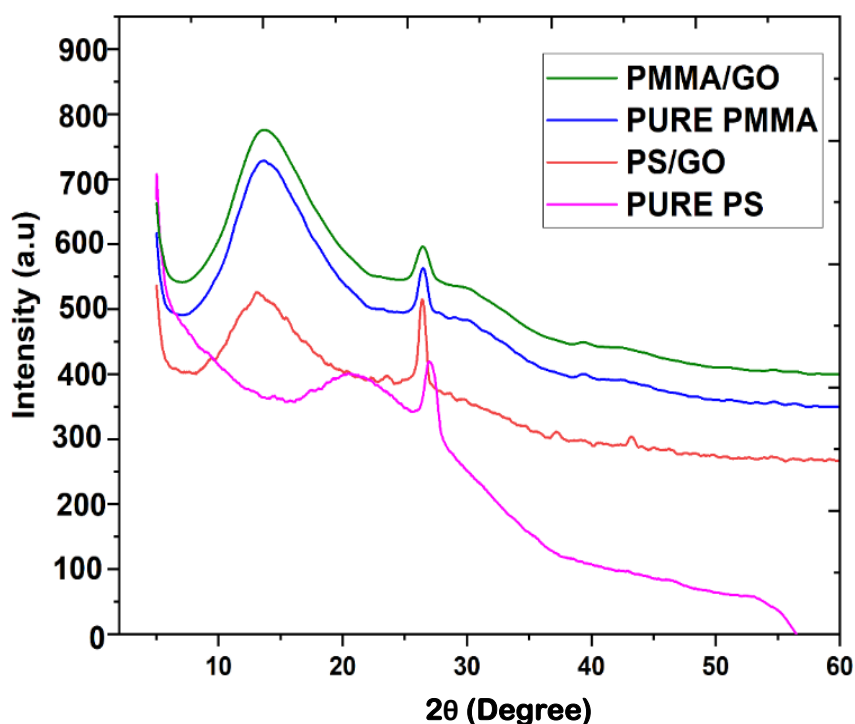


Figure 4.1.18: XRD of Pure PMMA, PMMA/GO, PS/GO and Pure PS nanocomposite polymer membranes

All the blend composites show a broad and diffuse peak, which indicates the amorphous nature of the blends. X-ray diffraction (XRD) analyses confirm the crystalline phase transition of GO. Crystallized PS/GO and PMMA/GO composites from a series of composite solvents have shown XRD patterns in Figure 4.1.18. The PMMA/GO diffractogram (Figure 4.1.18)

shows the characteristic scattering peak at an angle of 13.22° , which corresponds to the superposition of (1 0 0) and (2 0 0) reflections for the β phase of graphene oxide. At around 10° , the scattering from the -COOH groups in the graphite-like GO sheets causes this peak, which is usually seen at this distance. Figure 4.1.18 shows two broad peaks of PMMA/GO and pure PMMA at angles 13.22° and 13.32° , showing that PMMA is amorphous in nature. In the first half, the side group size corresponds to an approximately hexagonal arrangement of the molecular chains. When graphene oxide has not disseminated in an aqueous solution, the XRD spectrum shows additional peaks between 10° - 45° that are typical of graphene oxide. This suggests that between two and ten overlapping GO layers may be present. As the graphene oxide has dispersed, the sheets separate, and the GO has reshaped, thus this no longer matters for making the scaffolds. In addition, the miscibility of the polymer blends has been determined by the XRD scans of the polymer blends [50]. The relative x-ray peak intensities allow us to evaluate the volume percentage of the graphene oxide phase generated in the samples, it shows the 2θ and d spacing lattice characteristics for all samples. The lattice parameters observed for pure PS and pure PS/GO are 2θ of (PS) = 20.83° , 2θ of (PS/GO) = 13.06° and d spacing for pure (PS) = 8.31 \AA , d spacing for (PS/GO) = 7.64 \AA . As the concentration of GO in the sample increases, we see a little shift of the diffraction peaks towards higher angles. This indicates that the lattice parameters of the composite samples are somewhat less than those of the pure polymer. The intensity and height of the two peaks changes as the PS level in the atmosphere increased [51]. Using this information, we may conclude that the mixture were miscible. Our results show that the amount of carbon composite in GO samples is negligible compared to other carbon sources. Our analysis of the XRD patterns confirms that the crystallite size and crystallinity of the materials are decreased due to polymer composite with GO, as the full width at half maximum (FWHM) increases with the increasing composite concentration of GO in the pure polymer samples. These materials showed an amorphous nature since no clear diffraction peak could be seen in the 2θ angle range. All results of XRD patterns confirmed that PMMA/GO and PS/GO was amorphous polymer, which means PMMA and PS have amorphous nature [52].

4.1.4 Conclusion

The performance of the modified membranes, as analyzed in terms of permeability and selectivity, indicates alterations in the transport of hydrogen molecules. In both PS and PMMA nanocomposites, the presence of GO nanoparticles plays a significant role in improving the mechanisms for transporting hydrogen molecules. Furthermore, increasing the quantity of

graphene oxide nanofillers leads to an expansion of free space within the membrane, subsequently enhancing its permeability. The graphene composite allows for improved access of penetrants, making them more soluble within the membrane material, resulting in higher permeability. It is worth noting that Robeson's 2008 upper bound, which sets limits on membrane separation factors for various gas pairs, is well-suited for the gas pairings determined in this study. Specifically, the H₂/O₂ gas pair is an excellent example of a gas pair that falls within the upper bounds for novel gas separation membrane composites. This suggests that the nanocomposite membranes have the potential to be highly efficient in separating these gases, which could have important applications in various industries.

It was observed that the thermal and thermal properties of graphene oxide dispersion in the pure PS, Pure PMMA and blends of PS/PMMA where T_g was decreased as expected by increasing graphene oxide content compared to PS, PMMA and PS/PMMA blends of polymers. In the FT-IR spectra of the two polymers and their mixtures, several kinds of bands have been observed. Originally, Augis and Bennett's technique has used to determine the highest possible temperatures for crystallization to occur. It is important to note that activation energy values obtained using different iso-conversional approaches and particular iso-conversional techniques, such Ozawa, Kissinger, Boswell, and Augis and Benett, are very similar to one another. This underscores the importance of the interactions and modifications brought about by GO in these nanocomposite membranes, which have implications for their performance in various applications, particularly in gas separation processes.

References:

- [1] R. J. Kadhim, F. H. Al-Ani, M. Al-Shaeli, Q. F. Alsalhy, A. Figoli, Removal of dyes using graphene oxide (GO) mixed matrix membranes, *Membranes*, **2020**, 10, 1–24.
- [2] H. Y. Cheng, G. J. Jiang, J. Y. Hung, Enhanced mechanical and thermal properties of PS/mica and PMMA/mica nanocomposites by emulsion polymerization, *Poly. Composite*, **2009**, 30, 1–6.
- [3] N. N. Rozik, A. I. Khalaf, A. A. Ward, Studies the behaviours of polyaniline on the properties of PS/PMMA blends, *Part L: J. of Materials: Design and Applications*, **2016**, 230, 26–36.
- [4] N. Widjojo, T. S. Chung, Thickness and air gap dependence of macrovoid evolution in phase-inversion asymmetric hollow fibre membranes, *Ind. Eng. Chem. Res.*, **2006**, 45, 7618-7626.

- [5] N. K. Acharya, V. Kulshrestha, K. Awasthi, A. K. Jain, M. Singh, Y. K. Vijay, Hydrogen separation in doped and blend polymer membranes, *Int. J. Hydrogen Energy*, **2008**, 33, 27–31.
- [6] M. A. Aldosari, K. B. Alsaud, A. Othman, M. Al-Hindawi, N. H. Faisal, R. Ahmed, et al., Microwave irradiation synthesis and characterization of reduced-(Graphene Oxide-(Polystyrene-Polymethyl Methacrylate))/Silver Nanoparticle nanocomposites and their anti-microbial activity, *Polymers*, **2020**, 12, 52-65.
- [7] E. Sharifzadeh, M. Salami-Kalajahi, M. S. Hosseini, M. R. Aghjeh, Synthesis of silica Janus nanoparticles by buoyancy effect-induced desymmetrization process and their placement at the PS/PMMA interface, *Colloid. Poly. Sci.*, **2017**, 295, 25–36.
- [8] V. Mathur, K. Sharma, Thermal response of polystyrene/poly methyl methacrylate (PS/PMMA) polymeric blends, *Heat and Mass Transfer*, **2016**, 52, 01–11.
- [9] G. G. Silva, P. M. de Freitas Rocha, P. S. de Oliveira, B. A. Neves, Domain size effects on the thermal properties of PS/PMMA blends, *Appl. Surf. Sci.*, **2004**, 238, 64–72.
- [10] I. S. Tsagkalias, T. K., Manios, D. S. Achilias, Effect of graphene oxide on the reaction kinetics of methyl methacrylate in situ radical polymerization via the bulk or solution technique, *Polymers*, **2017**, 15, 165-182.
- [11] T. H. Min, C. J. Lee, H. J. Choi, Pickering emulsion polymerized core-shell structured poly(methyl methacrylate)/graphene oxide particles and their electrorheological characteristics, *Polym. Test*, **2018**, 66, 195–202.
- [12] A. K. Patel, N. K. Acharya, *Study of Gas Permeation for Polymer Blend and Composite Membranes*, **2019**.
- [13] L. M. Robeson, The upper bound revisited, *J. Memb. Sci.*, **2008**, 320, 390–400.
- [14] A. K. Patel, N. K. Acharya, Thermally rearranged (TR) HAB-6FDA nanocomposite membranes for Hydrogen separation, *Int. J. Hydrogen Energy*, **2020**, 45, 85–92.
- [15] P. S. Tin, T. S. Chung, Y. Liu, R. Wang, S. L. Liu, K. P. Pramoda, Effects of cross-linking modification on gas separation performance of Matrimid membranes, *J. Memb. Sci.*, **2003**, 90, 225-277.
- [16] H. D. Patel, N. K. Acharya, Synthesis and characteristics of HAB-6FDA thermally rearranged polyimide nanocomposite membranes, *Polym. Eng. Sci.*, **2021**, 61, 2782–91.
- [17] D. F. Sanders, Z. P. Smith, R. Guo, L. M. Robeson, J. E. McGrath, D. R. Paul, et al., Energy-efficient polymeric gas separation membranes for a sustainable future: A review, *Polymer*, **2013**, 54, 29–61.

- [18] H. Ravishankar, J. Christy, V. Jegatheesan, Graphene oxide (GO)-blended polysulfone (PSf) ultrafiltration membranes for lead ion rejection, *Membranes*, **2018**, 8-20.
- [19] R. J. Kadhim, F. H. Al-Ani, M. Al-Shaeli, Q. F. Alsalhy, A. Figoli, Removal of dyes using graphene oxide (GO) mixed matrix membranes, *Membranes*, **2020**, 10, 1–24.
- [20] M. Bhattacharya, Polymer nanocomposites-A comparison between carbon nanotubes, graphene, and clay as nanofillers, *Materials*, **2016**, 14, 132-148.
- [21] M. K. Pal, B. Singh, J. Gautam, Thermal stability and UV-shielding properties of polymethyl methacrylate and polystyrene modified with calcium carbonate nanoparticles, *J. Therm. Anal. Calorim.*, **2012**, 107, 85–96.
- [22] N. Abdullah, S. K. Kamarudin, L. K. Shyuan, N. A. Karim, Synthesis and optimization of PTRu/TiO₂-CNF anodic catalyst for direct methanol fuel cell, *Int. J. Hydrogen Energy*, **2019**, 44, 30543–52.
- [23] A. Iulianelli, A. Basile, Special issue on Hydrogen separation/purification via membrane technology, *Int. J. Hydrogen Energy*, **2020**, 45, 65-72.
- [24] H. V. Nguyen, T. A. Ngo, K. D. Do, Nguyen M. N., Dang N. T., Nguyen T. H., et al., Preparation and characterization of a hydrophilic polysulfone membrane using graphene oxide, *J. Chem.*, **2019**, 15, 1520-32.
- [25] M. A. Aroon, A. F. Ismail, T. Matsuura, M. M. Montazer-Rahmati, Performance studies of mixed matrix membranes for gas separation: A review, *Sep. Purif. Tech.*, **2010**, 75, 229–242.
- [26] B. D. Freeman, Basis of permeability/selectivity trade-off relations in polymeric gas separation membranes, *Macromolecules*, **1999**, 323, 75–80.
- [27] Y. K. Vijay, N. K. Acharya, S. Wate, D. K. Avasthi, Characterization of track etched membranes by gas permeation, *Int. J. Hydrogen Energy*, **2004**, 295, 15–9.
- [28] M. Pakizeh, M. R. Omidkhah, A. Zarringhalam, Synthesis and characterization of new silica membranes using template-sol-gel technology, *Int. J. Hydrogen Energy*, **2007**, 3218, 25–36.
- [29] V. Kulshrestha, N. K. Acharya, Awasthi K, Singh M, D. K. Avasthi, Y. K. Vijay, Study of gas permeation for asymmetric track-etched polymer blends, *Int. J. Hydrogen Energy*, **2006**, 3112, 66–70.
- [30] G. Bernardo, T. Araújo, T. da Silva Lopes, J. Sousa, A. Mendes, Recent advances in membrane technologies for Hydrogen purification, *Int. J. Hydrogen Energy*, **2020**, 4573,13–38.

- [31] X. Zhao, S. Chen, J. Zhang, W. Zhang, X. Wang, Crystallization of PVDF in the PVDF/PMMA blends precipitated from their non-solvents: Special orientation behaviour, morphology, and thermal properties, *J. Cryst. Growth*, **2011**, 328, 74–80.
- [32] A. Sargsyan, A. Tonoyan, S. Davtyan, C. Schick, The amount of immobilized polymer in PMMA SiO₂ nanocomposites determined from calorimetric data, *Eur. Polym. J.*, **2007**, 4331, 13–27.
- [33] S. S. Lock, K. K. Lau, N. Jusoh, M. Shariff, C. H. Gan, C. L. Yiin, An atomistic simulation towards molecular design of silica polymorphs nanoparticles in polysulfone based mixed matrix membranes for CO₂/CH₄ gas separation, *Polym. Eng. Sci.*, **2020**, 603, 197–215.
- [34] A. K. Jain, N. K. Acharya, V. Kulshreshtha, K. Awasthi, M. Singh, Y. K. Vijay, Study of Hydrogen transport through porous aluminum and composite membranes, *Int. J. Hydrogen Energy*, **2008**, 3334, 6–9.
- [35] A. P. Roberts, B. M. Henry, A. P. Sutton, C. M. Grovenor, G. D. Briggs, T. Miyamoto, M. Kano, Y. Tsukahara, M. Yanaka, Gas permeation in silicon-oxide/polymer (SiO_x/PET) barrier films : role of the oxide lattice, nano-defects and macro-defects, *J. Memb. Sci.*, **2002**, 208, 75–88.
- [36] S. S. Nayab, M. A. Abbas, S. Mushtaq, B. K. Niazi, M. Batool, G. Shehnaz, et al., Anti-foulant ultrafiltration polymer composite membranes incorporated with composite activated carbon/chitosan and activated carbon/thiolated chitosan with enhanced hydrophilicity, *Membranes*, **2021**, 11-30.
- [37] R. J. Kadhim, F. H. Al-Ani, M. Al-Shaeli, Q. F. Alsalhy, A. Figoli, Removal of dyes using graphene oxide (GO) mixed matrix membranes, *Membranes*, **2020**, 10,1–24.
- [38] J. F. Sark, N. Jullok, W. J. Lau, Improving the structural parameter of the membrane sublayer for enhanced forward osmosis, *Membranes*, **2021**, 12, 365-380.
- [39] A. Najjar, S. Sabri, R. Al-Gaashani, M. A. Atieh, V. Kochkodan, Antibiofouling performance by polyethersulfone membranes cast with oxidized multiwalled carbon nanotubes and arabic gum, *Membranes*, **2019**, 9-25.
- [40] X. Liu, J. Duan, J. Yang, T. Huang, N. Zhang, Y. Wang, et al., Hydrophilicity morphology and excellent adsorption ability of poly(vinylidene fluoride) membranes induced by graphene oxide and polyvinylpyrrolidone. *Colloids Surf. A. Physicochem. Eng.*, **2015**, 4861, 72–84.

- [41] Z. Guo, R. Xiu, S. Lu, X. Xu, S. Yang, Y. Xiang, Submicro-pore containing poly(ether sulfones)/polyvinylpyrrolidone membranes for high-temperature fuel cell applications, *J. Mater Chem. A. Mater*, **2015**, 388, 47–54.
- [42] Ronald P. D'Amelia-, Evan H. Kreth, Establishment of the Flory-Fox Equation for Polymethyl Methacrylate (PMMA) Using Differential Scanning Calorimetry (DSC), *J. of Poly. and Biopoly. Phy. Chem.*, **2023**, 11 (1), 1-10.
- [43] H. D. Patel, N. K. Acharya, Transport, Spectroscopic, and Electrical Properties of Thermally Rearranged Nanocomposite Membranes, *Chem. Eng. Technol.*, **2022**, 45(12), 2223–2233.
- [44] C. Khatuaa, I. Chinyaa, D. Sahab, S. Dasa, R. Sena, A. Dhara, Modified clad optical fibre coated with PVA/TiO₂ nano composite for humidity sensing application, *International Journal on Smart Sensing and Intelligent Systems*, **2015**, 814, 24–42.
- [45] A. K. Patel, N. K. Acharya, Metal coated and nanofiller doped polycarbonate membrane for Hydrogen transport, *Int. J. Hydrogen Energy*, **2018**, 216, 75–82.
- [46] S. W. Kuo, H. C. Kao, F. C. Chang, Chain interactions, and surface energies of PMMA terpolymers having high glass transition temperatures and Thermal properties, specific low moisture absorptions, *Polymer*, **2005**, 4623, 54–64.
- [47] S. Kumar, A. Sharma, B. Tripathi, S. Srivastava, S. Agrawal, M. Singh, et al., Enhancement of Hydrogen gas permeability in electrically aligned MWCNT-PMMA composite membranes, *Micron*, **2010**, 419, 09–14.
- [48] D. F. Sanders, Z. P. Smith, R. Guo, L. M. Robeson, J. E. McGrath, D. R. Paul, et al., Energy-efficient polymeric gas separation membranes for a sustainable future: A review, *Polymer*, **2013**, 5447, 29–61.
- [49] H. Y. Cheng, G. J. Jiang, J. Y. Hung, Enhanced mechanical and thermal properties of PS/mica and PMMA/mica nanocomposites by emulsion polymerization, *Polym. Compos.*, **2009**, 3035, 1–6.
- [50] Z. Hu, J. Mahin, L. Torrente-Murciano, A MOF-templated approach for designing ruthenium–cesium catalysts for Hydrogen generation from ammonia, *Int. J. Hydrogen Energy*, **2019**, 44301, 08–18.
- [51] N. Panapitiya, S. Wijenayake, D. Nguyen, C. Karunaweera, Y. Huang, K. Balkus, et al., Compatibilized immiscible polymer blends for gas separations. *Materials*, **2016**, 9, 325-340.
- [52] B. A. Mccool, Y. S. Lin, Nanostructured thin palladium-silver membranes: Effects of grain size on gas permeation properties, *J. Mater. Sci.*, **2001**, 36, 3221–3227.

Thermally Stable PET/PEG- DES/TiO₂ Polymer Blend Composites Membranes with Enhanced Properties for Food Packaging

4.2.1 Introduction

4.2.2 Experimental Set-up

4.2.2.1 Synthesis of Membranes

4.2.3 Result and Discussion

4.2.3.1 Gas-Barrier Properties

4.2.3.2 Diffusion and Solubility Coefficients

4.2.3.3 Porosity Analysis

4.2.3.4 Differential Scanning Calorimetry (DSC)

4.2.3.5 Thermogravimetric Analyzer (TGA)

4.2.3.6 Fourier Transform Infrared Spectroscopy

4.2.3.7 Contact Angle Analysis

4.2.3.8 Mechanical Properties

4.2.3.9 X-ray Diffraction

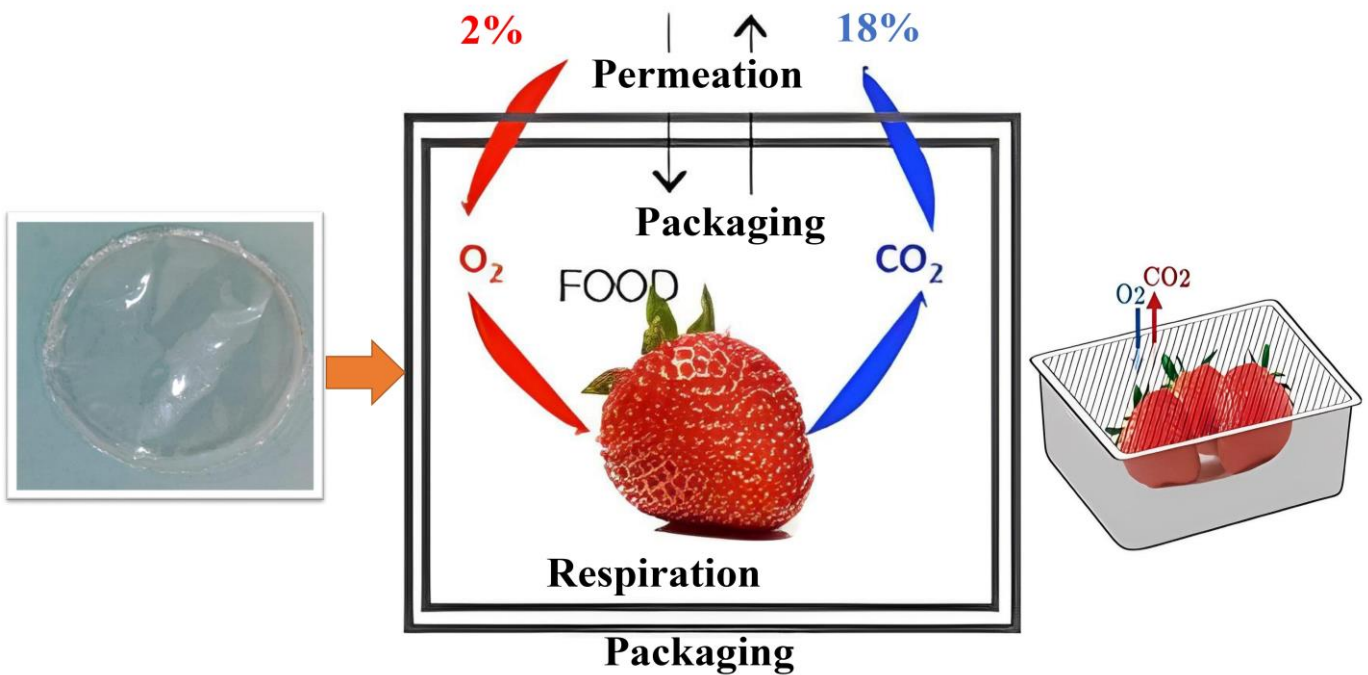
4.2.3.10 FE-SEM Morphology

4.2.4 Conclusion

References

Chapter – 4.2

Thermally Stable PET/PEG- DES/TiO₂ Polymer Blend Composites Membranes with Enhanced Properties for Food Packaging



The modification behaviour of permeability is necessary to increase food self life and identify the optimum technological solution in polymer membrane. For the preservation of food quality, temperature and humidity factors are very important, particularly in practical applications such as food markets and long-term home usage. The purpose of this chapter is to make that type of polymer material that gives low permeability of material that will use as packaging material in the food business. In present chapter, the study of gas permeability, thermal stability and mechanical properties of pure polyethylene terephthalate (PET), polyethylene glycol (PEG), their blends by various weight percentage ratios of PET: PEG (50:50 w/w%) and blend of PET/PEG composite with DES/TiO₂ nanofillers is reported. Permeability tests, a nanofillers of DES/TiO₂ composite with PET/PEG blends shows a change in permeability than that of pure and blend of polymers. Various gases including H₂, CO₂, N₂, Ar and O₂ were used for the permeability measurements. Data support the blending of PET/PEG composite with DES/TiO₂ nanofillers enhancement in barrier characteristics to O₂, especially improving the thermal and mechanical properties of material. Modified samples were allowed through various thermograms of PET, PEG, their blends and blend of PET/PEG composite with DES/TiO₂ nanofillers using DSC and TGA to optimize the glass transition temperature, weight loss and thermal stability of materials. SEM has been used to characterize the structural and morphological characteristics of these composite membranes. FT-IR was performed to identify the compounds formation between blends and composite membranes. In this study, particular attention to developing packaging materials' mechanical property, degradability, thermal stability, and antibacterial activity for various packaging applications.

4.2.1 Introduction

Food packaging membrane material to be very certain of both food safety and long-lasting durability, it needs an antibacterial environment with modified air permeability. Packaging material made of plastic, as opposed to glass or metal, are more permeable to small molecules, including gases, water vapour, and organic vapour, as well as other low molecular weight substances like food additives, flavours and smells. The transmission of these molecules varies from high to low due to the materials barrier characteristics [1,2]. In recent years, understanding how these molecules behave through polymer membranes has become extremely important, particularly for polymers used in the food packaging industry where contamination from the outside environment must be avoided and the use of modified atmosphere packaging (MAP) techniques must control the self life of the food. Compared to

most polymers, including polyethylene glycol (PEG), polyethylene (PE), and polypropylene (PP), polyethylene terephthalate (PET) is known for exceptionally low gas permeability. There are several PET variants on each with its own production method and unique features still, MAP applications need a higher barrier performance standard than PET [3].

Plastics property make them a popular material and it has been used to enhance cost-efficient carry bags. However, not all the plastics are the same and can not perform the same roles in all situations. Although many different types of plastic may seem and feel the same, the characteristics of the various types of plastic may significantly differ. Polyethylene glycol (PEG) and polyethylene terephthalate (PET) are two of the most regularly used polymers for food packaging applications. Both the PEG and PET are beneficial materials, but they are not similar and should not be used equally because of the differing qualities of the material properties, PEG and PET each have their own advantages and disadvantages. Outside heat is better resisted by PEG plastic than by PET and at the same time, PET plastic is far resistant to cold from the outside than PEG. Both PEG plastic and PET plastic have a broad temperature resistance range, and the advantage of one kind of plastic over the other is by small margins. In comparison to PEG plastic, PET plastic holds up much better and it easily beats PEG in terms of durability [4]. It is observed that the variation of physio-chemical properties in the final blend composition. PET is more resistant to O₂ permeation losses than that of other forms of plastic, it is often used for beverage packaging. Due to its low diffusivity, it is the most promising polymer for recycling as a material for food packaging (i.e., it prevents significant penetration of organic substances into the plastic). Due to its high degree of transparency, high degree of dimensional stability and strong thermal as well as mechanical properties PET is widely used. Additionally, it is commonly used to fabricate fibers, membranes, and packaging materials with intermediate barrier requirements. However, it is highly desirable to improve certain features in many applications, such as barrier properties for food packaging and beverage applications [5]. Thermal transitions and other PET structure-related features are significantly affected by this chain stiffness. A thermoplastic polymer with excellent processing characteristics, Polyethylene glycol (PEG) is used in various products, including furniture, toys, household items, and appliances and PET polymer is often used in applications for food packaging. Polymer blending is a quick and inexpensive way to create new desired property combinations without creating novel structures. Using a nanocomposite technique to create modified material using polymer nanocomposites, inherent limitations of polymer-based packaging materials may be overcome, such as poor mechanical qualities and low water

resistance. Titanium dioxide (TiO₂) is the strongest material and has exceptional mechanical, electrical, and thermal characteristics. Scientists in a wide range of research fields, including biotechnology, bioengineering, the food packing industry, environmental purification, biomass pre-treatment and conversion, recovery processes, solvent and gas separation, have recently given Deep Eutectic Solvent (DES) supported membranes a lot of attention. In order to obtain the requisite membrane characteristics for gas separation, we suggest using a novel family of solvents called DESs to functionalize DES/TiO₂ nanosheets and partially replace the oxygen functional groups with hydrophilic groups. Ionic liquids have comparable capabilities, but DESs have recently gained popularity as a preferable replacement due to their cheaper cost, toxicity, and considerably simpler production [6]. Low-porosity membranes and DES have been combined, and this has shown to be a desirable property, resulting in the creation of next-generation membranes that can satisfy practical requirements for food packing industry. The gases often used in modified environment packaging are nitrogen, carbon dioxide, and oxygen (N₂, O₂, CO₂). In the field of food packaging, other gases, including Ar and H₂ were being studied. As they are not soluble in polymer crystallites, gas molecules cannot penetrate them, at the end, the amorphous regions are where the gas penetration into semi-crystalline polymers is restricted. Due to a long, winding route between the crystallites and a reduction for polymers that is accessible for gas penetration and crystallite permeability has decreased. The volume fraction of the crystalline phase has inversely correlated with the decrease in permeability.

In this present study, the blending of PET and PEG has been accomplished by a simple phase-inversion technique, by using glassy polymers in 50 wt% ratios. The nanofillers DES/TiO₂ were used with different amounts such as (1 wt% - 15 wt%). A polymer nanocomposite membrane (PNC) of PET/PEG blend composition with 1 wt% of DES/TiO₂ nanofiller for balanced mechanical properties in terms of stiffness and toughness is also significant. The DES/TiO₂ nanofillers can significantly reduce the gas penetration of polymeric membranes, which gives them an additional benefit over conventional carbon reinforcements. However, the drastic change in permeation of gases with the thermal and mechanical stability of both composite membranes has been improved by adding DES/TiO₂ nanoparticles to the polymer matrix. While gas permeability will be minimal perpendicular to the layer orientation, composite stiffness will be most significant in that direction. Gas flows through a nonporous polymer membrane according to this concept by separating from the beginning of the membrane exposed to low pressure, dissolving into the face of the membrane exposed to high gas pressure, and diffusing through the polymer [7]. Gas molecules move through these free

volume elements via Brownian motion (i.e., diffusion), here two significant elements in controlling the diffusion of small gas molecules through polymers are the local segmental motions of polymer chains and polymer stacking. The thermal analysis of PET, PEG, and PET/PEG blend samples are discussed using the DSC and TGA method. The polymeric structure becomes stiff, brittle, and glassy at this glass transition temperature (T_g) and using DSC, identified polymer glass transition temperature (T_g) and by using TGA analyzed weight loss of material. The DSC analysis of PET, PEG and a blend of PET/PEG films made with various weight percent (wt%) ratios of DES-TiO₂ nanofillers is presented in this chapter. Combining polymers alters their thermal diffusivity, capacity, density, thermal conductivity and specific heat in a dramatic way, with that morphology and phase separation directly linked to the characteristics of polymer blends [8]. At present, a group of researchers in polymer science seem to be focusing on better materials for the food packing industry, along with other qualities like good thermal stability and better mechanical properties.

4.2.2 Experimental Set-up

4.2.2.1 Synthesis of Membranes

The pure polymeric membrane of PET, PEG and blend composite membrane of PET/PEG-DES/TiO₂ with different wt% of DES/TiO₂ nanofillers were prepared by the solution casting method. The synthesis of DES by using 1:1 molar ratio of dry ChCl and urea were mixed together and then heated for around 2 hr at 80 °C with constant stirring to produce clear fluid. At 40 °C, this fluid was equilibrated for 24 hr in a vacuum oven. To achieve homogenous dispersion, 10 ml of DES and 1 g of TiO₂ were sonicated for 1 hr. This dispersion was put in a flask with a flat bottom, stirred for two hours at 80 °C, and then transferred. After filtering, the mixture endured numerous washings with distilled water and 50 ml of ethanol each time. This DES modified nanocomposite (DES/TiO₂) was dried for 24 hr at 80 °C in a vacuum oven. In this experiment, both polymer granules were dissolved into Dichloromethane (DCM) solvent and then the solution was stirred for 24 hr on a digital magnetic stirrer with a control rpm of 500. PET has viscosity of 0.785 dL/g and PEG has viscosity of 0.893 dL/g. To get a homogenous blended solution, the solution of PET and PEG was individually stirred for 24 hr and then again, blends of PET and PEG polymers with weight percentage ratios of PET: PEG (50:50 w/w%) was stirred for 24 hr at ambient temperature. DES modified titanium dioxide (TiO₂) was individually stirred for 12 hr in a solvent of Dichloromethane, and then went the of PET/PEG composite with DES/TiO₂ (1 wt%, 3 wt%, 5 wt%, 10 wt%, and 15 wt%)

was sonicated for 1 hr by using probe-sonicator for better agglomeration and then all solution was again stirred for 24 hr at ambient temperature. The solvent was moved to a glass with a flat bottom, and the solvent evaporated overnight. The next day, after being taken out of the petri dish using the solution casting technique, these membranes were further tested for permeability. A thickness gauge with a least count of 0.001 mm was used to measure the thickness of membranes [7]. Various characterization techniques have been discussed in chapter 2.

4.2.3 Results and Discussions

4.2.3.1 Gas-Barrier Properties

Gas permeability of food packaging materials can cause degradation and corrosion. In terms of oxygen permeability, the amount of oxygen introduced into the package is sufficient to enable faster microbial growth and food degradation. The permeability of the carbon dioxide should be strictly regulated for the packing of carbonated beverages and bacterial blooms in the food, causing it to metamorphose [9]. Fresh fruit and vegetable respiration absorbs oxygen and emits carbon dioxide and water, reducing nutrients in storage circulation and resulting in taste changes and weakness. Therefore, the study of packaging material permeability is important for the food business. This characterization looked at three properties: gas permeability, diffusivity, and solubility of materials. The elements that affect permeability were examined along with certain technology that may increase barrier properties. Since hydrogen is much more permeable to polymers than other gases, such as nitrogen, oxygen, and carbon dioxide, membranes were first used to separate hydrogen from mixtures of other gases. Due to its fast ability to do so, membrane-based gas separations were first focused on separating H₂ from CO₂.

The filtering process used in gas purification is another industrial use for hydrogen-based membranes [10]. In terms of separation efficiency, the polymer used to synthesize the membrane is the most important factor, Figure 4.2.1 (I and III) shows the effects of food packing material permeability of pure PET, pure PEG, blend of PET/PEG and polymer composite blends of PET/PEG with (1, 3, 5, 10, 12 and 15 wt%) of DES/TiO₂ with respect to various gases like H₂, O₂, CO₂, N₂, and Ar.

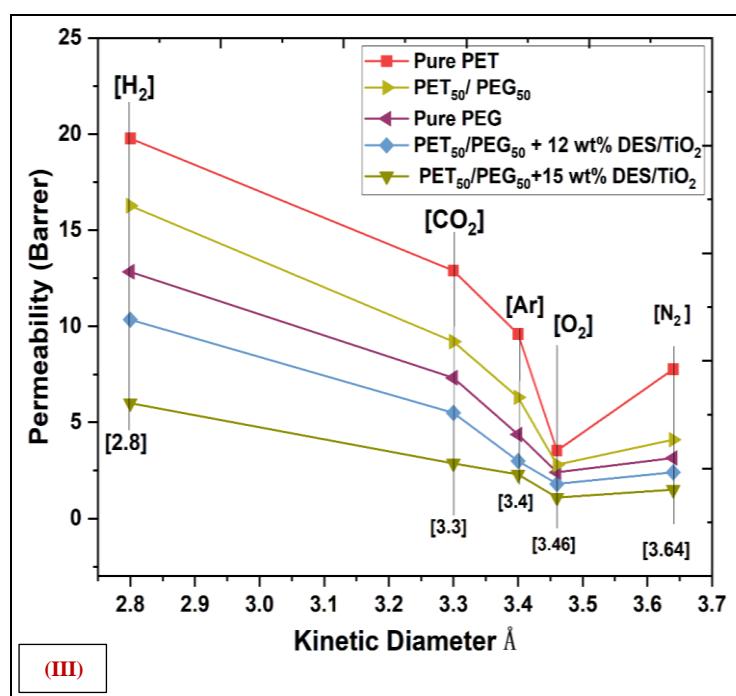
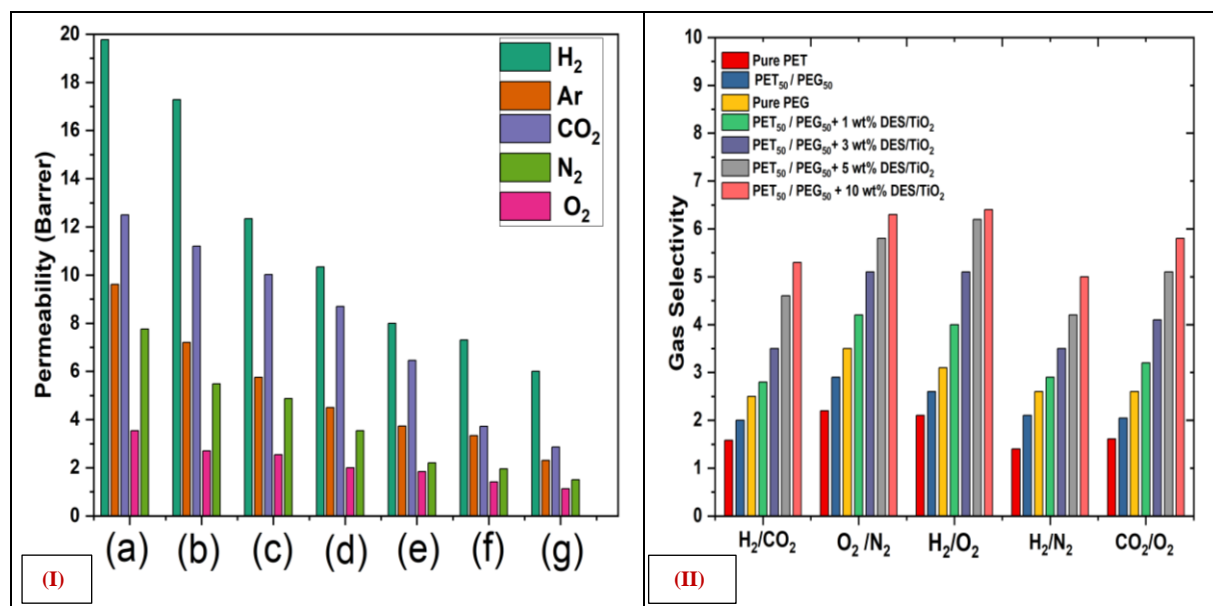


Figure 4.2.1: (I and III) Permeability and (II) Selectivity comparison of pure and blend PET/PEG composite with (1, 3, 5, 10, 12 and 15 wt%) of DES/TiO₂ nanofillers

Figure 4.2.1 shows the gas permeability and selectivity of many commonly used polymer materials. Here, it has been observed that the permeability of pure PET is high as compared to the permeability of pure PEG, still, as we increase the weight percentage of PEG in the pure PET blending ratio, the permeability drastically decreases which is observed in Figure 4.2.1 (I). Membrane thickness plays a significant role in the calculation of gas permeability [11]. When in a blending ratio of PET/PEG as we increase wt% of DES/TiO₂ the permeability of the material has decreased and in the case of PET₅₀/PEG₅₀ membrane

permeability is very low as compared to all other blending ratios of PET: PEG (50:50 w/w %) with respect to all gases. As the blending ratio of the two polymers have altered, the permeability has been found to change dramatically. The permeability decreases by almost half as we DES/TiO₂ from pure PET to a blend of (PET₅₀/PEG₅₀) polymer membranes. In the case of H₂ and CO₂, permeability decreased by 62% and 67% as we went from pure PET to blends of PET₅₀/PEG₅₀. This might be because PET and PEG are miscible polymers and as we increase the wt% of DES/TiO₂ in PET/PEG polymer blend, then DES/TiO₂ decreases porosity and fractional free volume (FFV) between two molecules of polymer membrane to measure gas permeability. The percentages of H₂ and CO₂ permeable fillers in the blend matrix are proportional to the effects of those gases to a smaller extent than their respective blend membrane. Oxygen has less penetrates through membranes, it is possible that causes for the shifts include oxygen molecules being significant and more irregularly shaped compared to H₂ molecules. It has shown that the mixing effect decreases oxygen permeability while decreasing hydrogen permeability also. The permeability decreases with the addition of DES/TiO₂ nanofillers and when increased the concentration of DES/TiO₂. This may be a result of bipolar interactions between O₂ and the chemical composition of the substance. The characteristics parameter of diffusivity and solubility for O₂, which were affected by the interaction between the polymer and the penetrant, also affect O₂ permeability. O₂ is a non-polar molecule, it may dissolve in a matrix of polar functional groups in polymers. The solubility parameter has been affected due to condensation between the carbon dioxide and the polymer blends. In the case of oxygen, adding 10 wt% of DES/TiO₂ to PET/PEG results in a 72% reduction in permeability. This result supports the idea that blends with PEG polymers provide a ‘tortuous channel’ that slows molecular diffusion through the matrix and limits the cross sectional area available for permeation and it is comparable to the permeability reduction found for different gases [9,10].

Figure 4.2.1 (II) shows the selectivity of various gas pairings of H₂/CO₂, H₂/O₂, O₂/N₂, H₂/N₂, CO₂/O₂ for both pure and modified membranes. Due to the mixing of PET/PEG, the permeability for H₂ and CO₂ improves, but the selectivity is little improved. The selectivity for hydrogen over carbon dioxide has improved by 27%; compared to producing a blending membrane, hydrogen separation from the other gases is restricted. Selectivity of hydrogen over oxygen was improved by up to 36%, whereas over nitrogen was reduced by 6% for pure PET to a blend of PET₅₀/PEG₅₀ wt% ratio. The selectivity of oxygen over nitrogen was reduced by 39% and carbon dioxide over oxygen was improved by 25% and decreased permeability of oxygen often results in increased selectivity in membrane materials. In the case of the blend of

PET/PEG same trend is obtained; the selectivity was increased by increasing the wt% of DES/TiO₂ in a blend of PET/PEG for H₂/CO₂, H₂/O₂, and CO₂/O₂ gas pairs and the permeability has decreased at the same time. Comparing the blended membrane structure of PET/PEG to a pure polymer membrane of PET, a significant variation in selectivity has been obtained. Although permeability-selectivity parameters are trade-offs, the nanogap theory may be responsible for DES/TiO₂ selectivity increasing as permeability decreases. According to the theory, the weak adherence to polymer chains causes a free small space or nanolayer to form surrounding them. As a result, the separation factor is supported by the fact that short diffusive modes enhance penetrant penetration and that the nanogap increases as the filler surface becomes compatible with the polymer blend [10,11].

One of the most significant methods to enhance the barrier property is composite multilayer structure packaging. Figure 4.2.1 (III) shows the permeability of different blends of PET/PEG composite with (1, 3, 5, 10, 12 and 15 wt%) of DES/TiO₂ membranes. We can quickly notice from Figure 4.2.1 (III) that the barrier property increased after composite with DES/TiO₂ nanofillers. The outside material must have great strength, nice gloss, heat resistance and thermal stability. Moreover, it requires high barrier qualities and double-sided conformance for the intermediate layer. It has been shown that the addition of DES/TiO₂ nanofiller particles causes a significant shift in permeability. PET/PEG-DES/TiO₂ (1, 3, 5, 10, 12 and 15 wt%), reduces the membrane permeability compared to pure PET membrane. PET/PEG-DES/TiO₂ (1, 3, 5, 10, 12 and 15 wt%) reduces the permeability compared to pure PET and blend composite of PET/PEG-DES/TiO₂. Additionally, blend of PET₅₀/PEG₅₀ composite with (1, 3, 5, 10, 12 and 15 wt%) of DES/TiO₂, it was shown that a more significant value reduced the permeability compared to that of PET, PEG, composite of (1, 3, 5, 10, 12 and 15 wt%) of DES/TiO₂ [5,7]. By introducing the blending effect in PET with PEG in (50:50) wt% ratios composite with (1, 3, 5, 10, 12 and 15 wt%) of DES/TiO₂ nanofillers, the permeability has reduced by 70% in the case of hydrogen gas and in comparison to their respective blend membrane, it decreases O₂ permeation. The differences between oxygen molecules and those of H₂ and CO₂ may explain the changes. For blended composite membranes, further modification results in a change in hydrogen permeability value. Rather than an improvement in penetration, the fillers actually work against it and decrease the permeability of the material [6,7]. The mechanism explains PNC membrane changes for H₂ penetration (nanogaps hypothesis) explained above and strong penetration of the filler surface into the polymer volume causes a reduction in permeability in the Maxwell model [15]. In

contrast, the inclusion of filler enhances the porosity of the blended composite membrane in this case. Because the blending process already causes polymer chain interaction and alters the polymer structure, inserting DES/TiO₂ fillers blocks the available free volume or fractional free volume. The efficiency of gas molecules to diffuse through the membrane matrix is restricted by this small barrier. As a result, the blended membrane of PET₅₀/PEG₅₀-DES/TiO₂ is even well suited for food packing material compared to pure PET, PEG and blends of PET/PEG, we also can consider the blended composite of PET₅₀/PEG₅₀ with DES/TiO₂ because they are cost effective membrane material.

4.2.3.2 Diffusion and Solubility Coefficients

The key components of membrane penetration are diffusivity (D) and solubility (S). Diffusivity measures how easily molecules can travel over the pores of membrane, whereas solubility measures how many gas molecules can be dissolved in a substance. Diffusivity has also been affected by the size and shape of the membrane pores. The composition gradient is the driving factor in molecular diffusion, smaller solute molecules can diffuse more readily than larger molecules. The diffusion rate of solute molecules is inversely proportional to their size. Figure 4.2.2 (III and IV) shows the diffusion coefficients and, solubility coefficients and diffusivity-selectivity, solubility-selectivity of pure and blend of PEG/PET polymer membranes composite with different wt% of DES/TiO₂. It has been observed that the diffusivity increases with decrease in amount of DES/TiO₂ in PET/PEG blend membrane and with that, solubility decreases in the same scenario. The permeability of PET was 19.6 Barrer compared to other membranes as we increased the amount of DES/TiO₂ in PET/PEG blend then permeability decreased with that solubility increased and diffusivity decreased. As a result, larger molecules diffuse more slowly [12]. Based on these results, permeability is shown to be directly related to material solubility and inversely proportional to material diffusivity. The inclusion of impermeable filler particles makes the diffusive channel more compressible, the diffusion coefficients in the mixed matrix are estimated using the free volume theory applied to the polymer phase. The fillers existence impacts the mixed matrix diffusion coefficient in two different ways: (i) Because DES/TiO₂ particles block the gas molecules flow through in the blends membrane and are impermeable, they increase diffusivity by making the diffusive path more sinuous (ii) The polymeric composite matrix has a decreased fractional free volume due to the nanofiller, which increases diffusivity. For all the gases, the values of diffusivity consistently rise with the Van der Waals volume of the penetrants, and an explanation provided for this in Figure 4.2.2.

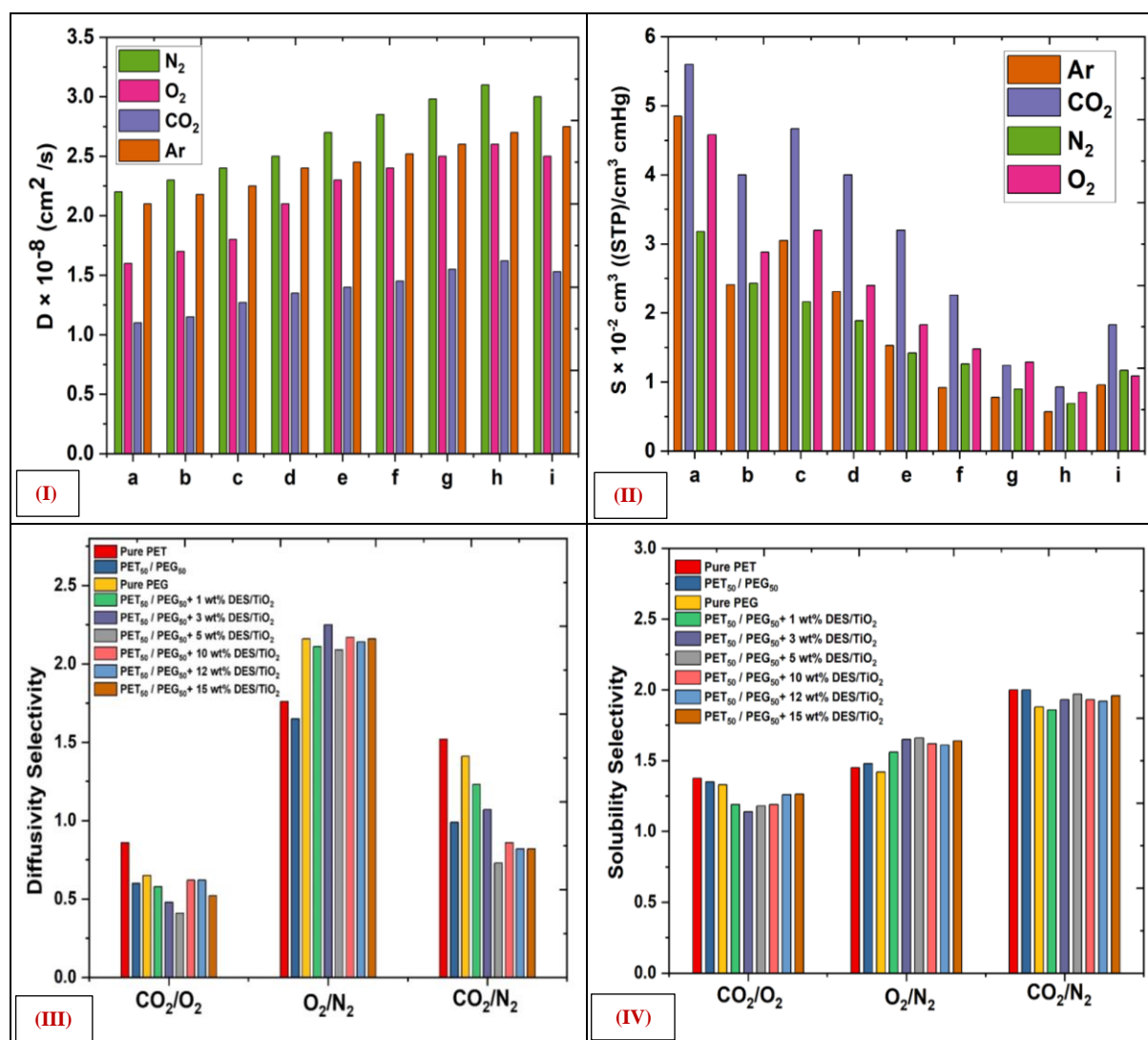


Figure 4.2.2: (I and II) Describes the Diffusion coefficients and Solubility coefficients value of pure and blend of PEG/PET polymer membranes composite with 1 wt% of DES/TiO₂, here (a) Pure PET (b) PET₅₀ / PEG₅₀, (c) Pure PEG, (d) PET₅₀/PEG₅₀ + 1 wt% of DES/TiO₂, (e) PET₅₀/PEG₅₀ + 3 wt% of DES/TiO₂, (f) PET₅₀/PEG₅₀ + 5 wt% of DES/TiO₂, (g) PET₅₀/PEG₅₀ + 10 wt% of DES/TiO₂, (h) PET₅₀/PEG₅₀ + 12 wt% of DES/TiO₂, (i) PET₅₀/PEG₅₀ + 15 wt% of DES/TiO₂, **(III and IV)** Represent Diffusivity-Selectivity, Solubility-Selectivity of pure and blend of PEG/PET polymer membranes composite with (1, 3, 5, 10, 12 and 15 wt%) of DES/TiO₂ nanofillers

It is difficult to develop accurate expectations for permeability, solubility, and diffusivity just based on the behaviour of the unloaded polymer matrix [11,12]. Differences in the molecular interactions between the permeating species and the membrane contribute to differences in solubility. Greater selectivity may result from making use of chemically specialized energetic interactions like hydrogen bonding; simple Van der Waals dispersion forces, which are frequently greater for bigger molecules, may nevertheless lead to substantial selectivity.

When DES/TiO₂ nanoparticles are added to high-free-volume glassy polymers, mixed matrix membranes (MMM) are created that have solubility and transport behaviour for a wide range of compounds. At a particular temperature, gases such as N₂, O₂, CO₂, and water vapour have various capacities for condensation, which is related to their differences in solubility. Therefore, it is assumed that the physical constants of the various gases, particularly temperature and condensation pressure, can affect how permeable they are. Diffusivity selectivity, a measurement of ability of polymer membranes ability to distinguish between molecules of various sizes and shapes, is highly influenced by the mobility of the polymer segments and intersegmental packing [13]. The method also allows the calculation of the ideal contributions of solubility-selectivity and diffusivity-selectivity contributions, a sufficient description of the observed behaviours for the ideal selectivity. Based on the values of the diffusion coefficient, which typically increases with increasing penetrant size, it has been projected that the diffusivity contribution would dominate the selectivity behaviour in these studies. Solubility-based gas separations are possible using both inorganic and polymeric membranes, both have their advantages and disadvantages and at the moment scientists are putting more effort into building membranes that can both process a significant amount of fluid and be very selective [7,8]. By comparing the permeability of Amul Milk bag, Amul Butter Milk bag, PET₅₀/PEG₅₀, PET₅₀/PEG₅₀ + 5 wt% of DES/TiO₂, and PET₅₀/PEG₅₀ + 10 wt% of DES/TiO₂ membrane.

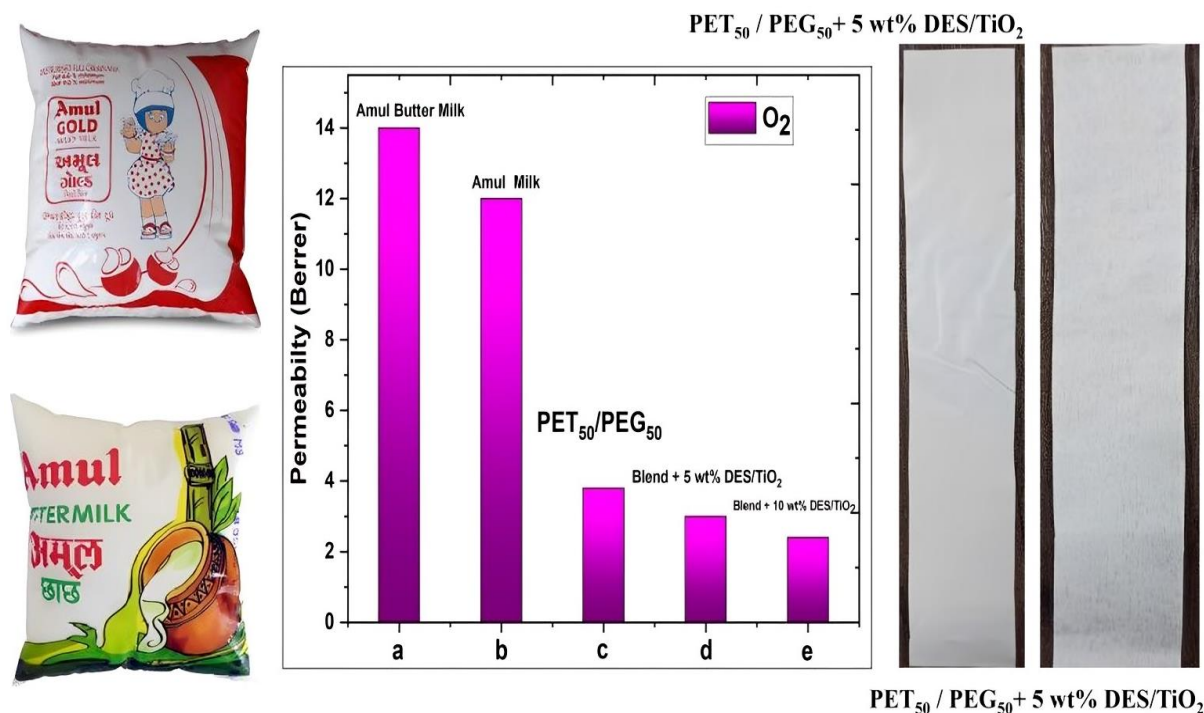


Figure 4.2.3: Permeability comparison of Amul Milk, Amul Butter Milk, PET₅₀/PEG₅₀, PET₅₀/PEG₅₀ + 5 wt% of DES/TiO₂, PET₅₀/PEG₅₀ + 10 wt% of DES/TiO₂

Figure 4.2.3 observed that the permeability of O₂ gas is decrease for PET₅₀/PEG₅₀ blend and blend composite with different wt% of DES/TiO₂ nanofillers. Experiment with Amul milk and Amul butter milk packing material was performed, It was observed that the value permeability of O₂ for Amul milk and Amul butter milk packing material is 14 Barrer and 12 Barrer, respectively. The permeability value is decreasing in case of Barrer PET₅₀/PEG₅₀, blend composite with 5 wt% of DES/TiO₂ and 5 wt% of DES/TiO₂ which is around 3.8 Barrer, 3 Barrer, 2.8 Barrer, for O₂. This phenomena happened because DES/TiO₂ fillers decreased the fractional free volume and void space between PET/PEG blend and DES/TiO₂ act as a barrier parameter for oxygen gas [14]. It shows that the permeability of oxygen has been reduced in case of a blend and blend composite of PET/PEG-DES/TiO₂ material, it will increase the freshness and reduce the deterioration rate of food. Therefore, the blend composite of PET/PEG-DES/TiO₂ material is more effective for packing material than exist up packing material by industry used.

4.2.3.3 Porosity Analysis

It observed that increasing membrane thickness increases microcapsule strength while decreasing membrane permeability because it provides stability to the mass transfer of chemicals across the membrane surface.

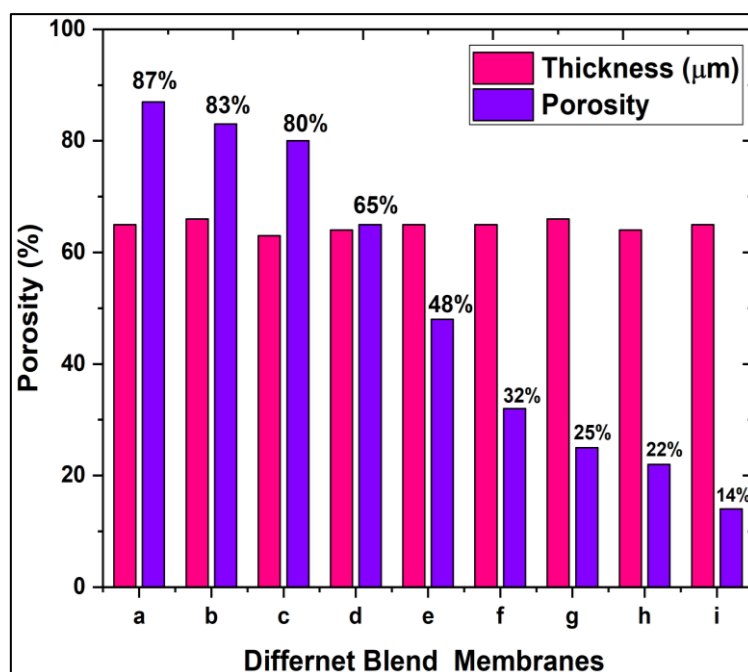


Figure 4.2.4: Thickness and Porosity comparison of pure and blend composite membrane, (a) Pure PET (b) PET₅₀/PEG₅₀, (c) Pure PEG, (d) PET₅₀/PEG₅₀ + 1 wt% of DES/TiO₂, (e) PET₅₀/PEG₅₀ + 3 wt% of DES/TiO₂, (f) PET₅₀/PEG₅₀ + 5 wt% of DES/TiO₂, (g) PET₅₀/PEG₅₀ + 10 wt% of DES/TiO₂, (h) PET₅₀/PEG₅₀ + 12 wt% of DES/TiO₂, (i) PET₅₀/PEG₅₀ + 15 wt% of DES/TiO₂

In all membrane separation procedures, the thickness of the membrane plays a significant role in determining how well it performs. The rate of diffusion increases as the membrane thickness decreases. While under normal conditions, the diffusion barrier is exceedingly porous, some situations cause the barrier to expand and hinder diffusion [15]. The net diffusion rate of a gas over a gas membrane has been inversely correlated with the thickness of the membrane, proportional to the area of the membrane and proportional to the change in partial pressure. The thickness and porosity of the membranes for the PET/PEG blend and the PET/PEG blend with (1, 3, 5, 10, 12 and 15 wt%) of DES/TiO₂ nanofillers membranes are shown in Figure 4.2.4. Porosity of PET and PET/PEG is very high, but as increase the wt% of DES/TiO₂ nanofillers in a blend of PET/PEG, the porosity decreases and that results are expecting this blending material is very applicable for food packaging, particularly the blend of PET₅₀/PEG₅₀ - 15wt% of DES/TiO₂. As porosity decreases, permeability decreases, and porosity is a measure void spaces of a materials and permeability is a measure ability of a materials to transfer gas molecules or fluids [11,12]. Porosity and permeability are properties common to all materials and permeability is a measure of how easily a fluid flows through a porous material and material may be extraordinarily porous, yet it has no permeability if the pores are not interconnected. Similarly, a material may have a few continuous pores that permit fluid movement, yet when porosity is calculated, the material does not seem to be extremely porous. Membrane porosity, which is related to the void volume percentage of membranes, calculated as the volume of the holes divided by the total volume of the membrane. Although not all voids are open at both ends, the effective porosity of the membrane has been defined as the ratio of the related pore volume to the overall void volume. The stiffness of the porous network has been regulated by the solid phase, which is the pores wall. As the number of holes along the width was decreased by increasing the wt% ratio of (1, 3, 5, 10, 12 and 15 wt%) DES/TiO₂ nanofillers, the porous structure with smaller pores exhibited a better capacity to tolerate flow stress [12,13]. Therefore, the samples with bigger pore sizes deformed more than those with smaller pore sizes, suggesting more flexible behaviour.

4.2.3.4 Differential Scanning Calorimetry (DSC)

PET and PEG blends were developed by modifying the weight percentage ratio of PET and PEG polymers. Blends were heated at 50 °C up to 120 °C temperature with a heating rate of 5 °C/min. According to these observations, the blends of PET: PEG (50:50) polymers are miscible while in the blending process. The glass transition temperature (T_g) of pure PEG, pure PET and all blend composite of PET/PEG-DES/TiO₂ with different wt% shown in Figure 4.2.5.

Furthermore, a DSC experiment is conducted to examine the impact of T_g value on blends of PET/PEG blends with different concentrations of PET and PEG. From these curves, it observed that when we increased the wt% of DES/TiO₂ nanofillers in PET/PEG blends then the glass transition temperature also increases with wt% of DES/TiO₂. After adding PEG and DES/TiO₂ it increases the thermal stability of PET/PEG blend composites membrane.

Figure 4.2.5 it is shows that the glass transition values of pure PEG is 79.25 °C, for PET₅₀/PEG₅₀ the T_g value is 90.60 °C, for Pure PET the T_g value is 91.27 °C, for PET₅₀/PEG₅₀ + 1 wt% of DES/TiO₂ the T_g value is 91.73 °C, for PET₅₀/PEG₅₀ + 5 wt% of DES/TiO₂ the T_g value is 94.90 °C, for PET₅₀/PEG₅₀ + 10 wt% of DES/TiO₂ the T_g value is 95.26 °C, for PET₅₀/PEG₅₀ + 12 wt% of DES/TiO₂ the T_g value is 97.06 °C. DSC curves confirm the behaviour of heterogeneous polymeric systems. It is clear from Figure 4.2.5 that the thermal stability increases for PET/PEG blend with increasing the wt% of DES/TiO₂ nanofillers in the blend and thermal stability of the blend of PET₅₀/PEG₅₀ is very good as compared to blend of PET/PEG polymer.

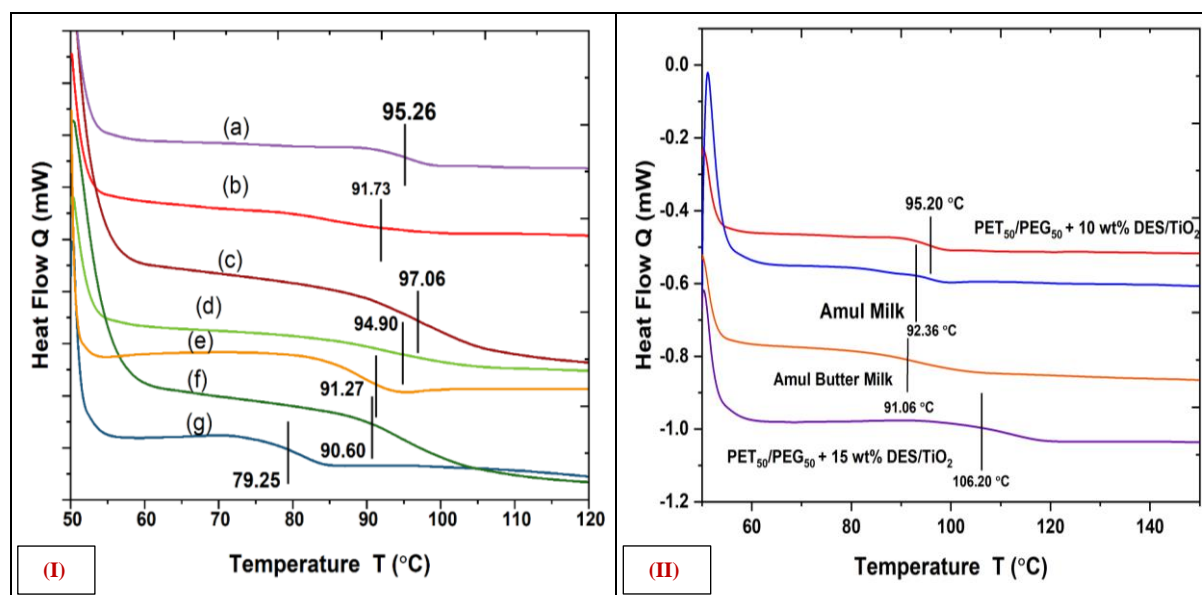


Figure 4.2.5: DSC thermogram of (I) Pure PET, Pure PEG and PET/PEG - DES/TiO₂ polymer blend composite here (a) PET₅₀/PEG₅₀ +10 wt% of DES/TiO₂, (b) PET₅₀/PEG₅₀ + 1 wt% of DES/TiO₂, (c) PET₅₀/PEG₅₀ + 12 wt% of DES/TiO₂, (d) PET₅₀/PEG₅₀ + 5 wt% of DES/TiO₂, (e) Pure PET, (f) PET₅₀/PEG₅₀, (g) Pure PEG and (II) comparison of Amul Milk, Amul Butter Milk, PET₅₀/PEG₅₀ + 10 wt% of DES/TiO₂, PET₅₀/PEG₅₀ + 15 wt% of DES/TiO₂

The T_g value of the blend polymer of PET/PEG is shown in Figure 4.2.5 (I); from these values of T_g , it is said that the T_g changed as we changed different wt% ratios of DES/TiO₂ nanofillers in miscible polymer blends, it happened because of miscible bonding between PET

and PEG polymer and also because of the amorphous nature of PEG and semi-crystalline nature of PET polymer. As a result of the presence of inorganic nanocomponents, the polymer matrix becomes stuck, increasing the glass transition temperature (T_g). Although they could make the material harder to process, interaction regions have been suggested in which the polymer has adsorbed, increasing the softening temperature by a few degrees (18 °C) and extending the polymers useful lifetime. Figure 4.2.5 (II) shows the comparison of glass transition temperature of Amul Milk bag, Amul Butter Milk bag, PET₅₀/PEG₅₀ + 10 wt% of DES/TiO₂, and PET₅₀/PEG₅₀ + 15 wt% of DES/TiO₂.

4.2.3.5 Thermogravimetric Analyzer (TGA)

Table 4.2.1 represents the T_g values of blend composite membrane and some industrial packing materials, it shows composite with 15 wt% of DES/TiO₂ gives 106.20 °C, T_g value which shows good thermal stability of material as compared to other industrial packing materials. DES/TiO₂ particles have good thermal characteristics and when we composite DES/TiO₂ particles with PET/PEG blend the thermal stability of overall material is increasing.

Table 4.2.1: Glass transition temperature (T_g) value of different polymer blend composite material and some industrial packing materials

Material	Glass Transition Temperature (T_g) (°C)	Material	Glass Transition Temperature (T_g) (°C)
PET ₅₀ /PEG ₅₀ +10 wt% of DES/TiO ₂	95.26	PET ₅₀ /PEG ₅₀ +15 wt% of DES/TiO ₂	106.20
PET ₅₀ /PEG ₅₀ + 1 wt% of DES/TiO ₂	91.73	Amul Milk	92.26
PET ₅₀ /PEG ₅₀ + 12 wt% of DES/TiO ₂	97.06	Amul Butter Milk	91.06
PET ₅₀ /PEG ₅₀ + 5 wt% of DES/TiO ₂	94.90	Pure PET	91.27
PET ₅₀ /PEG ₅₀	90.60	Pure PEG	79.25

From this DSC thermogram it observed that the value glass transition temperature of blend PET/PEG composite with 10 wt% and 15 wt% of DES/TiO₂ higher than Amul Milk and Amul Butter Milk packing material, that means PET/PEG composite with DES/TiO₂ has increased the thermal stability of material. It has observed that the value of T_g of Amul Milk bag and Amul Butter Milk bag is 92.36 °C and 91.06 °C, for PET/PEG blend composite with 10 wt% and 15 wt% of DES/TiO₂ the value is 95.20 °C and 106.20 °C.

Moreover, increase the wt% of DES/TiO₂ the material has become more thermally stable. The plasticizer effect of the small inorganic nanocomposite molecules in the polymeric blend, which facilitates the intramolecular mobility of the polymers lateral chains, may be the reason for the T_g increased when PET/PEG polymer composite with DES/TiO₂ nanofillers. The tensile stress of the polymer may also influence the change in T_g [15]. This phenomenon has happened because of the good thermal stability of DES/TiO₂ particles. The thermal stabilities of PET/PEG blend composites with a ratio of DES/TiO₂ (1 wt% and 3 wt%) were evaluated using TGA. Figure 4.2.6 (I) shows the samples TGA and thermograms. This graph indicates that all samples showed a similar decomposition behaviour. Table 4.2.2 provides a summary of the decomposition temperatures for various percent weight losses.

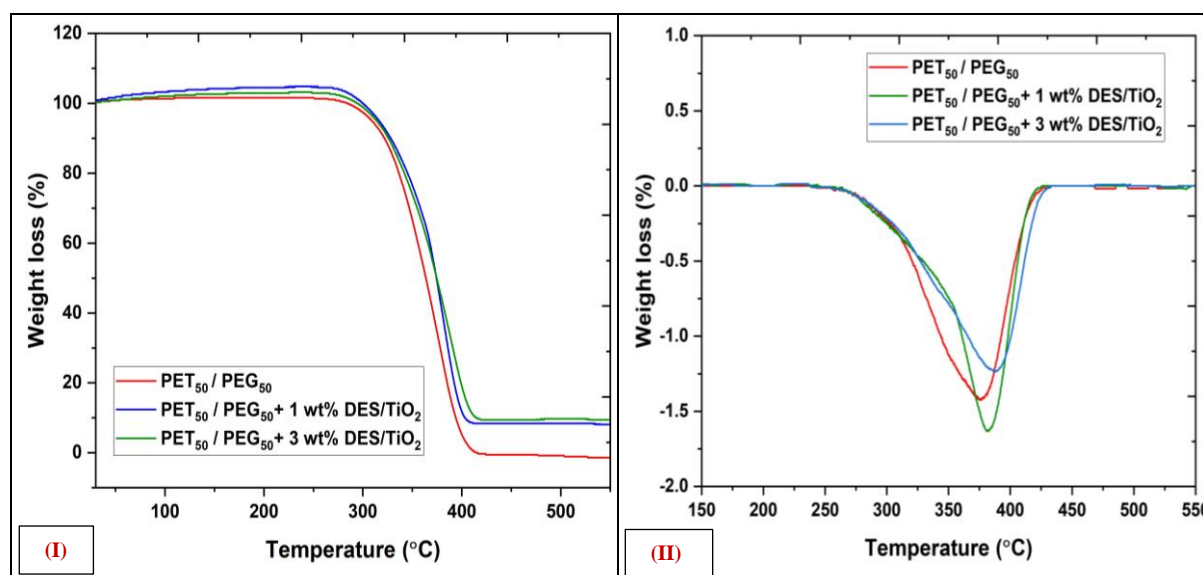


Figure 4.2.6: (I) TGA thermogram and (II) DTG thermogram of PET/PEG polymer blends

The char yield in TGA is a significant parameter that provides valuable information about the thermal decomposition behaviour of a material. TGA curves often exhibit multiple stages of decomposition, each corresponding to the breakdown of specific components in the material. The char yield at each stage can help identify the residues formed during different

decomposition steps. For materials used in applications where fire resistance is important, char yield is a key parameter. Materials that leave behind a higher char residue after exposure to high temperatures are often more fire-resistant, as the char layer can act as a protective barrier.

The temperature at which weight losses of 5%, 50%, and 95% of the total weight as well as the char yield (wt%) at 500 °C were analyzed in order to determine the impact of addition of DES/TiO₂ on the thermal stability of PET/PEG blend composites. The temperature at which 50% of the material had begun to degrade (T₅₀) and the initial decomposition temperature (T₀) were determined using the TGA curves. Table 4.2.2 provides the temperature for the first, half, and final stages of decomposition. In the case of PET/PEG-DES/TiO₂ the blend composites ratio, starting mechanism, and crosslinking amount affect the T₀ and T₅₀ values. The temperature of decomposition increases as DES/TiO₂ content increases. It is noticeable that the addition of DES/TiO₂ improves thermal stability even more since it decreases the decomposition temperature and increases the emission of char. For weight losses of 5%, 50%, 95% and T_{max} respectively, the degradation temperatures were determined to be in the range of 250 °C to 260 °C, 290 °C to 300 °C, and 410 °C to 420 °C, respectively. When DES/TiO₂ content was increased from 1 wt% to 3 wt%. In general, PEG improves the blends thermal stability and decreases the rate of weight loss, producing a high char yield at higher temperatures [14,15]. The physical, mechanical, and relative thermal properties of the PEG-filled PET/PEG.

Table 4.2.2: TGA data of the decomposition temperatures of PET/PEG blends at different percent weight loss

Membrane Samples	Temperatures at Characteristic Weight Loss, °C				T _g (°C)	Char yield (wt%) at 550 °C
	T _{5%}	T _{50%}	T _{95%}	T _{max} (°C)		
PET ₅₀ /PEG ₅₀	253	295	410	375	91.27	1.48
PET ₅₀ /PEG ₅₀ + 1 wt% of DES/TiO ₂	254	297	414	380	95.26	8.26
PET ₅₀ /PEG ₅₀ + 3 wt% of DES/TiO ₂	255	299	421	390	94.90	9.69

At 500 °C, it was found that the weight loss for the PET₅₀/PEG₅₀ sample was 98%, the PET₅₀/PEG₅₀+1 wt% of DES/TiO₂ sample weight loss was 96%, and for PET₅₀/PEG₅₀+3 wt% of DES/TiO₂ sample it was 94%. This shows that the thermal stability improves as DES/TiO₂ content increases. It is clear that thermal stability increases as crosslinking strength of DES/TiO₂ increases [16]. Due to this trend, it may be reduced that the initial breakdown process for PET starts at a somewhat lower temperature than that of PEG. The weight loss of the PET/PEG blend composite is decreased by increasing wt% of DES/TiO₂ in PET/PEG. Considering, the addition of DES/TiO₂ is more resistant to thermal degradation than pure polymers and blend of polymer, between 320 °C and 420 °C, the weight loss is significant (approximately 90%), as the main chains weakest areas, the ester group C-O and the unsaturated chain C-H are broken [15,16].

Three peaks shown in the DTG curve, corresponding to the degradation of blends composites of PET/PEG-DES/TiO₂ in Figure 4.2.6 (II). Additionally, samples with greater DES/TiO₂ crosslinking, a slight peak has been seen for all samples at around 370 °C. It is clear that from Table 4.2.2, in the majority of cases, the DES/TiO₂ content and crosslinking increase thermal stability. The degradation temperature of the blended PET₅₀/PEG₅₀ has also been found to be higher than that of the pure PET components and other researchers have previously reported that combining two polymers enhances thermal stability [14,15]. The samples with higher weight percentages of DES/TiO₂ nanofiller had excellent thermal stability, as measured by the slope of the main area, than the pure PET sample, which was linked to their lower thermal conductivity.

Between 295 °C to 410 °C, PET₅₀/PEG₅₀ lost almost 98% of its entire mass, with maximum loss at a temperature of 375 °C and after 550 °C, there was no degeneration, PET₅₀/PEG₅₀+ 1 wt% of DES/TiO₂ lost almost 96% of its entire mass between 254 °C to 414 °C, and PET₅₀/PEG₅₀+ 3 wt% of DES/TiO₂ lost 94% of its entire mass between 255 °C to 421 °C. The glass transition temperature that resulting the greatest amount of thermal decomposition is determined using the aforementioned thermal decomposition data. The release of volatile compounds after 370 °C was what caused the sudden weight loss in all blends and the results obtained using the DTG curve also confirmed.

The onset decomposition temperature values taken from the graph are used to assess and compare the thermal stability of the membranes [17]. It is confirmed from study that the addition of DES/TiO₂ and PEG improves the blend thermal stability. The above might cause the second stage of PET/PEG blend decomposition. The ester groups in PET initially broke

down at low temperatures to create carbon-containing compounds, and then crosslinking carbonization took place between these blend and DES/TiO₂ nanofillers. The resulting hydrocarbon char residue served as a barrier against heat and oxygen diffusion on the polymer surface and it increased the second decomposition temperature to a value that was substantially higher than 550 °C, preventing the PET/PEG blend from decomposing any further.

4.2.3.6 Fourier Transform Infrared (FT-IR) Spectroscopy

The subject of polymer miscibility determination using FT-IR spectroscopy is changing rapidly and has given scientists a wealth of knowledge on molecular vibrations throughout the years. The type of bonds determines where these peaks occur [18]. The FT-IR spectra of pure PEG, pure PET polymer, blends of PET/PEG and PET/PEG-DES/TiO₂ blend composites were analyzed in transmission mode for frequency ranges between 400 cm⁻¹ and 4000 cm⁻¹, which is shown in Figure 4.2.7. The PET/PEG-DES/TiO₂ membranes has six functional groups, as can be shown in Figure 4.2.7.

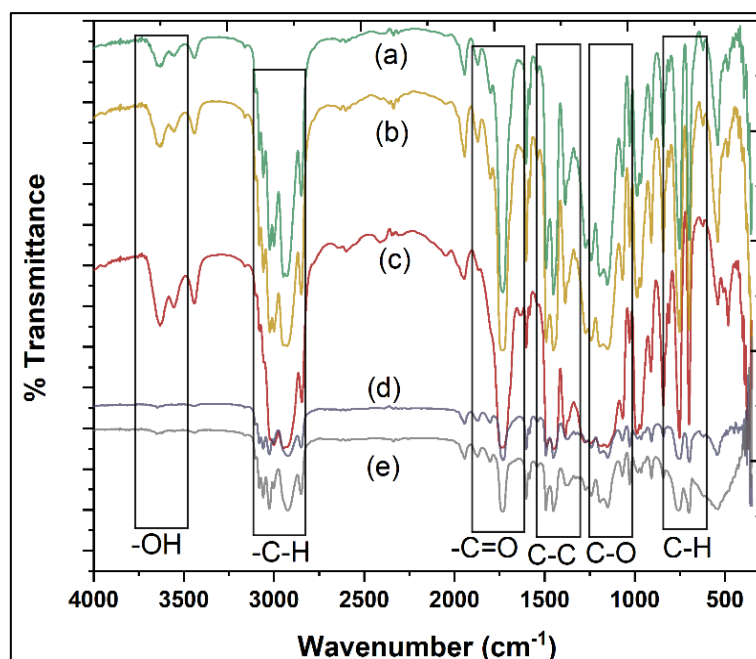


Figure 4.2.7: FT-IR Spectra of pure and blended PET/PEG composition with DES/TiO₂ polymer membranes. Here, the peak represented (a) PET₅₀/PEG₅₀ + 5 wt% of DES/TiO₂, (b) PET₅₀/PEG₅₀ + 10 wt% of DES/TiO₂, (c) PET₅₀/PEG₅₀, (d) Pure PET, (e) Pure PEG

These groups consist of one ethyl group, two ester groups, methylene group and an aromatic ring. The bonds between these functional groups range from C-C to C-H to C-O to -C=O and a -OH. The finger print area, located on the right side of Figure 4.2.7 between 1500

cm⁻¹ and 500 cm⁻¹, typically consists of a very long chain of absorptions. Figure 4.2.7 shows that PET and blends of PET/PEG polymer showed stretching of the C=C bond (benzene ring) has been associated with three different absorption peaks at 1440 cm⁻¹, 1454 cm⁻¹, and 1462 cm⁻¹, whereas stretching of the C-O bond has been associated with peaks at 1150 cm⁻¹ and 1136 cm⁻¹ (formation of ester group). At the C-H aromatic stretching vibration at 2913 cm⁻¹ and 2948 cm⁻¹, the C-H stretching vibration at 695 cm⁻¹, and the phenyl ring stretching vibration at 1720 cm⁻¹, 1435 cm⁻¹, 1160 cm⁻¹, 860 cm⁻¹, and 565 cm⁻¹, the typical absorption bands for polyethylene glycol were clearly visible.

It can be shown that several bands, such as those shown in Figure 4.2.7, 713 cm⁻¹ to 2932 cm⁻¹ belong to C-H deformation because this polymer contains a benzene ring, the band 723 cm⁻¹ was clearly visible in the spectra. Table 4.2.3 area value between 1130 cm⁻¹ and 1146 cm⁻¹ has some vibration, which might be a C-O stretch. Peaks at 1750 cm⁻¹, 1740 cm⁻¹ and 1715 cm⁻¹ were the locations where the C=O bonds and some peaks at 1454 cm⁻¹ and 1430 cm⁻¹ of the C-C stretching and the aliphatic-aromatic C-H stretching 2932 cm⁻¹ and at 2903 cm⁻¹, 2940 cm⁻¹, and 2945 cm⁻¹, C-H stretch aromatic is clearly present, while the hydroxyl group is present at 3630 cm⁻¹ and 3620 cm⁻¹.

The ester groups C-O bond absorbs in the finger print area as well and for the C-O stretching bond, there are two bands at ester groups C-O bond absorbs in the finger print area as well. For the C-O stretching bond, there are two bands located at 1110 cm⁻¹ and 1238 cm⁻¹. The C-H bond for the ethyl group might vibrate in one of two ways: (I) at 2970 cm⁻¹, the medium C-H stretching bond and (II) at 731 cm⁻¹ has the strong C-H bending bond. The C-H stretching band of the aromatic ring is at 2855 cm⁻¹. Alkyl group C-C bond stretching vibration is also associated with the band at 1445 cm⁻¹, and the C-O carbonyl group stretching vibration is associated with the band at 1136 cm⁻¹.

The stretching vibration of the C=O bond in the ester group is responsible for producing the strong band at 1725 cm⁻¹, and absorption bands corresponding to C=O bond stretching are often rather strong because a significant shift in the dipole occurs in that mode [15,16]. C=O is formed when PEG polymer combines with PET polymer. This causes a decrease in transmitted IR intensity as PEG increases because the concentration of -C=O in PET membrane increases as PEG increases (Figure 4.2.7).

Table 4.2.3: FT-IR spectra functional group analysis of pure PEG, pure PET, blends PET/PEG, PET/PEG-DES/TiO₂ blend composite membranes

Membrane Materials	-OH stretching (cm ⁻¹)	-C-H stretching (cm ⁻¹)	-C=O stretching (cm ⁻¹)	C-C stretching (cm ⁻¹)	C-O Bending (cm ⁻¹)	C-H Bending (cm ⁻¹)
PET ₅₀ /PEG ₅₀ + 5 wt% of DES/TiO ₂	3635	2948	1734	1449	1146	753
PET ₅₀ /PEG ₅₀ + 10 wt% of DES/TiO ₂	3640	2937	1734	1457	1141	747
PET ₅₀ /PEG ₅₀	3635	2936	1728	1446	1150	767
Pure PET	3644	2937	1724	1445	1146	753
Pure PEG	3645	2933	1730	1440	1150	754

According to Figure 4.2.7, hydrogen absorption and free carbon atoms may both contribute to the decrease in C-H transmission band intensities, which may increase the concentration of C-H bonds and hence, the transmission of C=O band intensity increasing. After blending with PEG polymer, PET/PEG may oxidize the surface and increase wettability due to -OH released from the band. Furthermore, the polarity may be improved by the release of the free radical -C-H. The -OH group is located at 3634 cm⁻¹, and as shown in Table 4.2.3, the transmission intensities of the PEG polymer increase with the PET blending [19]. Because of this, the blending of PEG and PET membrane causes a change in the surface chemistry, which in turns increases its polarity and wettability. The O-H and C-H bands in the PET/PEG blends FT-IR spectra are less intense than they are in pure PET because the PEG polymer helps to keep the PET monomers together, stretching the polymer chains. These results clearly show the successful formation of the blend of PET/PEG and PET/PEG-DES/TiO₂ composites successfully.

4.2.3.7 Contact Angle Analysis

An experimental method for determining whether a surface is hydrophilic or hydrophobic is measured through the contact angle analysis (Figure 4.2.8). If the angle of contact (θ) is between 0° and 90°, the material is hydrophilic, and if it is between 90° and 180°, it is hydrophobic and determines if the analyzed experimental alloys are hydrophilic or hydrophobic using the sessile drop method.

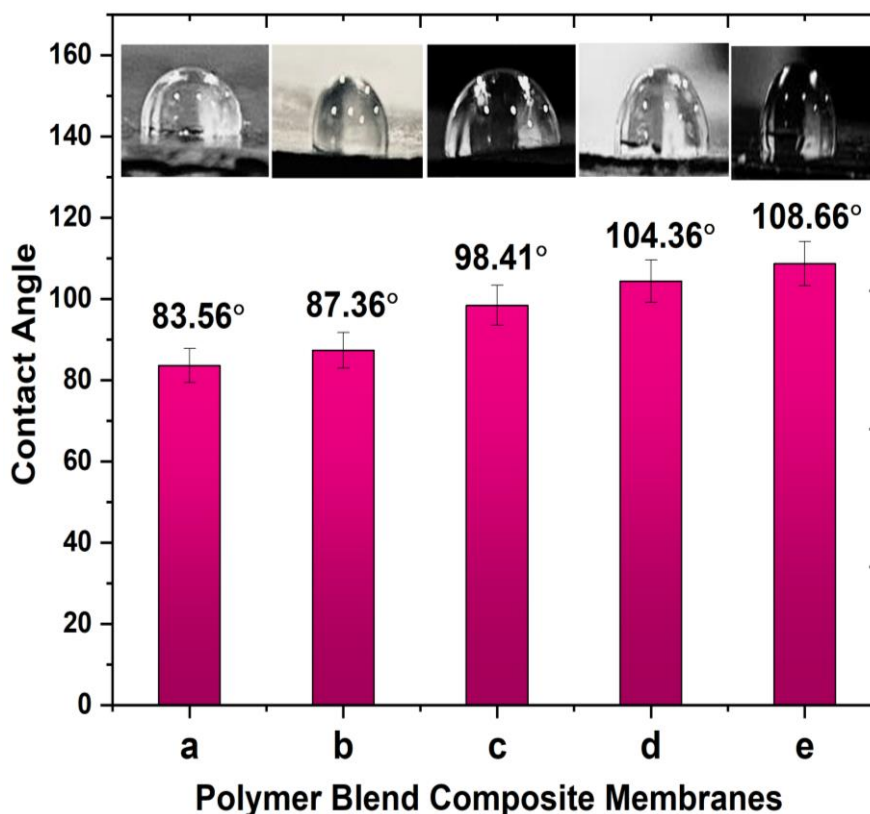


Figure 4.2.8: Water contact angles measurement for pure PET, pure PEG and blends of PET/PEG membranes, here (a) PET₅₀ / PEG₅₀, (b) PET₅₀/PEG₅₀ + 1 wt% of DES/TiO₂, (c) PET₅₀/PEG₅₀ + 5 wt% of DES/TiO₂, (d) PET₅₀/PEG₅₀ + 10 wt% of DES/TiO₂, (e) PET₅₀/PEG₅₀ + 15 wt% of DES/TiO₂

By depositing a drop of water with a micro surge and a drop volume of 4 μ l, the angle of contact is measured. Drop lighting was produced from behind and captured with a digital camera from the opposing side then the ImageJ software does further analysis of the captured picture [19]. As shown in Figure 4.2.8, contact angles were determined, along with the calculation of surface tensions and interfacial tensions, to further analyze pure PET, PEG and miscibility of PET/PEG blend with different wt% ratios of DES/TiO₂. Interfacial tension, which is different and dependent on the contributing phases, results from the interaction of molecules along an interface created when two different phases come into contact [20]. When PET was placed in water, it was found that the contact angle was the smallest. Next, it has observed that PET had a contact angle in the low 90° range for both polar and nonpolar liquids, showing somewhat lower affinity than that of PEG, while PEG had an organophilic nature and showed a hydrophobic characteristic with respect to the water droplet contact angle. If the contact angle is greater than 90°, wetting the surface is not allowed; the liquid would instead stay as a bead on the surface. A super-hydrophobic surface with a contact angle of 150° exhibits the lotus effect, in which the droplet quickly rolls down without making contact with the surface, but a

contact angle of less than 90° shows that soaking the surface is preferable, and the liquid spreads across a significant portion of the surface, indicating a preference for contact with the surface. The value of the contact angle (θ) for PET₅₀/PEG₅₀ is 83.56°, for PET₅₀/PEG₅₀ + 1 wt% of DES/TiO₂, θ is 87.36°, for PET₅₀/PEG₅₀ + 5 wt% of DES/TiO₂, θ is 98.41°, for PET₅₀/PEG₅₀ + 10 wt% of DES/TiO₂, θ is 104.36°, for pure PET₅₀/PEG₅₀ + 15 wt% of DES/TiO₂, θ is 108.66°. As per these results, it is observed that PET has hydrophilic in nature and PEG has a hydrophobic polymer in nature but as we add PEG polymer in PET/PEG blend and increase the wt% amount of DES/TiO₂ nanofillers then the blend of PET/PEG-DES/TiO₂ membranes, shows hydrophobic nature [19,20]. PET had a lower fluorine content than PEG, which is the reason roughness has reduced. In conclusion, it was determined that the PEG membrane's high water contact angle was caused by its rough surface structure and low surface energy material. The contact angle can be influenced by the roughness of the solid surface.

On a rough surface, the liquid may not spread as easily, resulting in a higher contact angle. Analyzing contact angles on surfaces with different levels of roughness can provide insights into surface topography and its effects on wetting behaviour. Furthermore, the contact angle reflects the balance between adhesive forces (liquid to solid) and cohesive forces (liquid to itself), a low contact angle indicates strong adhesion. Conversely, a high contact angle suggests weak adhesion, with the liquid forming a more self-contained droplet.

In manufacturing and quality control, contact angle measurements are used to assess the effectiveness of surface treatments. For instance, a surface modification to make it more hydrophobic or hydrophilic can be evaluated by monitoring changes in the contact angle.

4.2.3.8 Mechanical Properties

There are four types of polymer strength: Compressional (when the polymer is compressed), Flexural (when the polymer has stretched), Torsional (when the polymer is twisted), and Impact (under the effects of direct hammering). The percentage of elongation that can be applied before a sample of polymer breaks (its ultimate elongation) measures how much strain can be applied to the material before it breaks at the strength point. Figure 4.2.9 shows the entire mechanical observations for all samples [15,16].

Figure 4.2.9 (I and II) both the tensile and flexural strength/modulus slowly increased with the addition of PET, but the notched impact strength and elongation at break significantly increases, showing a brittle performance of PET/PEG blends. From above the data, blends with

a higher percentage of DES/TiO₂ are stronger elongation than those with PET/PEG blends. This shows that the content of DES/TiO₂ greatly impacts the elongation of the blends.

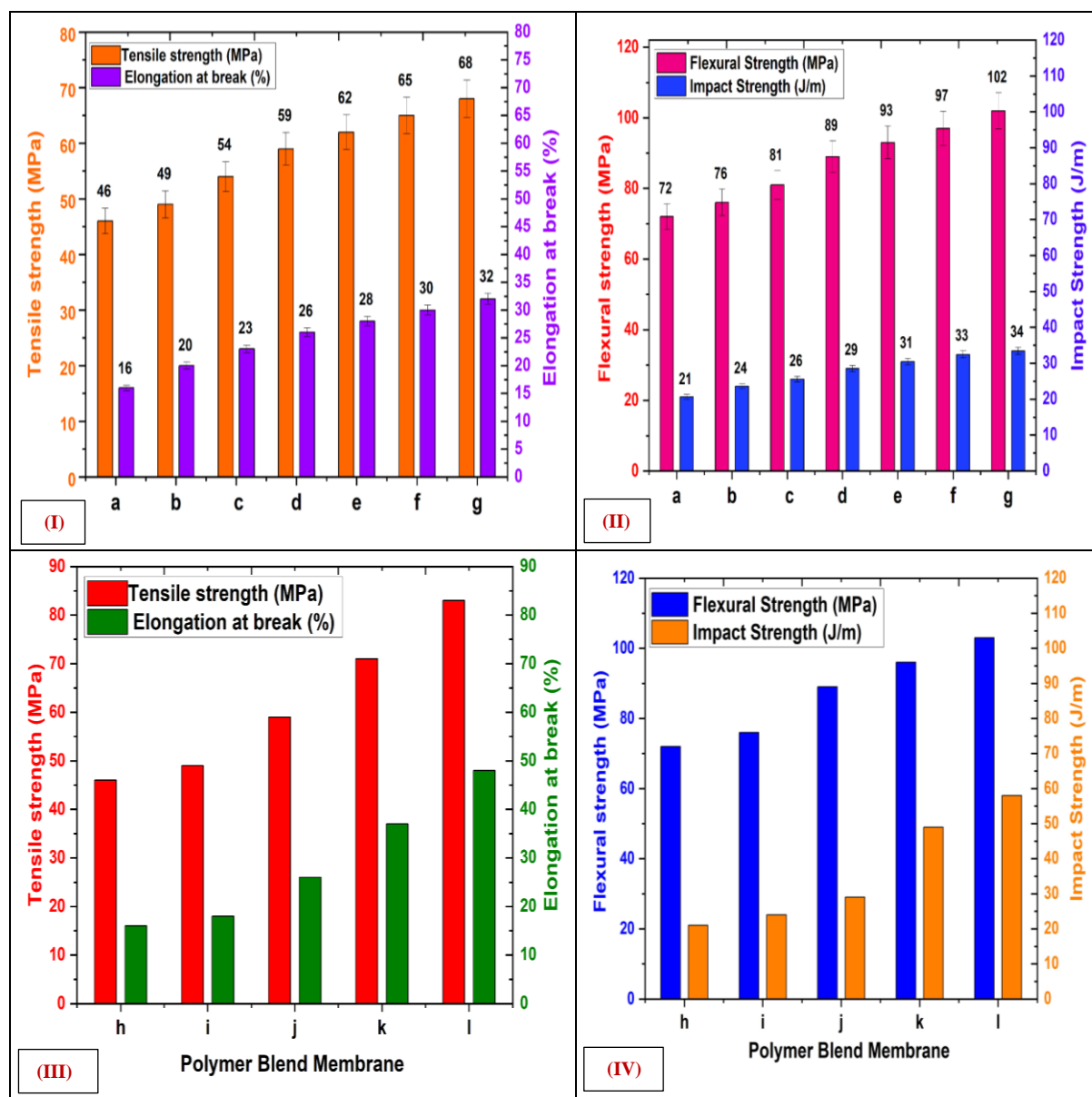


Figure 4.2.9: (I) Tensile strength, Elongation at break, and (II) Flexural strength, Impact strength of Pure PEG, Pure PET and blends PET/PEG membranes (a) Pure PET (b) PET₅₀ / PEG₅₀, (c) Pure PEG, (d) PET₅₀/PEG₅₀ + 1 wt% of DES/TiO₂, (e) PET₅₀/PEG₅₀ + 3 wt% of DES/TiO₂, (f) PET₅₀/PEG₅₀ + 5 wt% of DES/TiO₂, (g) PET₅₀/PEG₅₀ + 10 wt% of DES/TiO₂, (III) Tensile strength, Elongation at break, and (IV) Flexural strength, Impact strength, comparison of (h) Amul Milk bag (i) Amul Butter Milk bag, (j) PET₅₀/PEG₅₀ + 10 wt% of DES/TiO₂ (k) PET₅₀/PEG₅₀ + 12 wt% of DES/TiO₂ (l) PET₅₀/PEG₅₀ + 15 wt% of DES/TiO₂

According to Figure 4.2.9, DES/TiO₂ (10 wt%) has a 30% higher flexural strength than PET/PEG blends. Additionally, it should be observed that the blends are less flexible than PET/PEG-DES/TiO₂, because phase segregation is probably the reason for this. DES/TiO₂ (10

wt%) has the greatest impact strength and is 37% stronger than PET/PEG blends. This result is consistent with elongation at break, where DES/TiO₂ exceeds other blends including PET/PEG [17,18].

This is because DES/TiO₂ has a high energy absorption capacity before breaking. The impact strength of the blends has shown to increase with the addition of DES/TiO₂ up to 37 %, which is the highest of all blends and 45% higher than PET/PEG, which has been observed in Table 4.2.4. As the polymers molecular weight increases, it increases tensile strength also.

Weak intermolecular Van der Waals interactions between polymer chains at low molecular weights are considered for the low strength observed in these materials; in contrast, the bulky and entangled chains at high molecular weights are considered for the high strength observed in these materials [17]. When compared to PEG polymer, porous PET samples with larger pore sizes have a higher stress value.

Table 4.2.4: Tensile strength, Elongation at break, Flexural strength, and Impact strength are mechanical properties of pure PEG, pure PET and blends PET/PEG membranes

Membrane	Tensile strength (MPa)	Elongation at break (%)	Flexural strength (MPa)	Impact strength (J/m)
Pure PEG	46	16	72	21
PET ₅₀ /PEG ₅₀	49	20	86	24
Pure PET	54	23	81	26
PET ₅₀ /PEG ₅₀ + 1 wt% of DES/TiO ₂	59	26	89	29
PET ₅₀ /PEG ₅₀ + 3 wt% of DES/TiO ₂	62	28	93	31
PET ₅₀ /PEG ₅₀ + 5 wt% of DES/TiO ₂	65	30	97	33
PET ₅₀ /PEG ₅₀ + 10 wt% of DES/TiO ₂	68	32	102	34

In the crystalline phase, intermolecular bonding is stronger, which is why a more crystalline polymer is stronger. As a result, polymer deformation may cause the increased

strength associated with orientated chains. The behaviour shifts from hard to soft together with increasing percentage ratios of PEG in PET/PEG polymer blend composition. As shown in the Figure 4.2.9 (I and II), the samples of PEG polymer indicate elastic behaviour at the start of the load, then transition to plastic deformation behaviour as the force increases until breakdown. When compared to other ratios, the pure PET membrane thin film has the highest stress at fracture and the greatest elongation. This sample can sustain stress 49 MPa to 65 MPa and elongation (20% to 30%). In addition, as compared to samples of various ratios, the blend composites of PET/PEG-DES/TiO₂ membranes bears medium stress at fracture and medium elongation. These samples could carry stress 68 MPa with an elongation 32% and this sample could sustain stress 49 MPa to 65 MPa and elongation (20% to 30%). The impact strength of PET/PEG blends has improved by the addition of PET amount in PET/PEG blend. However, because of its branched chain structure, PET has a lower degree of crystallinity and a lower melting point than PEG, which reduces the intermolecular bonding forces in polymer blends made of PEG and PET [18].

Figure 4.2.9 (III and IV) represents the mechanical properties of Amul Milk, Amul Butter Milk, PET₅₀/PEG₅₀ + 10 wt% of DES/TiO₂, PET₅₀/PEG₅₀ + 12 wt% of DES/TiO₂ and PET₅₀/PEG₅₀ + 15 wt% of DES/TiO₂ materials. It is observed that the tensile strength for Amul Milk bag and Amul Butter Milk bag is 47 MPa and 46 MPa, a blend of PET/PEG polymers and composite with DES/TiO₂ nanofillers the tensile strength has increased. Moreover, flexural and impact strength of is also increases in case of blend of PET/PEG polymers and composite with DES/TiO₂. From Figure 4.2.9 (III and IV) it has been observed that after composite with DES/TiO₂ nanofiller the mechanical properties of material have increased, because DES/TiO₂ makes bond with PET/PEG material and decreases fractional free volume and void space between molecules.

4.2.3.9 X-ray Diffraction

In blend membranes, if the two polymers were unsuitable, each would have its own crystal area, and the X-ray scans of the two polymers in the same ratio as those for blending the samples would result in the desired results. Figure 4.2.10 shows X-ray diffraction scans of PET/PEG blends including varying amounts of DES/TiO₂ and the amorphous nature of the blends is shown by the broad and diffuse peak found in each blend composition [20]. As shown in Figure 4.2.10, the observed scans of PET₅₀/PEG₅₀-DES/TiO₂ show an amorphous nature with two peaks centered at $2\theta = 27.20^\circ$. The amorphous peak in the $2\theta = 26^\circ \sim 27^\circ$ range increased as the wt% ratio of DES/TiO₂ in PET/PEG blend composites, which is consistent

with the presence of two amorphous phases in the blends. The initial low-intensity peak might be explained by the size of the side group, which corresponds to an approximately hexagonal structure of the chemical chain and the Van der Waals distance is represented by the second amorphous halo [21].

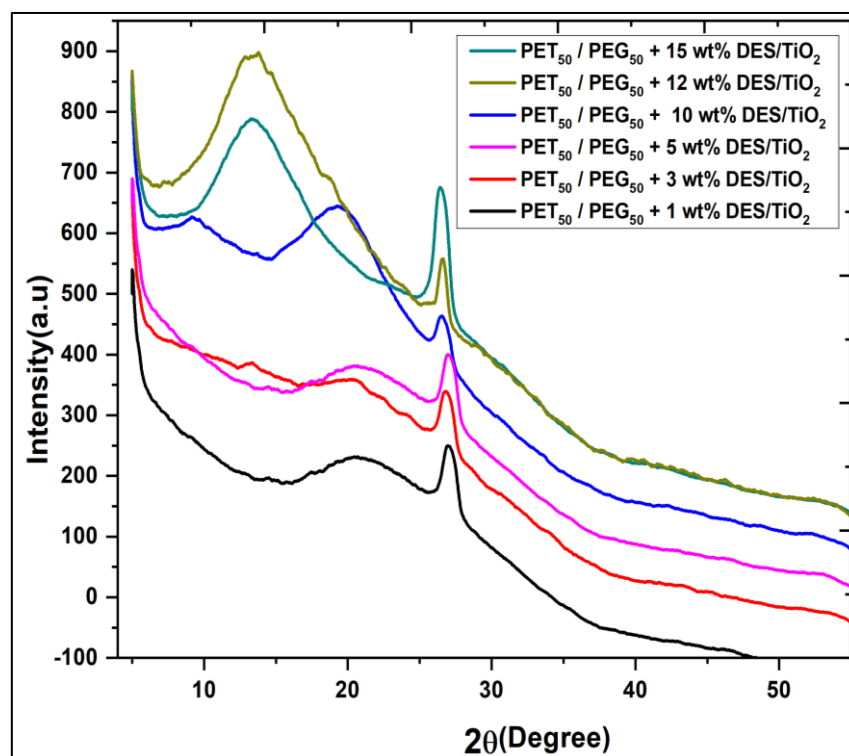


Figure 4.2.10: X-ray diffraction analysis of pure and PET/PEG-DES/TiO₂ blend composite membranes

The strength and height of the peaks increased as DES/TiO₂ content increased, this shows that miscibility occurred in the blends and the sharpness of the peak at 26.50° improved as the blends stretched. In the case of PET₅₀/PEG₅₀ + 15 wt% of DES/TiO₂, the sharpness and relative strength of the 27.12°. The sharpness of the peak at 27.12° improves as the blend composite has stretched; therefore, in the case of DES/TiO₂ (15 wt%) , the sharpness and relative strength of the peaks increases as the nanofillers ratio increases. we obtained a sharp peak at 26.38° and as we increased the wt% of DES/TiO₂ and went toward 15 wt%, the degree angle 2θ increased and shifted towards the right-hand side, which is observed from Figure 4.2.10. This happened because of the amorphous miscibility nature of PET and PEG polymers. These materials showed an amorphous nature since no clear diffraction peak could be seen in the 2θ angle range. PET₅₀/PEG₅₀-DES/TiO₂ blend composite polymers XRD patterns confirmed these are amorphous in nature.

4.2.3.10 FE-SEM Morphology

The morphology of the PET/PEG-DES/TiO₂ blend composites membranes has been confirmed by SEM analysis. Figure 4.2.11 shows SEM images of PET/PEG blends with different weight ratios of DES/TiO₂ in which a non-porous surface has been observed. Before taking the SEM micrographs, a thin layer of platinum was sprayed on the samples to ensure proper electron conductivity. The presence of PET and PEG polymer and DES/TiO₂ may show on the surface of the PET/PEG-DES/TiO₂ blend composites. From the SEM image, the surface morphology becomes denser, but the porous structure remains visible. The dense and uniform structure shown in the SEM micrographs of the surface and cross-section of pure PET/PEG without any obvious porosity morphology. On the surface of the porous PET/PEG blended membrane, however, there is a significant disruption of the pores of roughly 200 nm.

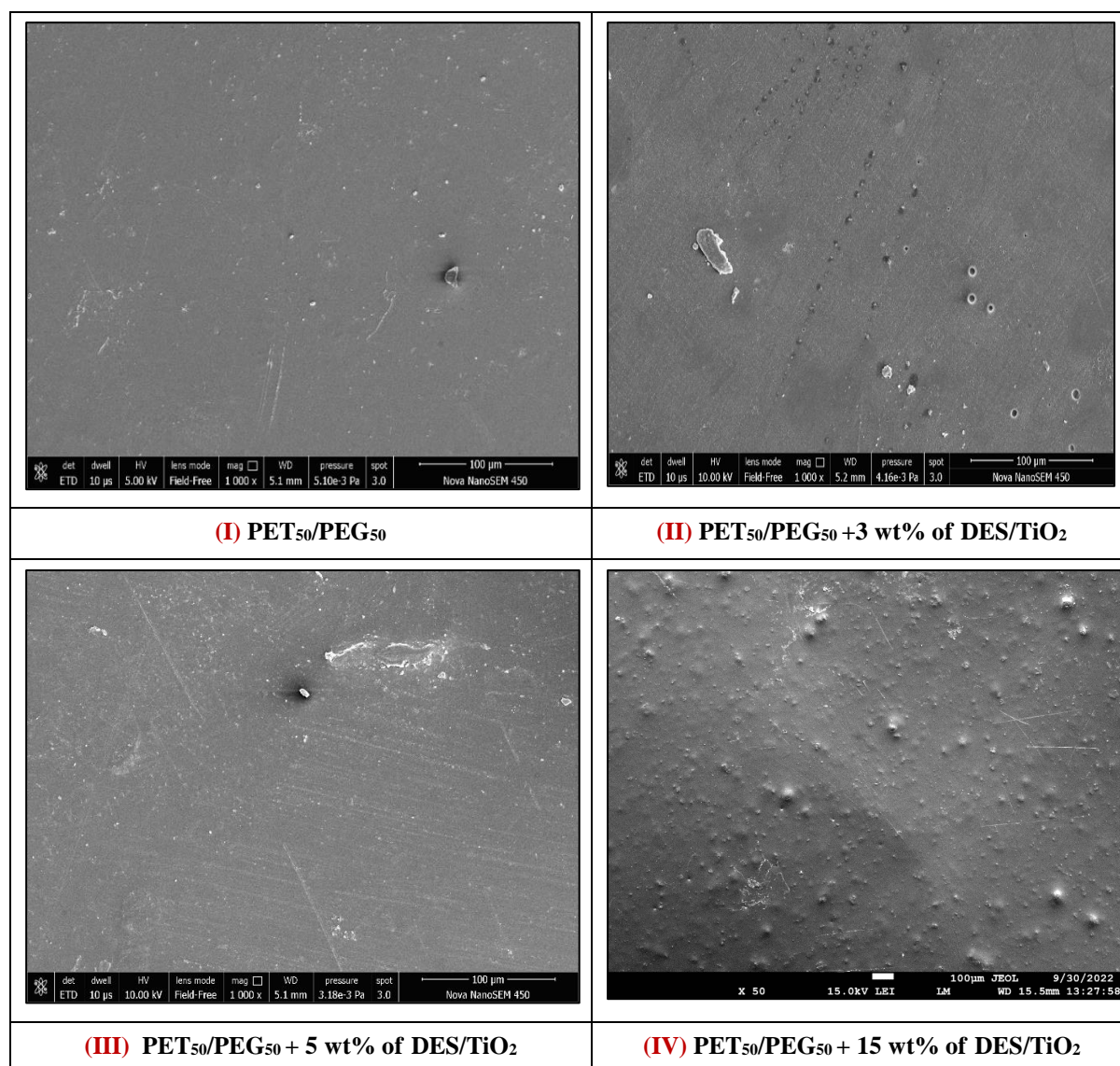


Figure 4.2.11: SEM micrography of PET/PEG blend membranes with different wt% of PET and PEG polymer

The porosities of the blended membranes are efficiently controlled by increasing the DES/TiO₂ content from 3 wt% to 15 wt%, according to cross-sectional SEM micrographs of the porous blends [22]. The inset of Figure 4.2.11 shows the formation of submicro-pores with a diameter of 300 nm and their regular distribution, while smaller pores with a diameter of 150 nm develop within the larger pores above them and act as connecting holes. Blend with PEG polymer are more effective barriers because they form a larger profile for the same amount of material. Where the dark entities are the PEG phases, which have been observed to be dispersed throughout the PET. The surface and cross-section results of all PET/PEG mixes are similar, with the PET forming spherical phases with sizes of approximately 1 μm. Furthermore, the PEG domains on the surface of all PET/PEG blend samples were significantly smaller than those in the cross-sectional areas, with diameters less than 5 μm [20,21]. This might be due to the aggregation of unreacted DES/TiO₂ from the surface during crosslinking, which resulted in some voids in the matrix. The SEM images also clearly show that there are interphases between the dark phases PEG and the white phases PET in blends of PET₅₀/PEG₅₀. The previously indicated functions of PEG might explain this in improving PET compatibility and chemical bonding between PET and PEG during cross-linking. In general, increasing the concentration of DES/TiO₂ minimizes macro voids. As a result, membranes with a higher DES/TiO₂ content have better channel structures, less macro voids, and decreased gas permeability [21,22]. As shown in Figure 4.2.11, the surface of the membrane was relatively smooth, with less pores surface for all of the PET/PEG polymer blend prepared membranes. This result is consistent with our hypothesis that the DES/TiO₂ would increase the exchange rate between these two polymers during the development of the blend composites membrane at a variable polymer concentration in the casting solution. A smooth-skinned, selective layer consequently developed. The rough surface of PET indicates improved adhesion at the PEG surface, resulting in a higher tensile modulus. Blending PEG into the PET phase may decrease the viscosity of the PEG phase, which reduces the movement of PET in the PET/PEG matrix and thereby decrease gas permeability. As an outcome, in all blending ratios of PET/PEG membrane, a larger number of PEG molecules remained on the top surface of the support after the PET was added, resulting in a thicker PET/PEG blend layer after blending, resulting in an excellent making PET/PEG polymer blend membrane. Meanwhile, because of its hydrophilicity, PET/PEG-DES/TiO₂ surface has a lot of smaller ridge-and-valley morphology, which allows for a lower O₂ diffusion rate into the organic phase and more participating monomers during the blending process.

4.2.4 Conclusion

Plastic packaging materials may give the high gas-barrier properties for food packaging either by blending of two polymers or by composite with filler materials into the polymer matrix. According to the studies, it is possible to obtain better barrier characteristics in a PET/PEG blend composites with DES/TiO₂ nanofillers in an industrial technique. The permeability decreased as the percentage of DES/TiO₂ nanofillers in the PET/PEG blend increased, and the composite with DES/TiO₂ provides good nanocomposite processability and high thermal capacity. The decrease in permeability of PET is related to the blend with PEG polymer and the dispersion of the DES/TiO₂ nanoparticles in the PET/PEG blend, since the greater the wt% of DES/TiO₂, the more difficulty the gas will have in passing through the blend and nanocomposite membranes. The SEM image shows the usual amorphous shape of PET, PEG and a blend of PET/PEG polymer, however some of them have been disrupted, most likely due to the nanocomposite being treated twice in separate industrial applications.

The food packaging sector might benefit greatly from these barrier results of O₂ gas since a variety of applications call for the regulation of the environment within the package. The materials used in this article conform to the global for food packaging materials. Since food packaging material must survive transportation, manipulation at supermarkets, and need to arrive in excellent shape to consumers, while retaining the products freshness and shelf life, tensile and impact qualities were tested. For the sample of PET₅₀/PEG₅₀+ 15 wt% of DES/TiO₂, the tensile strength is 30% more than that of pure polymers and blends of PET₅₀/PEG₅₀, indicating that even though the mechanical characteristics of the material improve with PET percentage in a blend of PET/PEG. According to studies on the permeability of O₂, etherified samples are less permeable in case of PET/PEG-DES/TiO₂ material compared to Amul Milk and Amul Butter Milk bags. The permeability of all membranes for O₂ decreases as the weight percentage of DES/TiO₂ polymer increases in PET/PEG-DES/TiO₂ blend composites. As the wt% of DES/TiO₂ increases, the membranes become less selective for O₂/N₂ and less permeable to all gases. Materials with a PET₅₀/PEG₅₀-DES/TiO₂ blend show the strongest compression force results, which are better than those of PET₅₀/PEG₅₀ blend. Additionally, all blended samples are stiffer than those of pure PEG, with those that include all blends of PET/PEG being the stiffest. As a way to improve the mechanical characteristics and gas-barrier properties of a polymer matrix, PEG/PET blend and composites with DES/TiO₂ nanofillers have attracted attention. Moreover, other characteristics like bending strength and modulus increased, large specific areas and surface-active centers enhance physical or chemical

interactions between DES/TiO₂ nanofillers and the polymer matrix of PET/PEG, which improves the more mechanical characteristics as compared to Amul Milk and Amul Butter Milk bags. It has been observed that nanocomposites have accurately synthesized, and nanoparticles dispersed equally throughout the polymer structure. To maintain the quality of chilled packaged food items, this study provides additional information on the development of heat management polymeric materials that are relevant for food packaging applications. Moreover, the blend composite of PET/PEG-DES/TiO₂ material is much effective for packing material than current packing material by industry used.

References:

- [1] D. M. Haile, S. De Smet, E. Claeys, E. Vossen, Effects of light, packaging condition and dark storage durations on colour and lipid oxidative stability of cooked ham, *J. Food Sci. Technol.*, **2013**, 50(2), 239-247.
- [2] N. Bohner, F. Hösl, K. Rieblinger, W. Danzl, Effect of retail display illumination and headspace oxygen concentration on cured boiled sausages, *Food Packag. Shelf. Life*, **2014**, 1(2), 131-139.
- [3] C. Saenz, B. Hernández, M. Beriain, G. Lizaso, Meat color in retail displays with fluorescent illumination, *Color Res Appl.*, **2005**, 30(4), 304-311.
- [4] J. Moller, J. Jensen, M. Olsen, L. Skibsted, G. Bertelsen, Effect of residual oxygen on colour stability during chill storage of sliced pasteurised ham packaged in modified atmosphere, *Meat. Sci.*, **2000**, 54(4), 399-405.
- [5] J. Moller, M. Jakobsen, C. Weber, T. Martinussen, L. Skibsted, G. Bertelsen, Optimisation of colour stability of cured ham during packaging and retail display by a multifactorial design, *Meat. Sci.*, **2003**, 63(2), 169-175.
- [6] G. Mortensen, J. Sorensen, H. Stapelfeldt, Effect of light and oxygen transmission characteristics of packaging materials on photo-oxidative quality changes in semi-hard Havarti cheeses, *Packag. Technol. Sci.*, **2002**, 15(3), 121-127.
- [7] A. Vasquez-Caicedo, S. Schilling, R. Carle, S. Neidhart, Impact of packaging and storage conditions on colour and β -carotene retention of pasteurised mango puree, *Eur. Food Res. Technol.*, **2007**, 224(5), 581-590.
- [8] M. Estevez, S. Ventanas, R. Cava, Effect of natural and synthetic antioxidants on protein oxidation and colour and texture changes in refrigerated stored porcine liver pate, *Meat. Sci.*, **2006**, 74(2), 396-403.

- [9] M. Estevez, S. Ventanas, R. Cava, Physicochemical properties and oxidative stability of liver pâté as affected by fat content, *Food Chem.*, **2005**, 92(3), 449-457.
- [10] J. Remnant, J. Adams, The nutritional content and cost of supermarket ready-meals, Cross-sectional analysis, *Appetite*, **2015**, 92, 36-42.
- [11] G. Smith, K. Belk, J. Sofos, J. Tatum, S. Williams, Economic implications of improved color stability in beef., *New York: John Wiley and Sons*, **2000**, 397-426.
- [12] R. Kampschmidt, Meat discoloration, effect of wave length of light on the discoloration of cured meats, *J. Agric. Food Chem.*, **1955**, 3(6), 510-512.
- [13] D. Juncher, B. Ronn, T. Beck Hansen, et al., Effect of pre-slaughter physiological conditions on the oxidative stability of colour and lipid during chill storage of sliced, retail packed roast ham, *Meat. Sci.*, **2003**, 63(2), 151-159.
- [14] H. Larsen, F. Westad, O. Sorheim, L. Nilsen, Determination of critical oxygen level in packages for cooked sliced ham to prevent color fading during illuminated retail display, *J. Food Sci.*, **2006**, 71(5), 407-413.
- [15] M. Rahmani, A. Kazemi, F. Talebnia, Matrimid mixed matrix membranes for enhanced CO₂/CH₄ separation, *J. of Poly. Engin.*, **2015**, 36 (5), 499-511.
- [16] A. Silberbauer, M. Schmid, Packaging concepts for ready-to-eat food: recent progress, *J. Packag Technol. Res.*, **2017**, 1(3), 113-126.
- [17] J. Tang, Y. Hong, S. Inanoglu, F. Liu, Microwave pasteurization for ready-to-eat meals., *Curr. Opin. Food Sci.*, **2018**, 23, 133-141.
- [18] D. Haile, S. de Smet, E. Claeys, E. Vossen, Effect of light, packaging condition and dark storage durations on colour and lipid oxidative stability of cooked ham, *J. Food Sci. Technol.*, **2013**, 50(2), 239-247.
- [19] A. Incoronato, D. Gammariello, A. Conte, M. del Nobile, Ready-to-cook fresh meal: study for shelf life prolongation, *J. Food Sci. Technol.*, **2016**, 53(2), 990-995.
- [20] F. Mestdagh, B. de Meulenaer, J. de Clippeleer, F. Devlieghere, A. Huyghebaert, A Protective influence of several packaging materials on light oxidation of milk, *J. Dairy Sci.*, **2005**, 88(2), 499-510.
- [21] T. Anthierens, P. Ragaert, S. Verbrugghe, et al., Use of endosporeforming bacteria as an active oxygen scavenger in plastic packaging materials, *Innov. Food Sci. Emerg. Technolog.*, **2011**, 12(4), 594-599.
- [22] J. Lee, Y. Chang, E. Lee, H. Song, P. Chang, J. Han, Ascorbic acid based oxygen scavenger in active food packaging system for raw meatloaf, *J. Food Sci.*, **2018**, 83(3), 682-688.